Melt-enhanced strain localization and phase mixing in a large-scale mantle shear zone (Ronda peridotite, Spain)

Sören Tholen[1], Jolien Linckens[1,2], Gernold Zulauf[1]

[1] Institut für Geowissenschaften, Goethe Universität Frankfurt a.M., Altenhöferallee 1, D-60438, Germany

[2] Tata Steel, R&D, 1970 CA Ijmuiden, The Netherlands

Correspondence to: Sören Tholen (tholen@geo.uni-frankfurt.de)

Abstract. Strain localization in upper mantle shear zones by grain size reduction and the activation of grain size sensitive deformation mechanisms (grain boundary sliding, diffusion creep) is closely linked to phase mixing. With its mylonitic grain sizes (50-100 μm) and well mixed phase assemblage, the km-scale shear zone at the northwestern boundary of the Ronda peridotite is in this respect no exception. In transects across the "mylonitic" into the less deformed "tectonic" part of this shear zone four dominant microstructural domains were identified: (1) olivine-rich matrix, (2) mixed matrix and neoblast tails of (3) clino- and (4) orthopyroxene porphyroclasts. In these, phase mixing quantities, its formation processes and its impact on strain localization were analyzed by a combined ~~microstructural~~ microfabric (EBSD) and geochemical (EPMA) analysis. The d~~D~~ominant microstructure of all samples is the mixed matrix composed of olivine, ortho- and clinopyroxene. Its homogenous distribution of interstitial, and/or wedge-shaped pyroxenes contradicts mechanical mixing. In general, high (> 60%) phase boundary percentages in all four microstructural domains indicate extensive phase mixing independent from microstructural domain and distance to the deformational center of the shear zone located at the NW boundary of the peridotite massif. The constant grain sizes with local variations independent on the distance the deformational ~~center~~centre indicate a broad scale deformation with ~~±~~ nearly constant stresses in the entire mylonitic area. ~~Decreasing Mg# and increasing Ti contents with increasing distance to the NW shear zone boundary,~~ Hh~~ighly~~ lobate phase boundaries, homogenous phase mixing and secondary phase distribution in all samples as well as continuous geochemical trends independent on the microstructural domain ~~in all samples~~ corroborate a reaction-driven, metasomatic formation ~~phase mixing by melt-rock reactions and crystallization of pyroxenes~~ of the mixed matrix and pyroxene tails in the entire shear zone ~~transect~~. Consistent geochemistry and phase assemblage in mylonites and tectonites but a change from equiaxial (tectonites) to wedge-shaped pyroxenes aligned in the foliation (mylonites) indicate a pre- to syn-deformational metasomatism~~melt infiltration~~. Established syn-deformational temperature estimates (800-900° C at 1.95-2.00 GPa), amphibole abundances in pyroxene neoblast tails, olivine B-type crystallographic preferred orientations (CPOs) and the microstructural consistency of grt/spl-mylonites from both major peridotite massifs of the Gibraltar arc, Ronda and Beni Bousera (Morocco), indicate an OH-bearing metasomatism by small fractions of evolved melts, which did not reset the equilibrium temperatures.~~Following the geochemical gradient, the potential source of melt is below a structurally deeper "melting" front which separates the sheared peridotites from coarse granular peridotites.~~ Grain size reduction by crystallization of interstitial pyroxenes and the formation of neoblast tails ~~The presence of mixed matrix~~ in the entire shear zone as well as the activation of~~,~~ dissolution-precipitation creep in the mylonitic mixed matrix corroborates the significance of that ~~its microstructural and geochemical consistency indicate that the melt infiltration~~metasomatism for ~~was fundamental for the formation of~~ and the strain localization in the evolution of the major shear zone of the~~major shear zone of the~~ NW Ronda ~~peridotite~~shear zone. Strong CPOs of all major phases (ol, opx, cpx) suggest dislocation creep as dominant deformation mechanism in the entire shear zone.

1 Introduction

Deformation in the upper mantle is localized in ductile shear zones. Accommodating most of the deformation in the lithospheric mantle, the shear zones have a major imprint on large scale deformation and plate tectonics (Bercovici and Ricard, 2014; Drury et al., 1991). To localize strain, weakening must occur. Weakening in turn is dependent on an initial heterogeneity/anisotropy and a softening mechanism localizing the strain in ~~the~~the area of heterogeneity and later on in the shear zone itself. In the lithospheric mantle, several types of heterogeneity were identified as potential "seeds" for strain localization: (1) Large-scale variations in the geothermal gradient as present for hot plumes or cold lithospheric roots of cratons, (2) major-element and modal heterogeneities as present in the compositional layering of most peridotite massifs, (3) the presence of melt, (4) variations in the hydration state of particularly olivine, (5) grain size heterogeneities and (6) lateral changes of the olivine CPO (e.g., Tommasi and Vauchez, 2015). Strain softening mechanisms that localize and maintain deformation were subdivided into three types (Drury et al., 1991): Thermal softening caused by shear heating and the positive feedback of temperature and strain rate (e.g., Kelemen and Hirth, 2007), geometric softening caused by the anisotropy in creep strength of grains aligned in a ~~crystallographic preferred orientation (CPO)~~ ((Mameri et al., 2019; White et al., 1980)~~Passchier and Trouw, 1996)~~ and microstructural or reaction softening which occurs by grain size reduction and the activity of a grain size sensitive deformation process (Drury and Urai, 1989). Both, thermal softening as well as microstructural softening depend on the presence of mixed phase assemblage, either as seed or as stabilization for strain localization (e.g., Kelemen and Hirth, 2007; Linckens et al., 2015). Phase mixing in the upper mantle has been ascribed to several different, deformation or reaction induced processes ~~which can either be deformation or reaction induced~~. Deformation induced phase mixing is commonly associated with grain boundary sliding (GBS). During GBS, neighbour switching of grains was reported to form mixtures (e.g., Boullier and Gueguen, 1975; Hirth and Kohlstedt, 2003) but also aggregates (Hiraga et al., 2013). Furthermore, disaggregation of single-phase domains at high shear strains ("Geometric mixing") was reported by Cross and Skemer (2017). Additionally, nucleation of neoblasts in creep cavitations during GBS leading to phase mixtures was reported by Précigout and Stünitz (2016). Reaction induced phase mixing is bound to either metamorphic (P-T) or metasomatic (melt/fluid) reactions. In the upper mantle, phase transitions from garnet to spinel and to plagioclase peridotites change the phase assemblage and the mineral chemistry of all present phases (e.g., Borghini, 2008). ~~Thereby, m~~Neoblast formation~~etamorphic reactions~~ can thereby lead to phase mixing and, during deformation, to the formation of ultramylonites (Furusho and Kanagawa, 1999; Newman et al., 1999; Tholen et al., 2022). Additionally, the interaction of rock and melt or fluid can cause phase mixing by precipitation of neoblasts and reactions with porphyroclasts/ pristine~~old~~ grains (e.g., Dijkstra et al., 2002; Kaczmarek and Müntener, 2008).

With its decreasing grain size, scattering of pyroxene neoblasts and concurrent diminishing of prior strong olivine CPOs towards the contact to the bordering Jubrique unit Ronda's NW tectonit~~ic~~e/mylonit~~ic~~e zone is commonly interpreted as km-scale upper mantle shear zone (Garrido et al., 2011; Précigout et al., 2013, 2007). In contrast to earlier studies on phase mixing in upper mantle shear zones by the authors where mixing depends on metamorphic and metasomatic reactions

(Linckens and Tholen, 2021; Tholen et al., 2022) Ronda's mylonites are thought to have little to no metamorphic or metasomatic influence (e.g., Johanesen and Platt, 2015; Précigout et al., 2007). Mechanisms of strain localization and phase mixing operating in Ronda's mylonites were suggested to be bound to grain boundary sliding accommodated by dislocation creep (Précigout et al., 2007). Following Précigout et al. (2007), neighbour-switching during this process leads to scattering of orthopyroxene neoblasts within the olivine-rich matrix. This classical interpretation includes a general grain size reduction in connection with the intensification of mixing towards the NW shear zone boundary which is thought to represent a strain localization with increasing stress (e.g., Garrido et al., 2011; Précigout et al., 2013). However, Ronda's peridotites in the complete shear zone area are extensively mixed. Thus, also the ~~lesser deformed~~low strain ~~regions~~area of ~~the shear zone present in~~ the ~~distal~~ mylonites ~~and~~ adjoining spinel tectonites and the spinel tectonites themself are thoroughly mixed (e.g., Johanesen and Platt, 2015). Although mixing in the spinel tectonites was postulated to be melt derived (Johanesen et al., 2014; Soustelle et al., 2009), the mylonites were so far considered to be either completely melt-free (Précigout et al., 2007; Soustelle et al., 2009) or melt-absent during the deformation (Johanesen and Platt, 2015). ~~Johanesen and Platt (2015) challenged the classical view of Précigout et al. (2007) and proposed on base of a constant grain size of recrystallized olivine in the entire shear zone (mylonite + tectonites), an evolution of the shear zone at constant stress with increased strain rates in the NW.~~

~~With our~~This detailed microstructural and geochemical study on samples taken across multiple transects ~~across~~from the mylonites ~~and~~ into the tectonites (Fig. 1) ~~we~~ focuses on the origin and evolution of the mylonitic unit. Analysis of the four major microstructural domains (mixed matrix, neoblast tails of clino-/orthopyroxene porphyroclast, olivine-rich matrix) decipher ~~this evolution, which involves~~ the interplay of ~~melt~~metasomatism, phase mixing and grain size reduction ~~which in turn have a major~~and its impact on ~~deformation and shear localization in~~ the evolution of the NW Ronda shear zone.
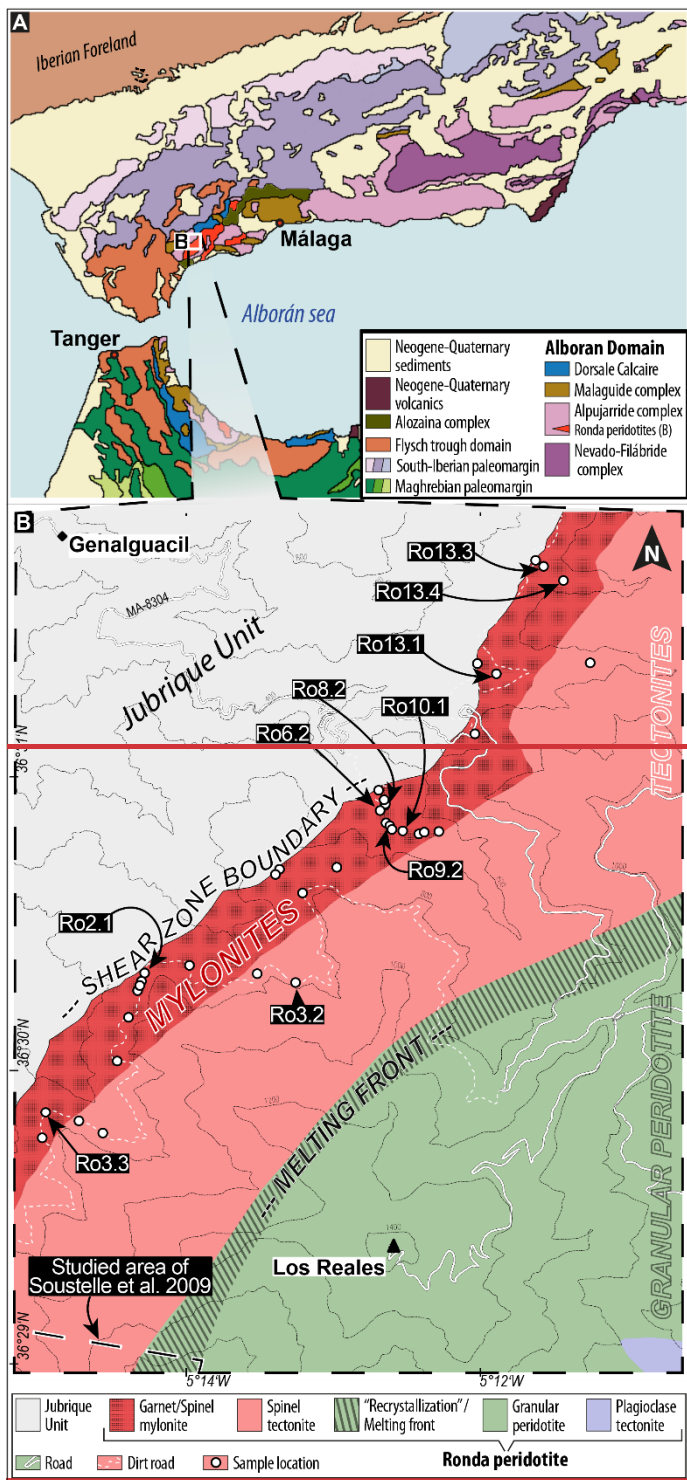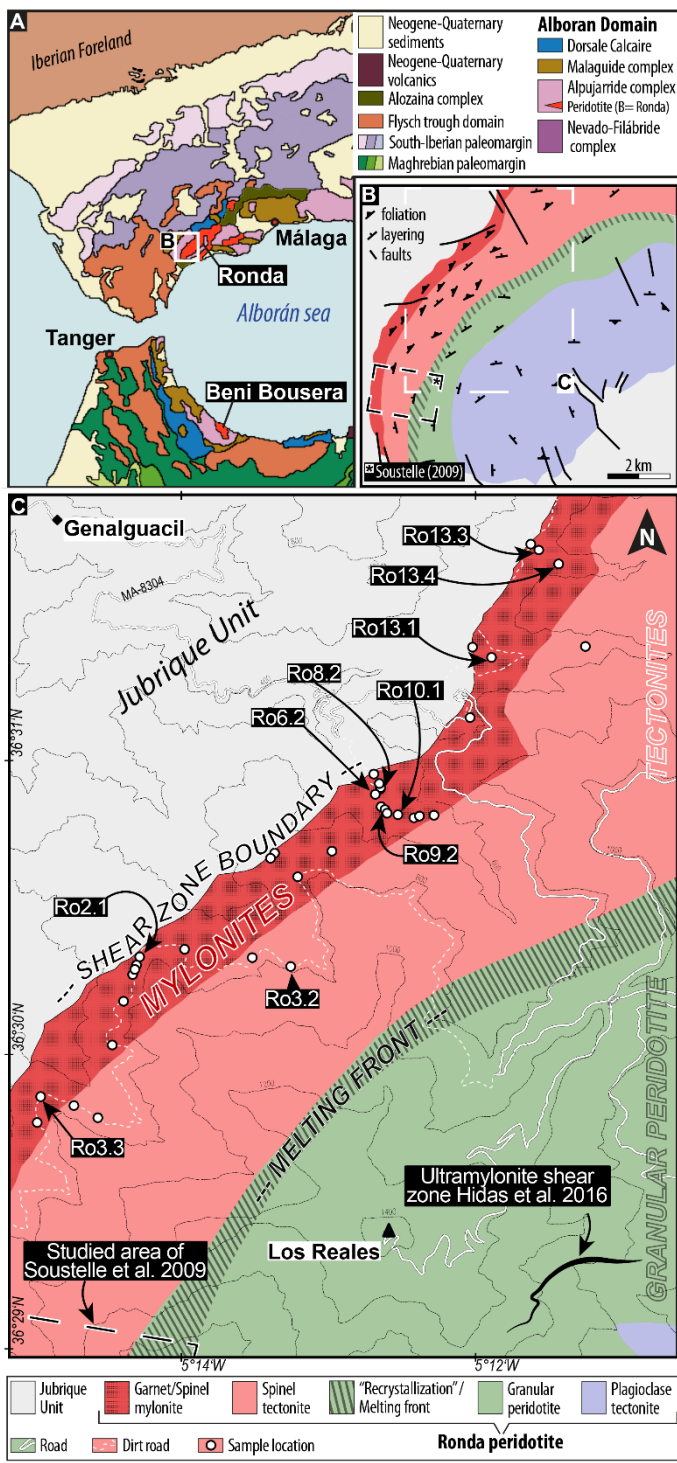
Fig. 1. A: Geological overview of the Gibraltar Arc (Betic cordillera and Rif mountains) modified after Suades and Crespo-Blanc (2011). Ronda Peridotite indicated by white box. B: Schematic structural map of the NW Ronda peridotite with area of

2 Geological setting

The Ronda peridotite, situated in southern Spain, is part of the Betic cordillera (Fig. 1). Together with the Rif mountains of N Morocco it forms the Gibraltar arc (= Betic-Rif orogen), which surrounds the Alboran Sea. The Betic cordillera is subdivided into four tectonic domains: The external (1) Sub-Iberian and (2) Maghrebian domains formed by the paleomargins of Iberia and NE Africa, (3) the allochthonous Flysch trough unit comprising Mesozoic to Cenozoic sediments of the oceanic or continental Tethys, and (4) the internal, Alboran domain (Fig. 1A) (Booth-Rea et al., 2007). Separated by extensional shear zones and different metamorphic records, the Alboran domain is divided into three main tectonic allochthons (Platt et al., 2006). In ascending order these are the Nevado-Filábride complex, the Alpujárride complex and the Maláguide complex. The lowermost Nevado-Filábride complex records a multistage metamorphic evolution including eclogite facies metamorphism followed by albite-epidote amphibole or greenschist facies overprints during decompression (Platt et al., 2006; Puga et al., 1999). The middle Alpujárride complex underwent HP-LT metamorphism overprinted by decompression and local heating (Balanyá et al., 1997; Platt et al., 2005). The uppermost Maláguide complex is characterized by unmetamorphic rocks or by very low-grade metamorphism (Lonergan, 1993).

The peridotite bodies of Beni Bousera, Ojen, Carratraca and Ronda in sensu stricto are embedded as lenses in the upper Alpujárride complex (Platt et al., 2006). Superimposed on the Ronda peridotite, the Jubrique (or Casares) unit represents a highly attenuated crustal section of ≤ 5 km thickness (Fig. 1) (Barich et al., 2014; Obata, 1980). Near the contact to the Ronda peridotite, it displays MP-HT granulite facies kinzigites with melt inclusions (Balanyá et al., 1997; Barich et al., 2014). With increasing distance to the peridotite, the metamorphic conditions decrease to LP-LT phyllites at the contact to the Maláguide complex (Balanyá et al., 1997). In the South and Southeast granitic rocks and migmatites of the Blanca unit underly the Ronda peridotite (Fig. 1). Partial melting and deformation of this unit at the contact to the peridotite have been attributed to the emplacement of the Ronda peridotite (Esteban et al., 2008). U-Pb SHRIMP dating of neo crystalline zircon rims from felsic and granitic dykes in this "dynamothermal aureole" point to an emplacement of the Ronda peridotite at 22.3 ± 0.7 Ma (Esteban et al., 2011). Miocene, brittle, top-to-the-N extensional faulting led to the final emplacement of the Alpujárride complex with high cooling rates from 300-100 °C/Ma (Esteban et al., 2004; Platt et al., 2003; Rossetti et al., 2005).

2.1 The Ronda peridotite

With ca. 300 km^2 areal extent, the Ronda peridotite is the world's largest exposure of subcontinental mantle (Obata, 1980). Its (micro) structural, petrological, and geochemical zoning led to its subdivision into four tectonometamorphic units (Fig. 1) (Précigout et al., 2013; Van Der Wal and Vissers, 1996, 1993). From NNW to SSE these are (1) a garnet/spinel-mylonite

unit, (2) a spinel-tectonite unit, (3) a coarse-grained granular-peridotite unit, and (4) a plagioclase-tectonite unit. Knowing

130 that tectonites include mylonitic microstructures, we nevertheless adopt the established nomenclature and distinguish between "mylonites" and "tectonites". ~~Thereby we hope to prevent confusion by multiple designations and enable a simple reference to the literature.~~

The garnet/spinel mylonites, located along the contact to the Jubrique unit (~500-750 m thickness), are composed of fine-grained, porphyroclastic spl- and grt-bearing peridotites (lherzolites, harzburgites, dunites) (Van Der Wal and Vissers, 1993).

135 ~~They are strongly foliat~~with a nearly horizontal lineation (Précigout et al., 2013).~~ed (~N50° strike, 80° NW dip)~~ ~~with a nearly horizontal lineation (Précigout et al., 2013).~~ Garnet-bearing pyroxenite layers are parallel to the strong foliation and predominantly stretched which leads in places up to their pinch-and-swell type boudinage (Précigout et al., 2013; Van Der Wal and Vissers, 1993). Occasionally, the pyroxenite layers ~~are also~~ show ~~folded~~ intrafolial folds~~ly~~ with their ~~fold~~ axes oriented NE-SW slightly dipping towards the NE (Précigout et al., 2013). Graphitized diamonds in garnet-bearing

140 pyroxenites and pre-deformational assemblages of olivine + pyroxenes + garnet found in pressure shadows indicate an origin of great depth (> 150 km) and a pre-mylonitic equilibration in the garnet stability field (1150 °C, 2.4-2.7 GPa (~100 km depth)) (Davies et al., 1993; Garrido et al., 2011). For mylonitic assemblages in the spinel stability field, equilibration conditions of 800-900 °C and 1-2 GPa have been obtained by Johanesen et al. (2014), Garrido et al. (2011) and Van Der Wal and Vissers (1993).

145 The transition between grt/spl-mylonite and the spl-tectonite remains controversial. Contrary to cross-cutting contacts between mylonites and tectonites described by Van Der Wal and Vissers (1996), Précigout et al. (2007) and ~~(~~Soustelle et al.~~,~~ (2009) postulated a continuous gradient from coarse grained tectonites (grain size of 250-450 µm) to fine-grained mylonites (150-220 µm). Decreasing strain with increasing distance to the NW boundary of the mylonites is also indicated by decreased folding intensity and rotation of pyroxenite layers towards the SE (Précigout et al., 2013). However, Johanesen

150 and Platt (2015) reported for both units (mylonites + tectonites) a consistent grain size of recrystallized olivine (~130 µm) and only an increase in the percentage of the recrystallized olivine grains towards the NW. As the main lithologies (harzburgites, lherzolites) and the foliation and lineation stay similar in tectonites and mylonites, tectonites were interpreted as the weaker deformed counterpart of the mylonites (Van Der Wal and Vissers, 1993). Microstructural and geochemical data indicate additionally, that the tectonites were affected by melt impulses originating from the structurally lower, coarse

155 granular peridotites (Johanesen et al., 2014; Soustelle et al., 2009).

Together with the grt/spl-mylonites, the spl-tectonites form the km-scale NW Ronda shear zone (Fig. 1). Its characteristics are the penetrative foliation with subhorizontal stretching lineation defined by cm-scale elongated orthopyroxenes and shear criteria indicating sinistral kinematics and minor coaxial shortening (Balanyá et al., 1997; Précigout and Hirth, 2014; Van Der Wal and Vissers, 1996). The orientation of the foliation and lineation roughly follows the boundaries to the adjacent

160 metasedimentary Jubrique unit in the NW and to the underlying coarse granular-peridotite unit in the SE (Fig. 1) (Van Der Wal & Vissers, 1996). In places, foliation and lineation show local variations and weakening (Van Der Wal & Vissers, 1996). For the examined area, the average orientation of the foliation is with ~N50° strike and 80° NW dip in accordance

with prior research (Précigout et al., 2013). The ~~Even if not in its present appearance, the~~ shear zone is considered to play a decisive role in the exhumation of the peridotite massif (Johanesen et al., 2014; Précigout et al., 2013). ~~Its boundaries are defined by the metasediments of the adjacent Jubrique unit in the NW and the underlaying coarse granular peridotite unit in the SE (Fig. 1). Throughout the manuscript, the authors refer to the NW contact of the garnet-bearing mylonites which constitute the deformational center of the shear zone and the adjacent metapelites of the Jubrique unit as "shear zone boundary" (SZB). Sample locations are allocated with their distance [m] to the SZB (Fig. 1). Even if not in its present appearance, the shear zone is considered to play a decisive role in the exhumation of the peridotite massif (Johanesen et al., 2014; Précigout et al., 2013).~~

The coarse granular-peridotite unit is separated from the spl-tectonite ~~zone~~ unit by a "recrystallization"/ "coarsening" or "melting" front (≤ 400 m) (Lenoir et al., 2001). Here, deformed grains annealed and coarsened, the foliation is lost and garnet-pyroxenite layers are recrystallized as spl-websterites (Garrido and Bodinier, 1999). Lenoir et al. (2001) have shown that the recrystallization front is the boundary/aureole of an area of partial melting (= coarse granular-peridotite unit) with melt extraction < 5%. Secondary cpx, crystallized ahead of the front, ~~proofed~~ indicated a re-fertilization (Soustelle et al., 2009). The location of the front was shown to be ~~strongly~~ dependent on the peridotite solidus (≥1200° C, 1.5 GPa) ~~)~~ in regard to the temperature gradient within the peridotite body (Lenoir et al., 2001). The coarse granular-peridotite unit itself is mainly composed of unfoliated spinel harzburgite with minor lherzolite and dunite and various types of pyroxenites (Garrido and Bodinier, 1999). The preservation of a strong olivine crystallographic preferred orientation (CPO) and folds of spl pyroxenites corroborates its connection to the overlaying spl-tectonites (Vauchez and Garrido, 2001).

The youngest unit, overprinting the coarse granular-peridotite unit in the southeast, comprises the plagioclase tectonites (Obata, 1980). Their equilibration at pressures of 0.8-0.9 GPa was placed in the context of the massif's exhumation (Hidas et al., 2016)~~in an upper plate of a subduction zone (Van der Wal, 1993)~~. It is composed of spl-free and spl-bearing plagioclase-peridotite layers. The transition between both units records km-scale folding and shearing including the development of a new foliation and the formation of mylonitic and ultramylonitic shear zones, which are tectonically assigned to the decompression of the massif from spinel to plagioclase lherzolite facies prior to the emplacement into the crust (Fig. 1; Hidas et al., 2013a).

3 Methods

Samples were cut perpendicular to the foliation and parallel to the stretching lineation (X-Z section). Thin sections of these sections were polished to a thickness of ~30 µm. After optical analysis by polarization microscopy, electron backscatter diffraction (EBSD) analysis combined with energy dispersive X-ray spectroscopy (EDX), and electron probe microanalysis (EPMA) were~~was~~ performed on carbon coated thin sections. For EBSD and backscattered electron (BSE) analysis, thin sections were polished beforehand with 0.03 µm colloidal silica.

Backscattered electron, EBSD and EDX analysis were conducted at the Institute for Geology and Mineralogy - University of Cologne using a Zeiss Sigma 300-VP field emission scanning electron microscope (SEM) equipped with a NordlysNano EBSD detector (Oxford Instruments). For a comprehensive overview, the entire thin sections were scanned in grids simultaneously by BSE and EDX (O, Mg, Al, Si, Ca, Cr, Mn and Fe; ~~Fig. 3~~Fig. 2). Having identified the microstructures of interest, these were scanned simultaneously by EBSD, EDX, BSE and forescattered electrons (FSE). Measurement settings were an acceleration voltage of 20 kV and a variable step size adapted according to grain sizes. Depending on the step size and acquisition time, EBSD map sizes differ over a wide range. For data acquisition, the program AZtec 4.2 was used (Oxford Instruments). The consistency of orientations between sample, measurement and post-processing reference frame was ensured by the measurement of a quartz standard. It consists of four synthetic quartz crystals embedded in epoxy. The known positions of the quartz single crystals in the standard combined with their known individual orientation enables the operator to identify possible rotations (spatially or crystallographic) of the data during acquisition and processing. Kilian et al. (2016) have shown that such rotations occur often due to unknown orientation in sample material and mistranslations between different processing platforms. Obtained EBSD data was as first step cleaned by deleting "wild spikes" and filling not indexed points with the average orientation of 6 or more neighbour orientations of the same phase (HKL Channel 5 software - Oxford Instruments). Additionally, the EBSD data were corrected for systematic mis-indexing of olivine due to similar diffraction patterns for orientations rotated 60° around [100]. Secondly, the cleaned data were imported into the MTEX 5.7 MATLAB extension (e.g., Bachmann et al., 2010). All following data processing and analysis were conducted using MTEX (http://mtex-toolbox.github.io/). Orientations of indexed points with high mean angular deviations (MAD > 1) were filled by the mean orientation of the neighbouring points. After grain calculation (grain internal misorientation < 15°) grain size specific and inclusion deletion and/or filling was carried out individually for each map. Incomplete grains at the borders of the mapped areas and badly indexed grains were excluded from further analysis. Grain reconstruction of serpentinized olivine grains was achieved by applying a half quadratic filter which preserves inner grain boundaries and fills missing data. An example is shown for the ol-rich matrix in figure 5. For all other phases, the original cleaned EBSD data is used to preserve the original grain and boundary shape. During the cleaning and ~~reconstructio~~reconstruction~~n~~, the results were checked against backscattered/forescattered, band contrast and microscope images. The EBSD phase assignment was checked by simultaneously obtained EDX maps and/or EDX point measurements. The cleaned EBSD maps were thereupon analyzed for grain and phase properties, boundary properties and orientation properties. Analyzed grain properties are phase abundances by covering area percentage, grain amount, grain size by the equivalent circular diameter (ECD), grain shape by aspect ratio, shape factor and shape preferred orientation (SPO). Phase abundances given by "%" in figures and in the entire manuscript are referring to area percentages. Boundary properties are grain (phase A- phase A) and phase (phase A- phase B) boundary percentages calculated by phase specific boundary length. The ratio of total grain to total phase boundary length gives the "mixing intensity" of a microstructure. Orientation properties include phase-specific crystallographic orientations illustrated by orientation or orientation density function (ODF) stereo plots. Its strength is calculated by the M-index (M) ~~and,~~ the J-index.~~,~~ both of which were used only from the minimum of 150 grains. ~~and the maximum mrd value (multiple of~~

random distribution). Both,The J-index (Bunge, 1982) and M-index (Skemer et al., 2005), express the strength of a given ODF. For a detailed evaluation of both see Skemer et al. (2005). All pole figures are equal-area lower-hemisphere plots. ODFs are only displayed for a minimum number of 100 grains per phase. Otherwise, single grain orientations are plotted in the stereoplot as dots. ODFs were calculated with grain mean orientations and a consistent halfwidth of 15°. To facilitate the comparison between ODF plots, the color-coding range is fixed according to the maximum of multiple of random distribution (mrd) from blue (mrd= 0) to red (mrd= 3). Higher mrd values are accordingly also colored red-. Dislocation densities were calculated in MTEX by resolving the geometrically necessary dislocation content following the method of (Pantleon, (2008).

Microprobe measurements of olivine, clinopyroxene, orthopyroxene, spinel and amphibole were conducted at the Institute of Geosciences - Goethe University Frankfurt a.M. using a field emission JEOL JXA-8530F Plus microprobe equipped with 5 wavelength-dispersive spectrometers. Measuring settings were 15 kV acceleration voltage and 20 nA beam current for 20 s (Al, Cr, Ca, Na, Mn, Fe and Ni), 30 s (P, K and Ti) or 40 s (Mg and Si) peak and 20 s for background measurement (settings and detection limits in S1). The same measurement settings and standards were used for the analysis of all phases. The spot-size was adjusted to the grain size with minimum sizes of 1 µm for small neoblasts and maximum 4 µm for porphyroclasts. References to supplementary data are given in the text by an "S" combined with the number of the appendix (e.g., S3 for supplementary CPO dataEPMA data).

4 Results

Samples were taken from multiple transects of the shear zone over a range from 39 to 703 m distance to the NW boundary of the Ronda peridotite massif shear zone boundary ("NW-B"; Fig. 1). Sample locations are therefore allocated with their distance [m] to the NW-B (Fig. 1). Referring to the established subdivision of the Ronda peridotite developed by Précigout et al. (2013) and Van Der Wal and Bodinier (1996) our samples are dominantly taken from the garnet-spinel mylonites and in greater distance from the shear zone boundary (SZBNW-B) from the spinel tectonites (Fig. 1). Both units are composed of lherzolite or harzburgite with minor dunitic lenses. The samples have a highly variable degree of serpentinization. Consistent with previous studies, the foliation is mostly oriented parallel to the SZBNW-B and steeply dipping (65-85°) towards NW (Précigout et al., 2013; Soustelle et al., 2009; Van Der Wal and Vissers, 1996, 1993; Vauchez and Garrido, 2001). Towards the contact, the foliation intensifies. The stretching lineation is sIn general, the samples display a NE-SW trending foliation dipping towards NW with subhorizontal to shallowly SW dipping (<20°) stretching lineation. The latterIt is defined by elongated orthopyroxene single crystals, neoblast tails of pyroxene porphyroclasts and olivine-rich lenses stretched in the foliation planeplain. Towards the contact to the bordering Jubrique metasediments (= NW-B), macroscopic evidence for increasing strain is an increase of porphyroclast elongation (Fig. 2) and an increase of the mylonitic matrix (Fig. 3Fig. 2). The elongation is mostly visible by tThe lengthening of orthopyroxene single crystals , which expands to aspect ratios > 10:1

260 and length of ~5 cm (Fig. 2). The increasing strain is additionally indicated by increasing deformation of partly garnet-bearing pyroxenites, by pinch-and-swell structures (~~Fig. 3~~Fig. 2D-i), and by boudinage described in detail by Précigout et al. (2013).
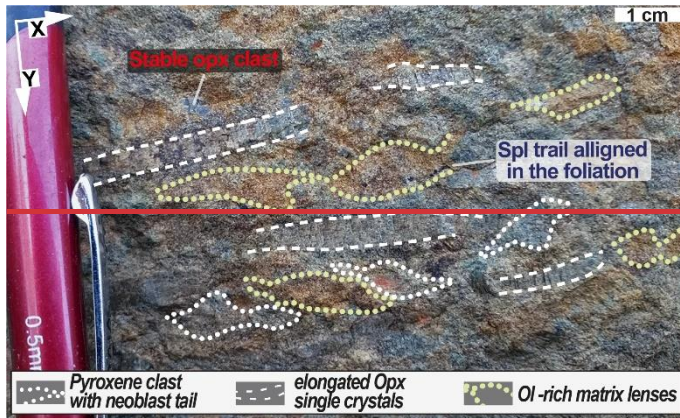
265

4.1 Microstructures

Figure ~~3~~2 gives a microstructural overview of representative thin sections with increasing distance to the ~~SZB~~NW-B. Due to serpentinization and to facilitate phase identification, BSE and Ca-EDX overview scans are shown instead of microscopic images. The proportion of neoblasts in the matrix increases towards the ~~shear zone boundary~~NW-B (~~Fig. 3~~Fig. 2).
270 Simultaneously, the abundance of porphyroclasts decreases. Nevertheless, deformation features like a clear foliation with marked elongation of porphyroclasts and recrystallized olivine dominated matrix are present in all mylonitic samples (39-502 m distance ~~SZB~~NW-B, ~~Fig. 3~~Fig. 2). Only the outermost, tectonic sample (703 m distance ~~SZB~~NW-B) lacks these features and shows a relatively undeformed fabric (~~Fig. 3~~Fig. 2F). Even though deformation was not as localized in this sample as in those situated closer to the ~~SZB~~NW-B, interstitial pyroxenes along olivine grain boundaries are present (~~Fig.~~
275 ~~3~~Fig. 2F-ii). Furthermore, layers consisting of a pyroxene and spinel assemblage crosscut the tectonic peridotite. Approaching the ~~SZB~~NW-B, pyroxene porphyroclasts show neoblast tails, which stretch out in the foliation. Simultaneously, pyroxenite layers turn parallel to the foliation and flatten till they disintegrate (~~Fig. 3~~Fig. 2D-ii) as described in detail in (Précigout et al.~~,~~ (2013).

With the focus on phase mixing as well as on reaction and recrystallization processes, we further investigated structures on
280 the micro-scale rather than on thin-section or larger scale. By microscopic analysis and the BSE/EDX element thin section overviews (~~Fig. 3~~Fig. 2) four major microstructural domains were identified: (1) Olivine-rich matrix, (2) mixed matrix, (3) clinopyroxene neoblast tails, and (4) orthopyroxene neoblast tails. In the following, their microstructural characteristics ~~of these four domains~~ are presented. Additional~~ly~~ ~~to these four main domains,~~ amphibole-clinopyroxenite veins investigated in three thin sections will be shortly addressed. For reasons of length and clarity, ~~only a selection of~~examples of microstructures

285 of each domain are shown which is shown in figures, pproviding e its main characteristics and an overview of each domain and their changes depending on the distance to the SZBNW-B. These figures include ODFs referring to the depicted microstructure. Graphs of the complete microstructural data are presented in Fig. 4figure 3. Average aspect ratios and average grain size are included only if enough grains were present for a valid statistical analysis (n> 20100). The presented results presented below include all analyzed microstructures of a given microstructural domain. The complete data is
290 attached as supplementary data (S2). Garnet, even if nominally present in a few maps (39 of 41563 analyzed grains), is excluded from further analysis because of its small abundance (< 0.1 % for all microstructural domains) and its susceptibility for mis-indexing with opx especially for small grains. Coarse grained garnet (ECD > 100 µm) was not present in the studied microstructures.
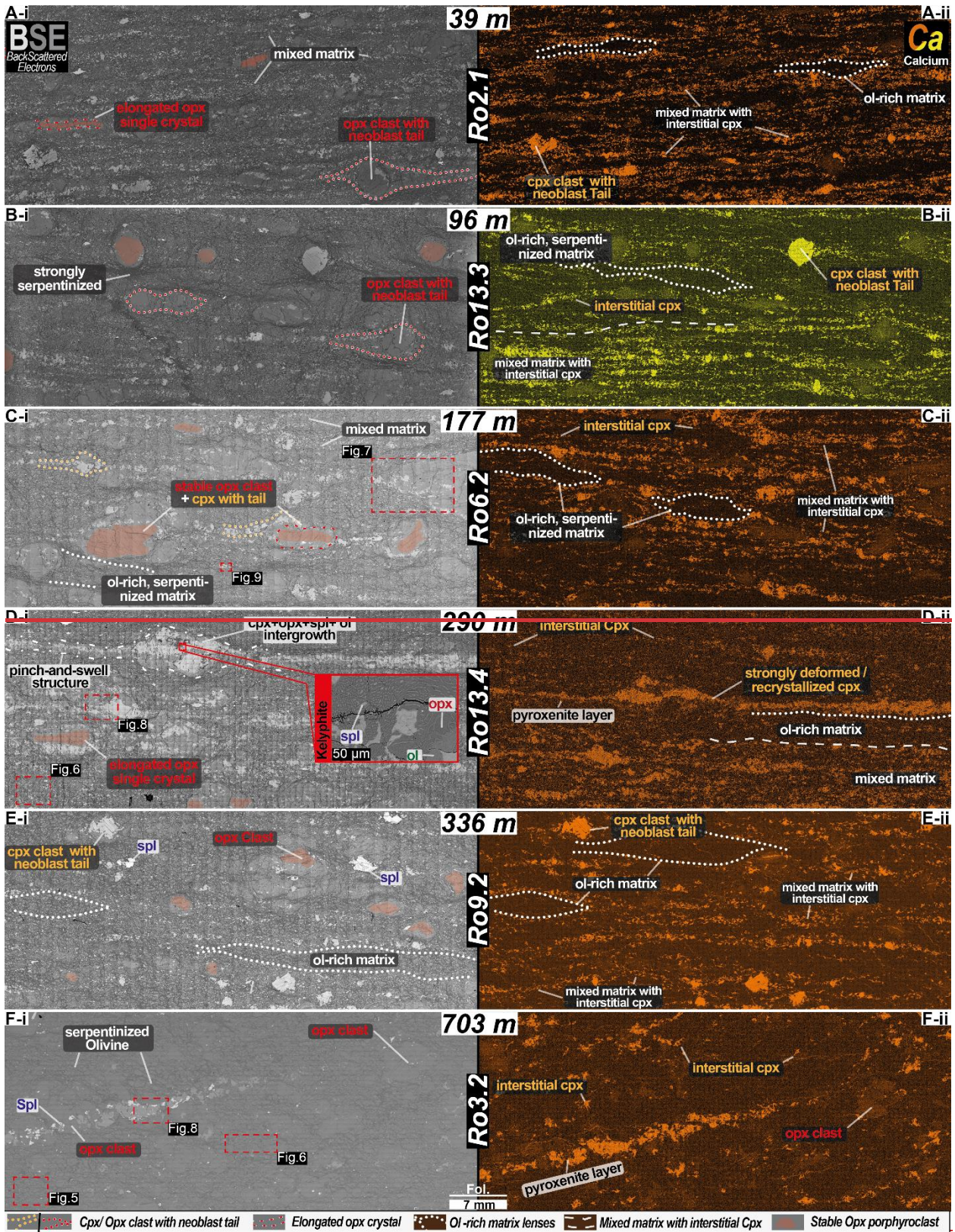
A-i BSE BackScattered Electrons — **39 m** — Ro2.1 — **A-ii** Ca Calcium
- mixed matrix
- elongated opx single crystal
- opx clast with neoblast tail
- mixed matrix with interstitial cpx
- ol-rich matrix
- cpx clast with neoblast Tail

B-i — **96 m** — Ro13.3 — **B-ii**
- strongly serpentinized
- opx clast with neoblast tail
- ol-rich, serpentinized matrix
- interstitial cpx
- cpx clast with neoblast tail
- mixed matrix with interstitial cpx

C-i — **177 m** — Ro6.2 — **C-ii**
- mixed matrix
- Fig.7
- stable opx clast + cpx with tail
- ol-rich, serpentinized matrix
- Fig.9
- interstitial cpx
- ol-rich, serpentinized matrix
- mixed matrix with interstitial cpx

D-i — **290 m** — Ro13.4 — **D-ii**
- cpx +opx +spl +ol intergrowth
- pinch-and-swell structure
- Fig.8
- Kelyphite
- opx
- spl
- ol
- 50 µm
- Fig.6
- elongated opx single crystal
- interstitial cpx
- strongly deformed / recrystallized cpx
- pyroxenite layer
- ol-rich matrix
- mixed matrix

E-i — **336 m** — Ro9.2 — **E-ii**
- cpx clast with neoblast tail
- spl
- opx Clast
- spl
- ol-rich matrix
- cpx clast with neoblast tail
- ol-rich matrix
- mixed matrix with interstitial cpx
- mixed matrix with interstitial cpx

F-i — **703 m** — Ro3.2 — **F-ii**
- serpentinized olivine
- opx clast
- spl
- opx clast
- Fig.8
- Fig.6
- Fig.5
- Fol.
- 7 mm
- interstitial cpx
- interstitial cpx
- opx clast
- pyroxenite layer

Legend: Cpx/ Opx clast with neoblast tail | Elongated opx crystal | Ol-rich matrix lenses | Mixed matrix with interstitial cpx | Stable opx porphyroclast

295
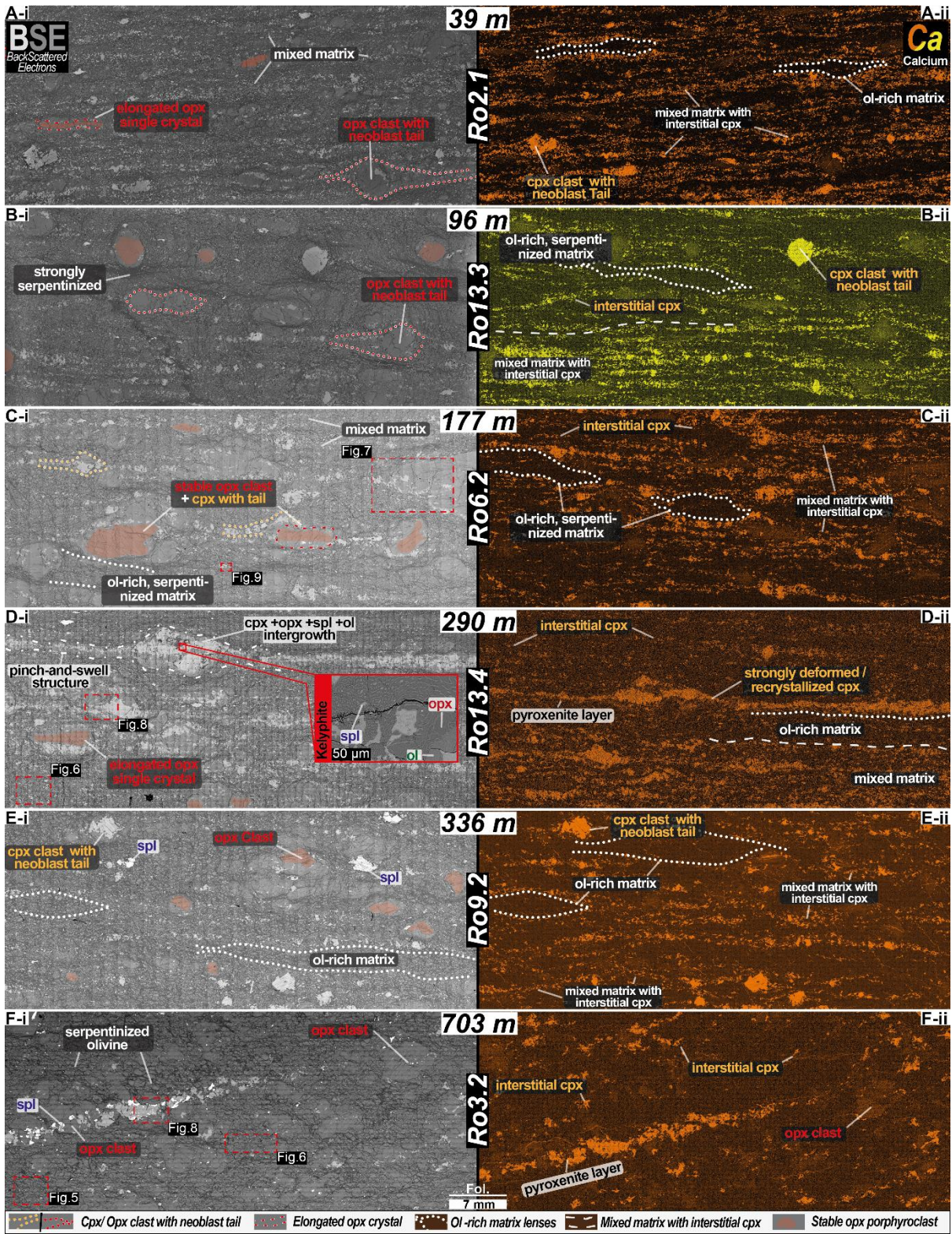
Fig. 23. Electron backscatter (left) and Calcium energy-dispersive X-ray spectroscopy (right) scans of the same thin sections ordered with increasing distance to the ~~shear zone boundary~~NW boundary of the Ronda peridotite (black numbers on white background). Locations of analyzed example microstructures and their figure # (5-9) are indicated. Dominant microstructural domains of the NW Ronda shear zone are marked: (1) strongly serpentinized olivine-rich matrix lenses, (2) mixed matrix with interstitial pyroxenes, (3) ortho- and (4) clinopyroxene porphyroclasts with neoblast tails. Note the presence of stable pyroxenes and elongated orthopyroxene. The presence of interstitial cpx (bright colours in EDX images) is indicative for the mixed matrix. D-i includes a close up on a kelyphitic assemblage.

300
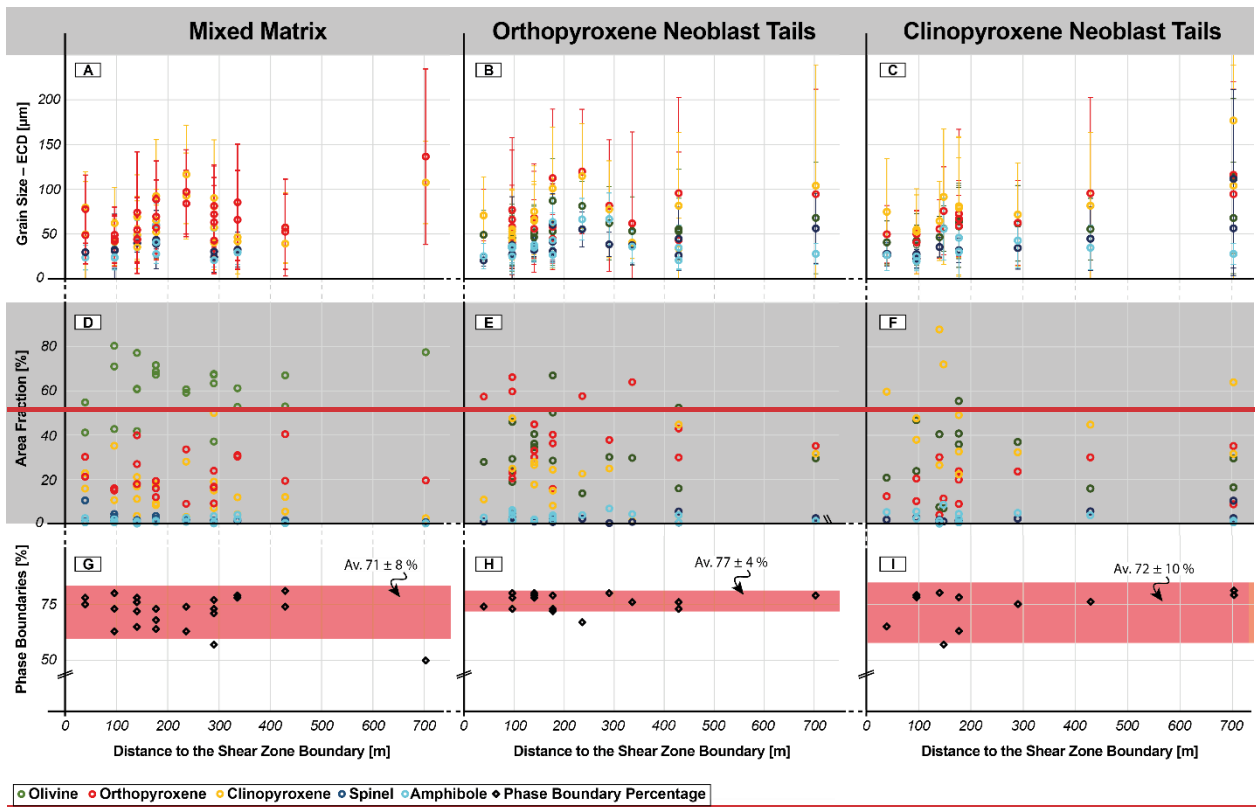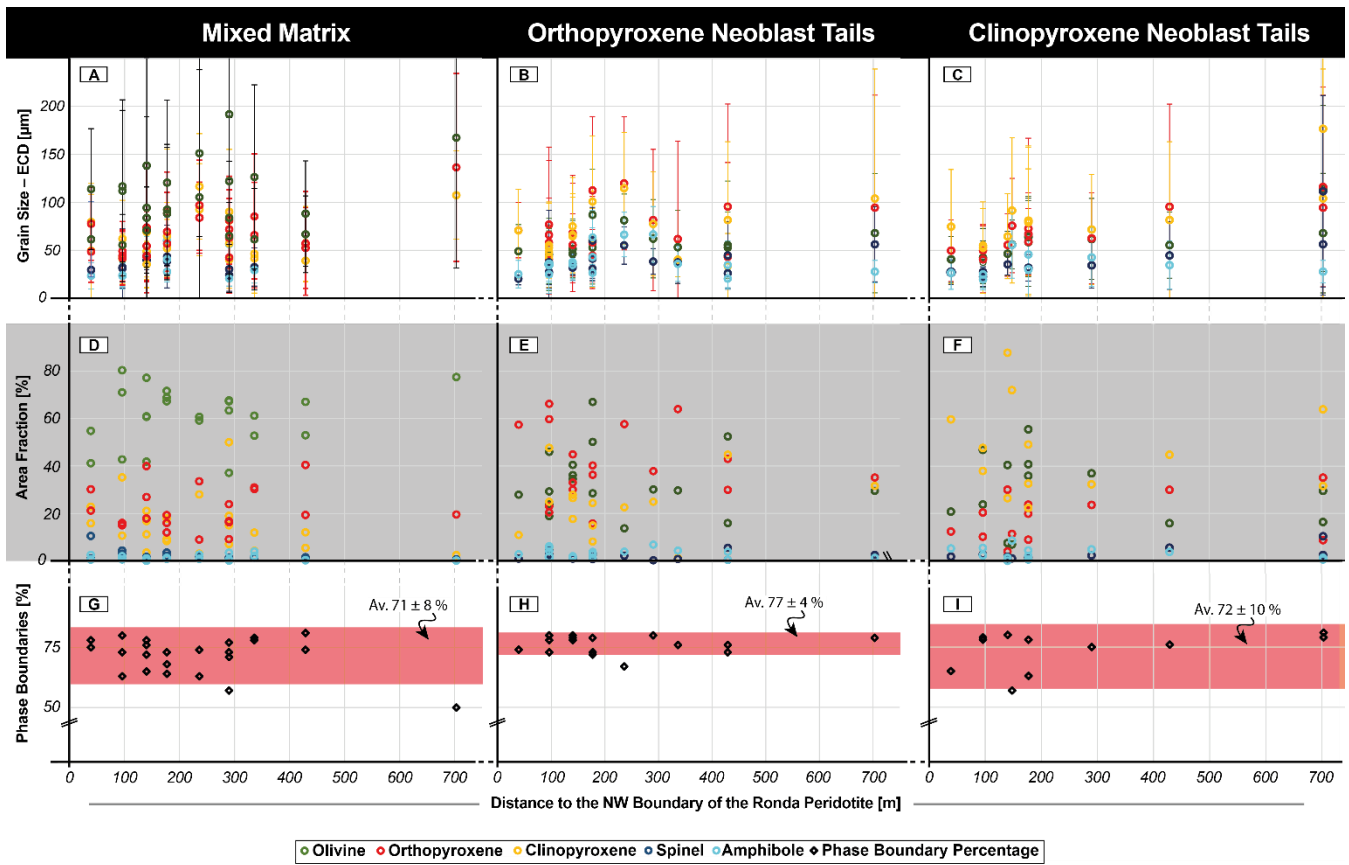
Fig. 34. Data overview of the major microstructural domains (mixed matrix, orthopyroxene and clinopyroxene porphyroclast neoblast tails) plotted against the distance to the ~~SZB~~NW-B. The olivine-rich matrix was excluded due to its small data base. Each data point represents the average grain size (A,B,C), area fraction (D,E,F) or phase boundary percentage of the total boundary length (G,H,I) of one EBSD map of an analyzed microstructure (e.g., Figs. 5-~~9~~8). The complete microstructural data is attached in supplementary data 2.
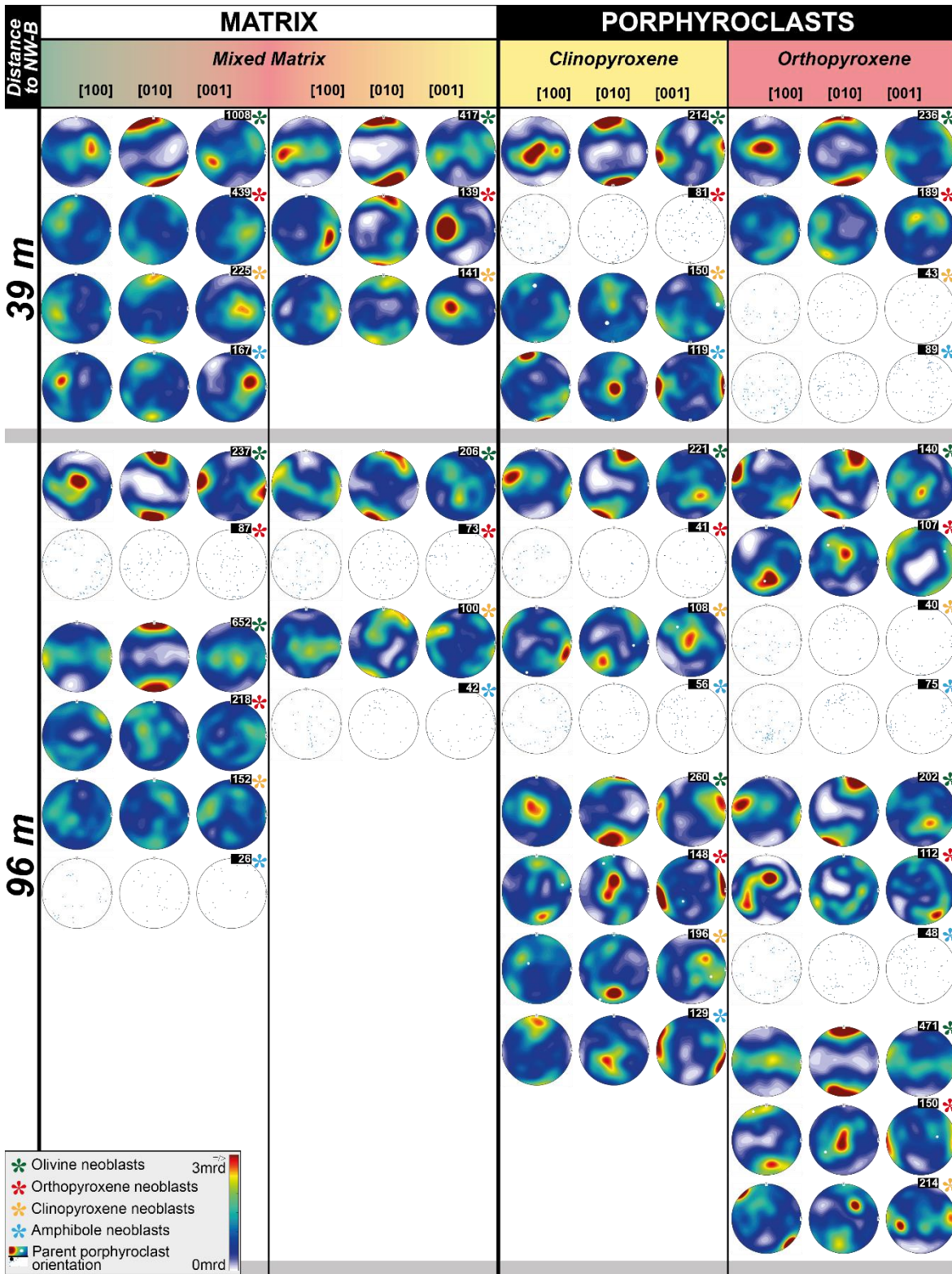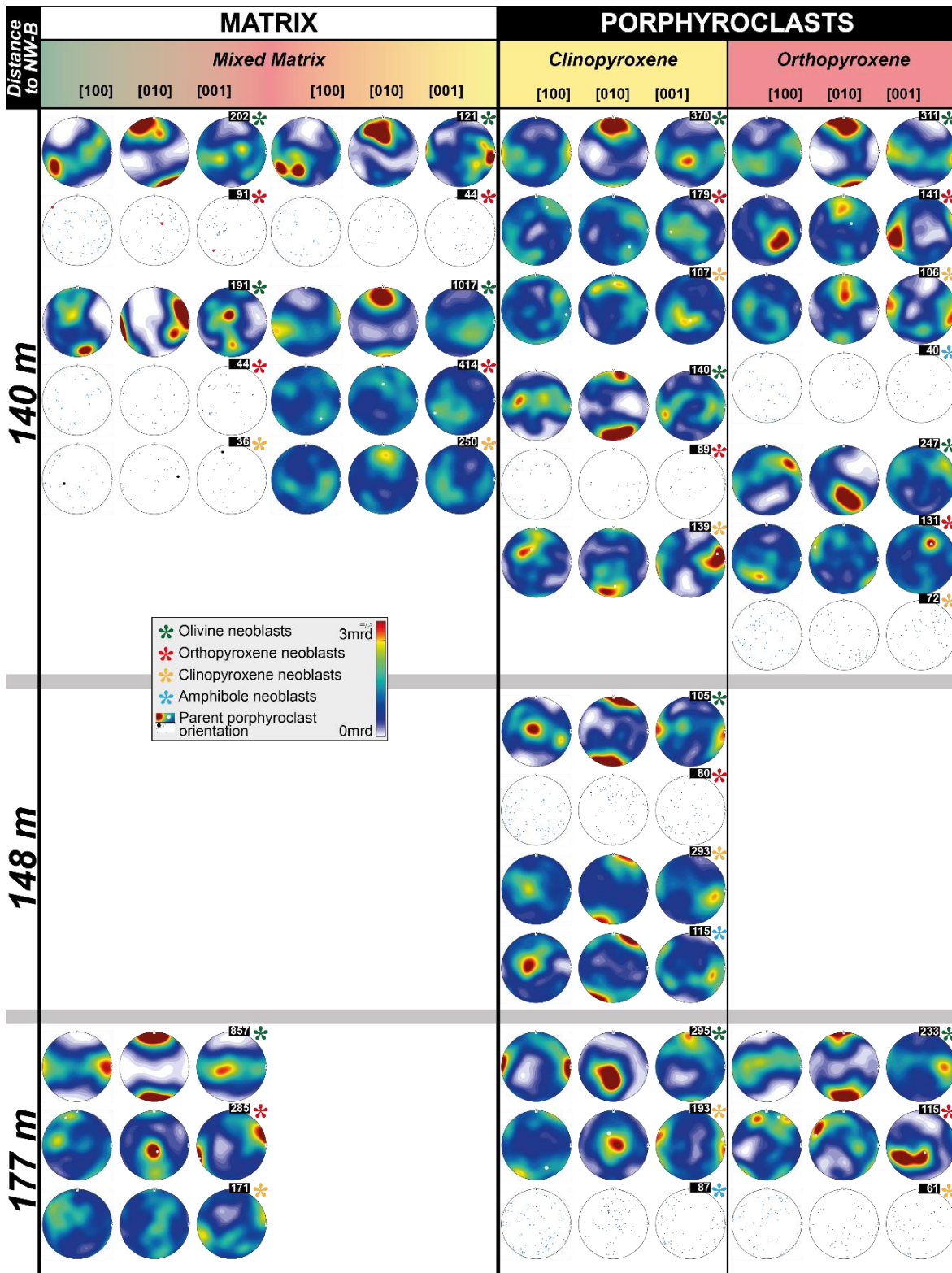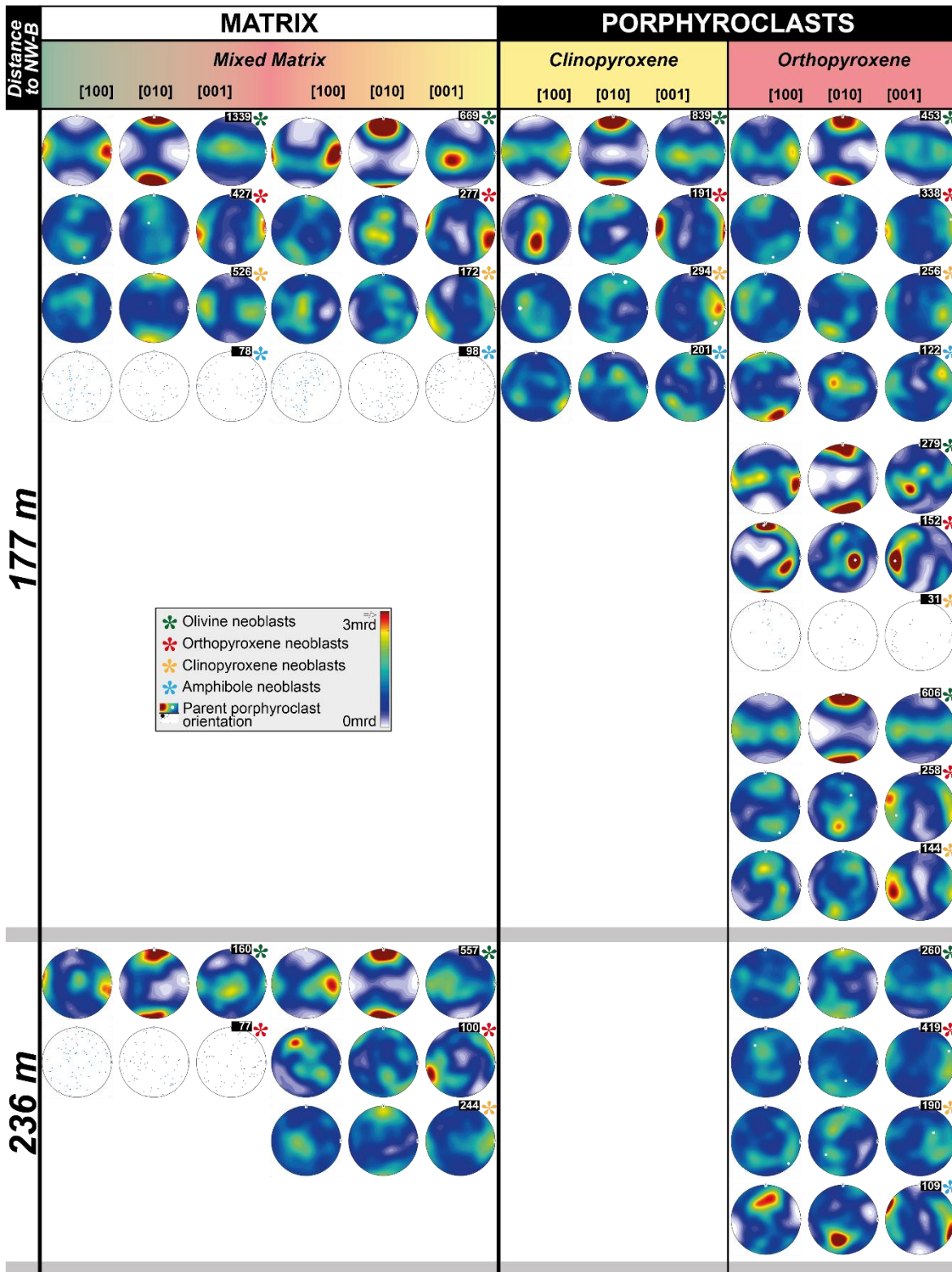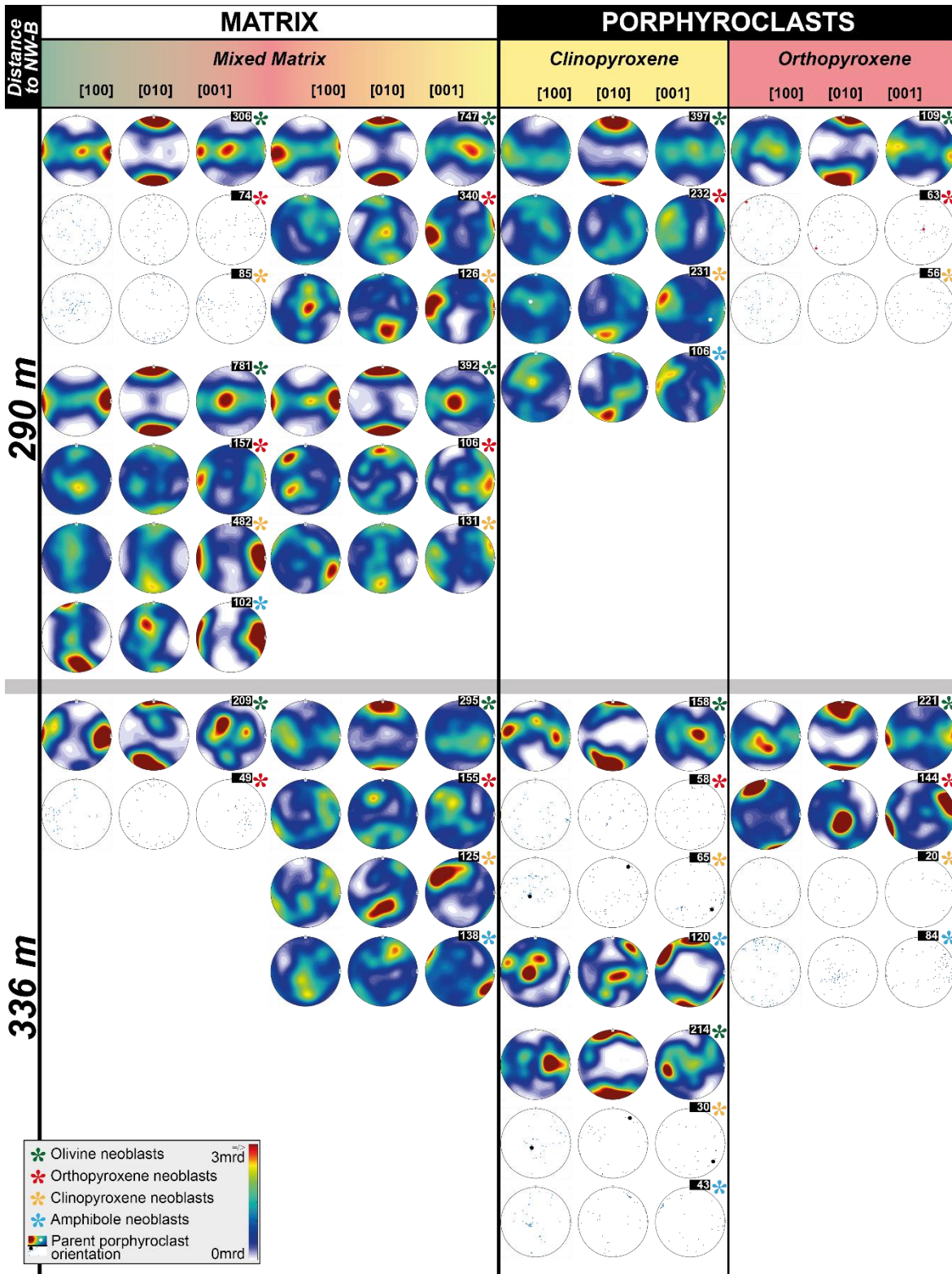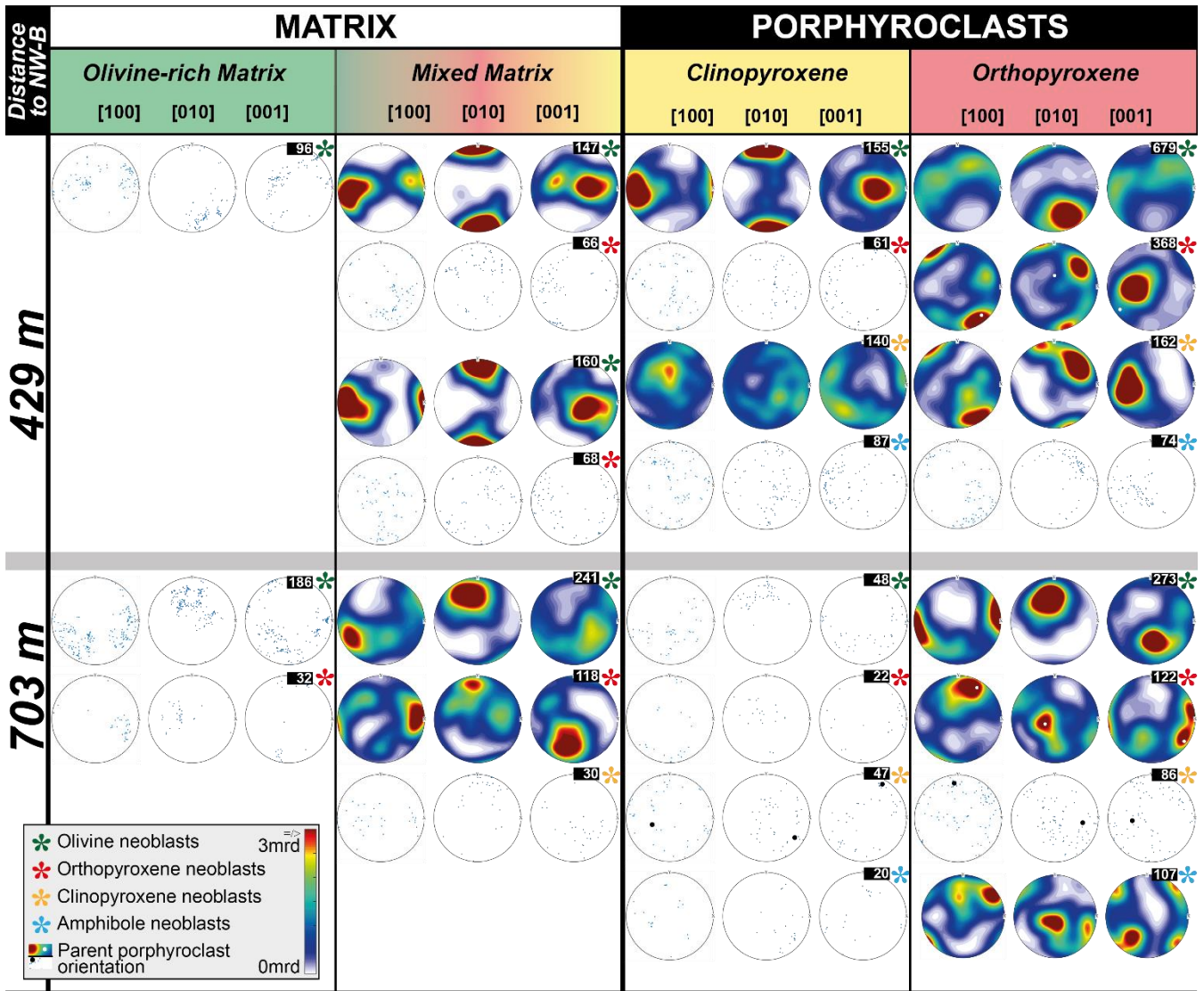
Fig. 4. Orientation data of all microstructural domains plotted per phase and EBSD map as lower pole figures of ODF (>100 grains) or dots of grain orientations (<100 grains). White numbers on black indicate number of grains analyzed for the specific phase. Phase is indicated by the color of the asterisk. Grouping of pole figures correspondents to the microstructure: Small spacing indicates neoblasts from the same microstructure.

4.1.1 Matrix domains

The overall olivine dominated matrix forms ~~the~~a major part of all analyzed samples (Fig. ~~3~~2). Due to the presence of interstitial cpx (high Ca counts in ~~Fig. 3~~Fig. 2) and opx, most of this matrix is mixed with only parts remaining almost monomineralic, olivine-~~-~~rich. ~~Even though~~Nevertheless, lenses of olivine-rich matrix domains are present in all samples (Fig. ~~2~~2). However, the differentiation between mixed domains and olivine dominated domains becomes increasingly difficult with decreasing distance to the ~~SZB~~NW-B. In both matrix domains olivine grains are cut by subvertical or

325 subhorizontal serpentine veins. With increased degree of serpentinization, olivine grain boundaries become increasingly lobate and originally coherent grains are separated into smaller fragments. Coherent crystallographic orientations with bended lattices over span multiple fragments, which were identified as single grains by the analysis of original EBSD analysis data (Fig. 5Fig. 5). Due to this discrepancy between calculated fragments grains and pristine grains, the EBSD data missing due to serpentinization were filled by applying a half quadratic filter. On base of the restored data grain

330 reconstruction of the original grain size could be achieved. Even though this method restores the pristine grain size and preserves the crystal orientations (Fig. 5; (Bergmann et al., 2016)), minor deviations in the shape of the grain boundary might occur.

pre-serpentinization grains, the grain properties (size, aspect ratio etc.) of the calculated grains of olivine are excluded from further analysis.

335 **4.1.1.1 Olivine-rich matrix**
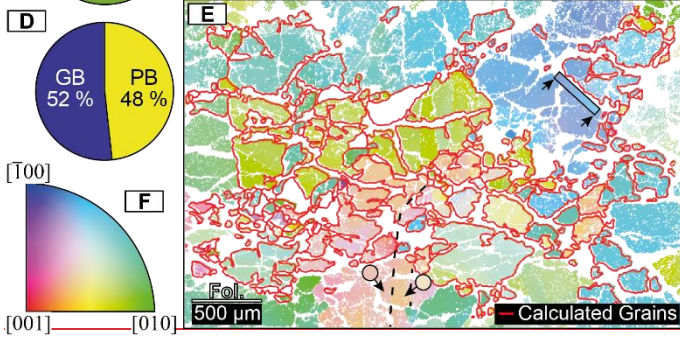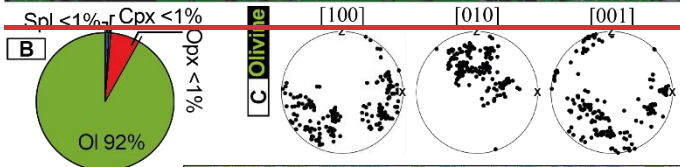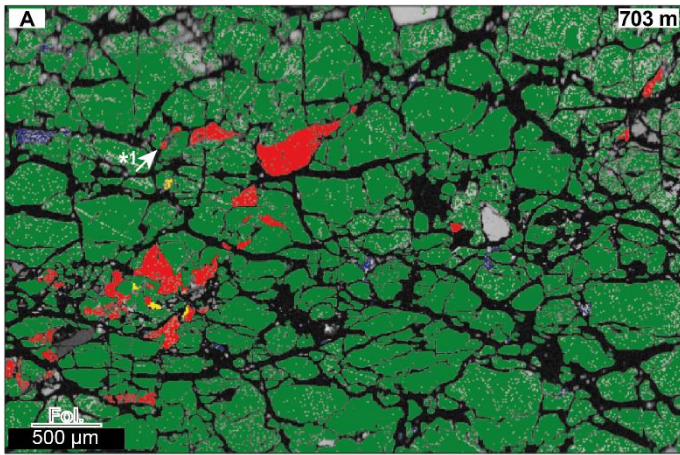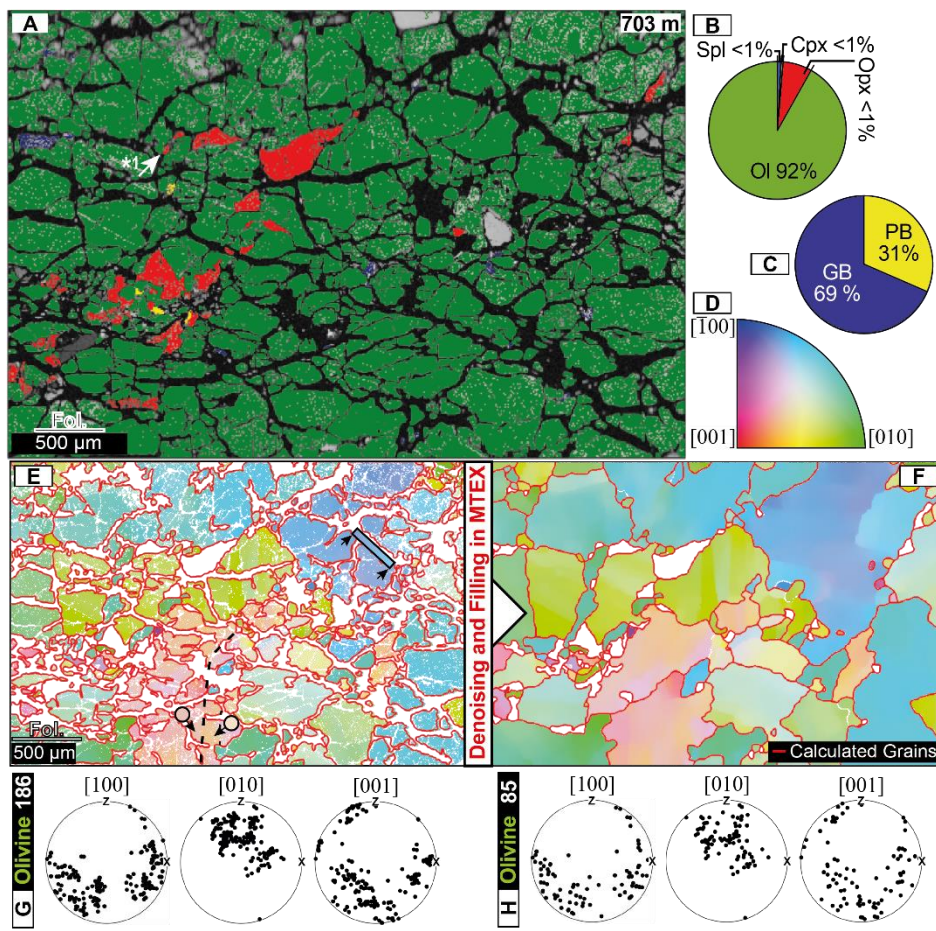
Fig. ~~Fig.~~ Fig. 5~~5~~. **A: Example microstructure of olivine-rich matrix in sample from 703 m distance to the ~~SZB~~NW-B. Area percentages (B), ~~orientations of calculated olivine grains (C), and~~ phase and grain boundary percentages (~~D~~C) are given in pie charts. The olivine orientation colour key for maps E & F is given in D. EBSD data reconstruction and denoising, optimized for olivine, is shown in E-H. E: Original ol orientations data with calculated grain boundaries (red). Examples of intracrystalline deformation by bending of the crystal lattice (box) and subgrain boundary (dashed line) covering and crossing multiple calculated fragmental grains are annotated. F: Denoised and filled ol orientation map with calculated grain boundaries (red). Olivine orientation plots of original (G) and reconstructed data (H).~~The orientation map of olivine (E) shows the areas of original grains identifiable by similar orientations. Examples of intracrystalline deformation by bending of the crystal lattice (box) and subgrain boundary (dashed line) covering and crossing multiple calculated fragmental grains (red outlines) are annotated. The orientation colour key is given in F.~~**

Due to the increased serpentinization in olivine-rich domains and ~~due to the~~ pervasive occurrence of pyroxenes as interstitial grains and on olivine grain boundaries only two microstructures of the olivine~~-~~-rich matrix type could be analyzed (e.g., ~~Fig. 5~~Fig. 5). They consist of on average ~~93~~83 % olivine (range ~~92~~77-~~84~~89), ~~6~~15 % opx (range ~~6~~9-~~7~~21) and minor spinel (~~1~~2 %) and cpx (< 1 %). The average reconstructed olivine grain size is 107 μm (range 103-112; S2). With on average 17 % secondary phases, 31,5 % of the total boundary length are phase boundaries. The crystallographic orientations of the olivines are predominantly parallel to each other (~~S3~~Fig. 4). ~~Areas of parallel orientations include multiple of calculated olivine grains (Fig. 5). In cases, b~~Bended lattices ~~or~~ and/or subgrain boundaries ~~can be traced over the boundary of calculated~~

355 ~~grains~~are often present (~~Fig. 5~~Fig. 5 – box and dashed line). ~~Even if statistically not verifiable, the size of these olivine areas which, in the opinion of the authors, represent the original grains prior to crosscutting serpentinization, was estimated to be several cm (Fig. 5).~~ Cracks within those original grains ~~and along their boundaries~~ are filled with serpentine (~~Fig. 5~~Fig. 5). Orthopyroxenes within the olivine-dominated matrix are oriented with their [001] axis perpendicular to the foliation plane (~~Fig. 4~~S3).
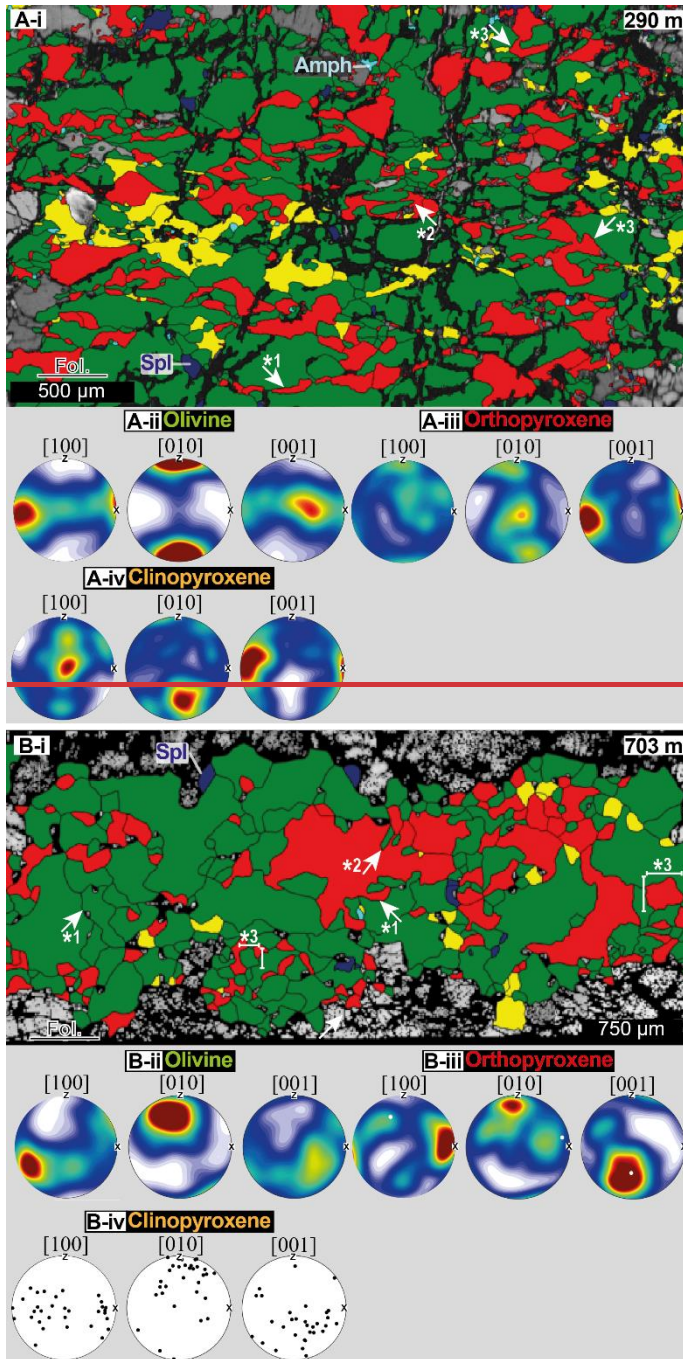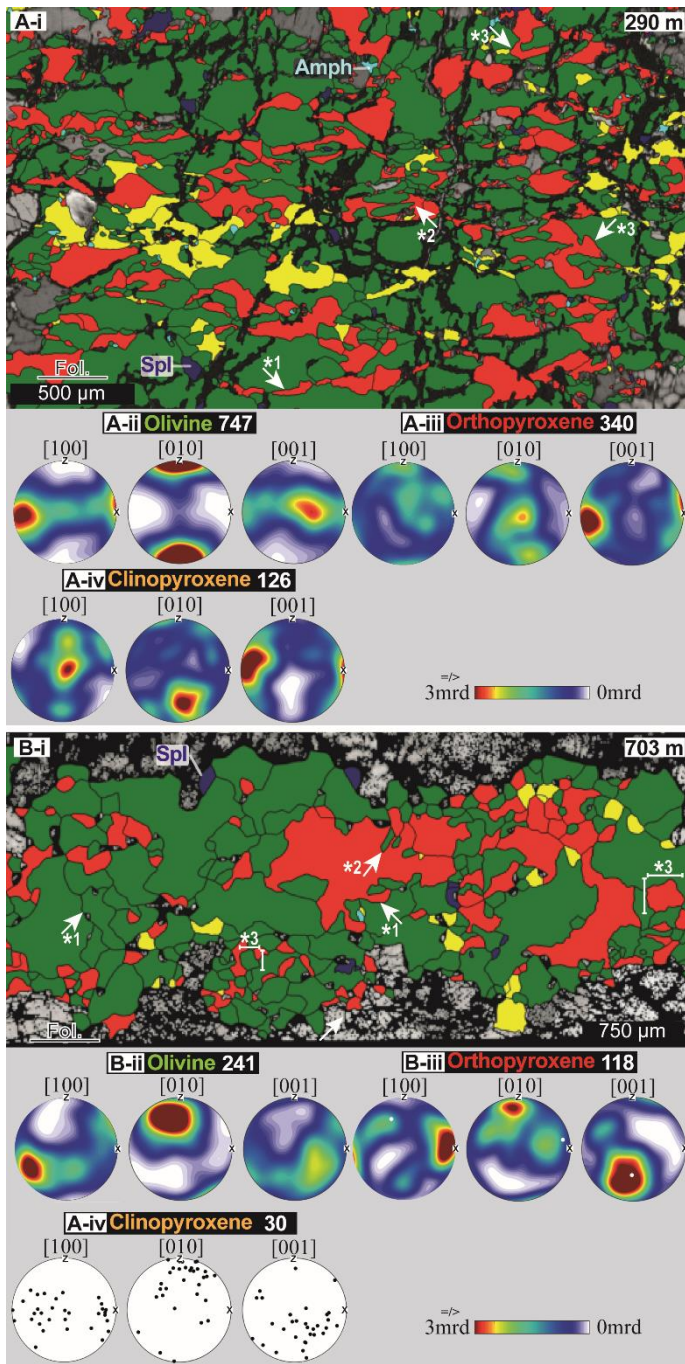
 4.1.1.2 Mixed matrix

Fig. Fig. 66. Example microstructures of the mixed matrix in 290 m (A-i) and 703 m (B-i) distance to the ~~SZB~~NW-B. A: Mixed matrix with wedge/film-shaped orthopyroxene (*1) in between coarser olivine, indentations (*2) and highly irregular phase boundaries (*3). CPOs of olivine (A-ii), orthopyroxene (A-iii) and clinopyroxene (A-iv). B: Mixed matrix of a tectonite sample with highly lobate grain and phase boundaries (*1), indentations (*2) and equi-axial grain shape (*3). CPOs of olivine (B-ii) and orthopyroxene (B-iii) and pole figure of clinopyroxene orientations (A-iv).

365
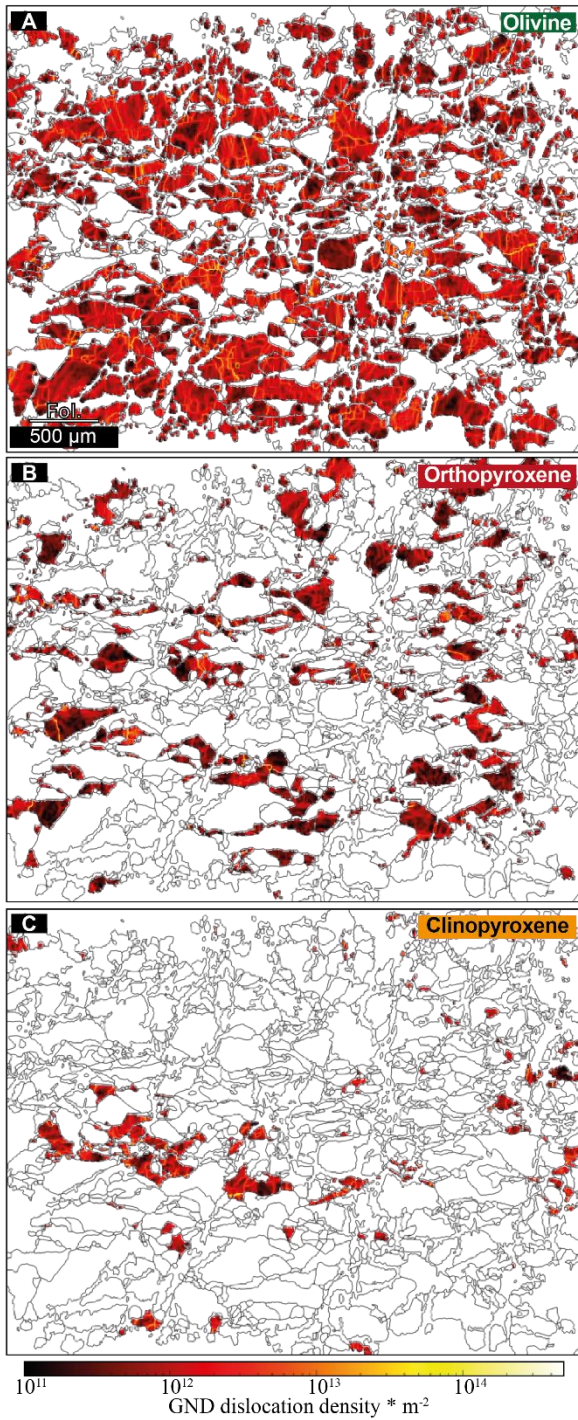
Fig. 7. Geometrically necessary dislocation (GND) density maps for olivine (A), orthopyroxene (B) and clinopyroxene (C) of the mylonitic mixed matrix shown in figure 6A-i. Note grain internal deformation in all phases and the formation of subgrain boundaries visible by bright yellow lines.

370

The microstructures of 23 mixed-matrix domains were analyzed either as subsets of EBSD maps covering pyroxene porphyroclast tail assemblages with adjacent matrix or as individual map. The subsets only consist of the mixed matrix surrounding the porphyroclast-tail assemblage. As mixed matrix microstructures are present in the entire transect (703 to 29 m distance to ~~SZB~~NW-B), they are present in both mylonitic and tectonite samples. Characteristic for the mixed matrix are small, interstitial and irregular/highly lobate pyroxene grains in between coarser grained olivine (~~Fig. 6~~Fig. 6). The grain shape of pyroxenes and olivine varies between rather equi-axial in tectonic samples (~~Fig. 6~~Fig. 6B-i) to elongated olivines and film/wedge-shaped pyroxenes in mylonitic samples (~~Fig. 6~~Fig. 6A-i). The long side of film-like pyroxenes is mostly parallel to the foliation. Bigger ~~P~~pyroxenes have in general ~~a~~ highly irregular grain shape_s and protrusions_ which form intergrow ~~and show in places intergrow~~ patterns with _bordering_ olivine_s_ (~~Fig. 6~~Fig. 6A-i *~~2~~1). _Indentations of olivine neoblasts in bigger pyroxenes are commonly observed (Fig. 6A-i *2)._ ~~The~~ The mineralogical assemblage of the mixed matrix is in general constant for the entire data set and consists of olivine (av. 61 %, range 37-80 %), orthopyroxene (av. 22 %, range 9-40 %), clinopyroxene (av. 14 %, range 2-50 %) and spinel (av. 2 %, range 0-10 %) with occasional amphibole (av. 1 %, range 0-4 %) (~~Fig. 4~~Fig. 3D). Spinel is present as interstitial grains. Phase abundances vary depending on the microstructural setting within one sample but do not significantly change over the distance to the ~~SZB~~NW-B (~~Fig. 4~~Fig. 3D). Similar to the olivine-rich matrix, former coarse grained olivines are cut by serpentine veins. Only in phase mixtures olivine grains are less effected by the serpentinization. Average grain sizes (ECD) are 67 µm for opx (range 42-136), 64 µm for cpx (range 35-117), 41 µm for spinel (range 24-90) and 40 µm for amphibole (range 21-60) (~~Fig. 4~~Fig. 3A, S2). _Reconstructed olivine grains form in all investigated thin sections and with on average 103 µm (range 55-192) ECD the biggest grains._ Almost over the entire mylonitic transect (39-429 distance to the ~~SZB~~NW-B) grain sizes of _all phases of_ the mixed matrix are similar within uncertainty (1σ, ~~Fig. 4~~Fig. 3A). Only around ~250 m distance to the ~~SZB~~NW-B, the grain size of both pyroxenes shows an excursion towards coarser sizes. Mixed matrix pyroxenes in the tectonite regime (~~Fig. 6~~Fig. 6B-i) have coarser grain sizes (~~Fig. 4~~Fig. 3A). Average aspect ratios are _2.03 ±.1 for reconstructed ol,_ 1.9 ±.2 for opx, 1.9 ±.3 for cpx, 1.8 ±.1 for spinel and 1.8 ±.2 for amphibole (S2). In contrast to the grain sizes, the average aspect ratios remain constant over mylonites and tectonites (S2). 71 ±8 % of the total boundary length are on average phase boundaries (29 % grain boundaries). Apart from one outlier, all mylonitic mixed matrix domains share this distribution. In the tectonite, phase boundaries only form 50 % of the total boundary length. On average 40 % of the total boundary length are olivine-opx boundaries with 48 % of the entire olivine boundaries and 79 % of all opx boundaries being olivine-opx boundaries. Despite the lower abundance of cpx, amphibole forms more phase boundaries with cpx (29 %) than with opx (16 %).

Olivine CPOs are moderate (av. max mrd 10, av. ~~M index~~M=-0.1~~7~~6). Overall, the A-type olivine CPO is dominant (18 of 23 mixed matrix microstructures_; Fig. 4_). However, transitions to the AG-type by [100] and [001] forming girdles in the foliation plane are present with variable strength (clear AG-type CPO n=3). Clear B-types_, which were also reported by_ ~~(~~Précigout _and_~~&~~ Hirth~~,~~ (2014) are ~~also~~ present in the two samples situated closest to the ~~SZB~~NW-B. Orthopyroxene CPOs are with an average maximum mrd of 8 and an average M-index of 0.0~~4~~6 the weakest opx CPOs of all investigated domains. In most cases, orthopyroxene's [001] axes are parallel to the lineation. The CPO of opx neoblasts is in places affected by the

orientation of larger opx grains within the mixed matrix (~~Fig. 6~~Fig. 6B-iii). Clinopyroxene CPOs are weak with an average M-index of 0.0~~5~~9 (av. max mrd 18). In most cases, both pyroxenes are oriented parallel to each other and show similar intensities (mrd, ~~M-index~~M) for a given microstructure. In some cases, maxima of pyroxene [100] and [010] orientations are flipped in the sense that clinopyroxene [100] maxima are parallel to orthopyroxene [010] maxima, and cpx [010] display

410   orientations similar to opx [100] (e.g., ~~Fig. 6~~Fig. 6A-iii/iv). Only in four mixed matrix microstructures enough amphibole grains are present to determine a CPO (Fig. 4~~S3~~). In general, amphibole orientations are parallel to the present pyroxene and its [001] axes are aligned parallel to the lineation. Neoblasts of ortho- and clinopyroxene and in particular olivine have a high dislocation density, in places concentrated into sub-grain boundaries (Fig. 7).

4.1.2 Porphyroclast tails

415   Porphyroclasts are present in all mylonitic samples (~~Fig. 3~~Fig. 2). In the tectonite sample, the small difference between grain sizes of matrix and porphyroclasts does not allow a clear differentiation between both (~~Fig. 3~~Fig. 2F). Here, pyroxene is either present in layers consisting of both pyroxenes, spinel and minor olivine (~~Fig. 8~~Fig. 9B-i), as clasts, or (~~Fig. 3~~Fig. 2F-i/ii) as interstitial pyroxenes along grain boundaries of olivine clasts (~~Fig. 6~~Fig. 6B-i). The pyroxene porphyroclasts in tectonites are predominantly orthopyroxenes. In mylonitic samples, the contrast between porphyroclasts and matrix is

420   marked by their strongly differing grain sizes (~~Fig. 3~~Fig. 2A-E). Most porphyroclasts are pyroxenes. Often assemblages of intergrown pyroxenes ± spinel form porphyroclastic assemblages (~~Fig. 3~~Fig. 2D-i). These assemblages are predominantly present in deformed pyroxenitic layers or in areas with an increased pyroxene proportion (~~Fig. 3~~Fig. 2C-i lower image half). Occasionally, also garnet surrounded by kelyphitic rims or coarse spinel grains (Fig. 2E-i) form porphyroclasts. As both pyroxenes are present as (porphyro)clasts in tectonites and mylonites, their microstructures were analyzed from 29 to 703 m

425   distance to the ~~SZB~~NW-B. In mylonitic samples, both pyroxenes show the formation of neoblast tails (~~Fig. 3~~Fig. 2A-E). Common characteristics of pyroxene neoblast tails are a mixed phase assemblage of both pyroxenes, olivine, amphibole and spinel. The affiliation of neoblast tails to the parent porphyroclasts is given by the contrast in phase composition and neoblast grain shape between tail and surrounding matrix as well as by neoblast indentations into the parent porphyroclast (Figs. 7,8).

4.1.2.1 Orthopyroxene porphyroclasts
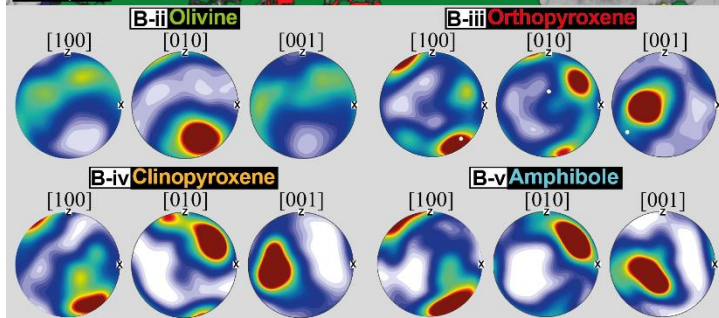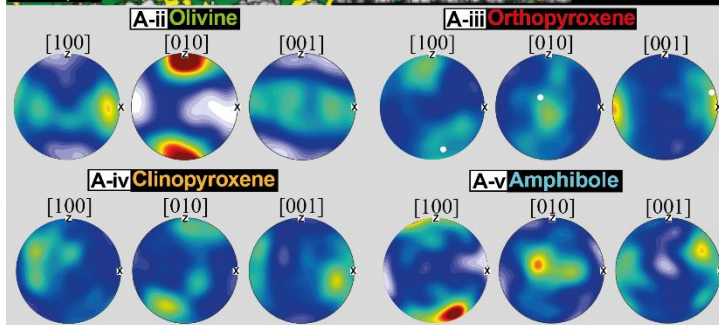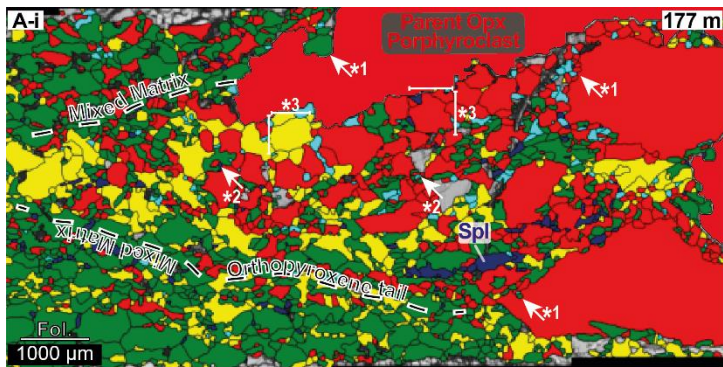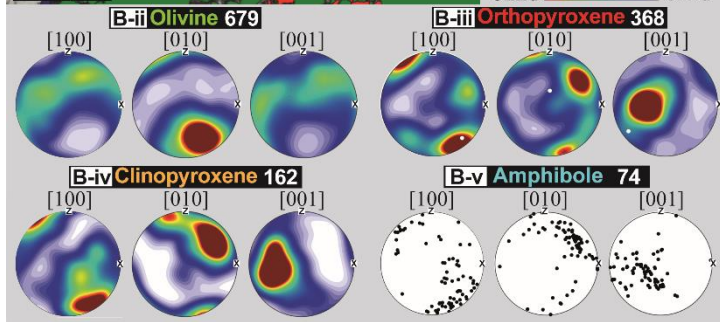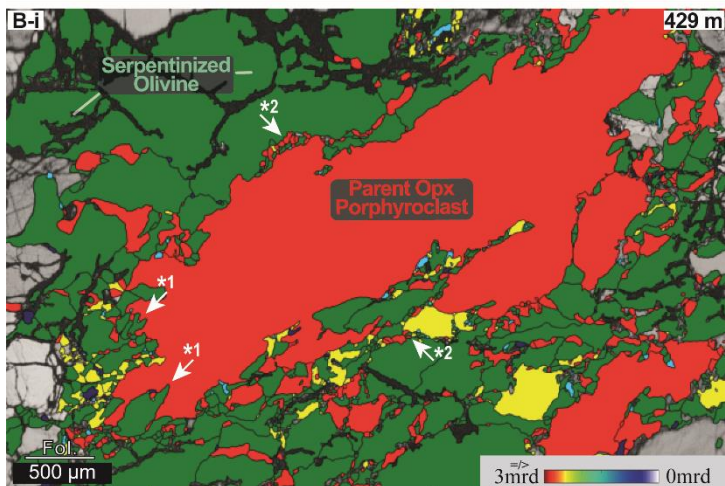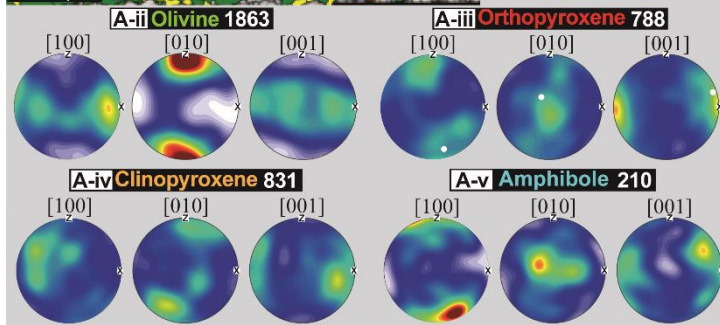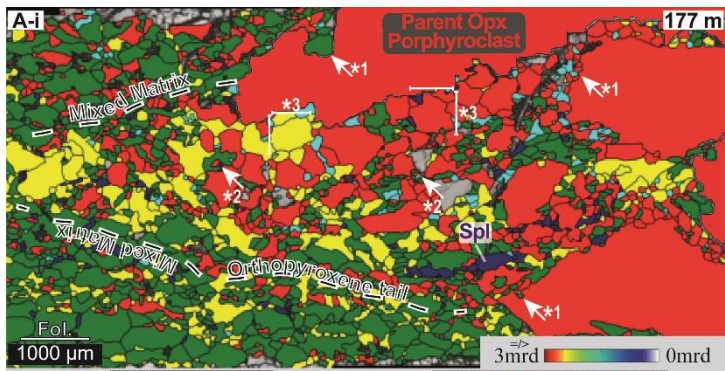
Fig. 7Fig. 8. Example microstructures of orthopyroxene porphyroclasts with neoblasts in 177 m (A-i) and 429 m (B-i) distance to the SZBNW-B. A: Neoblast tail of opx and subordinate cpx porphyroclast assemblage. Annotated are neoblast indentations in parent porphyroclasts (*1), interstitial amph and spl (*2) and equi-granular grain shape (*3). Note the difference in phase composition and abundances, grain size and shape between neoblast tail and surrounding mixed matrix. CPOs of all present phases are given in A ii-v with white dots in A-iii indicating the parent clast orientation. B: Orthopyroxene porphyroclast with neoblast indentations (*1) and fine-grained mixed neoblast assemblages at its boundary (*2). Note the presence of fine-grained mixed neoblast along grain boundaries of the surrounding coarse olivine. CPOs of all present phases are given in B ii-v with white dots in B-iii indicating the parent clast orientation.

Orthopyroxene clasts (tectonites) and porphyroclasts (mylonites) are present in all samples. Their shape is variable (Fig. 3Fig. 2). However, towards the SZBNW-B highly elongated porphyroclasts (aspect ratios > 1:10) become more abundant. Neoblast formation around opx porphyroclasts is present in all mylonitic samples. Common characteristics of neoblasts are low internal deformation, equi-axial grain shape and often irregular boundaries (Fig. 7Fig. 8). In the distal part of the mylonite unit close the tectonites, the formation of neoblasts is weaker and rather arranged in diffuse patches around the porphyroclast (Fig. 7Fig. 8B-i). Neoblast assemblages are present at the parent clast grain boundary and extend along grain boundaries into the surrounding coarse-grained olivines (Fig. 7Fig. 8B-i). With decreasing distance to the SZBNW-B, opx porphyroclast neoblast assemblages become more abundant and form tails within the foliation (Fig. 7Fig. 8A-i). The mineralogical assemblage of these domains consists of orthopyroxene (av. 41 %, range 16-66), olivine (av. 34 %, range 14-67), clinopyroxene (av. 20 %, range 1-48), amphibole (av. 3 %, range 1-7) and spinel (av. 2 %, range 1-6) (Fig. 4Fig. 3E). Spinel and especially amphibole form mostly interstitial grains. There are no clear trends in the phase assemblage related to the distance to the SZBNW-B (Fig. 4Fig. 3E). Amphibole and spinel are constantly present as secondary phases with standard deviations of ±2 % (amph) and ±1 % (spl) (Fig. 4Fig. 3E). For olivine and both pyroxenes, phase abundances in opx neoblast tails can vary in a single thin section in the same magnitude as over the entire shear zone transect. Average grain sizes are 69 µm for opx (range 41-120), 54 µm and reconstructed ol (range 3853-8199) for olivine, 66 µm for cpx (range 34-115), 37 µm for amphibole (range 21-67) and 36 µm for spinel (range 20-56) (Fig. 4Fig. 3B). Apart from one excursion at around 250 m distance to the SZBNW-B, the grain sizes are largely constant throughout the entire transect (Fig. 4Fig. 3B). For a given opx tail, grains of both pyroxenes and reconstructed olivine are mostly similar sized (± 10 µm). Amphibole and spinel have similar, small grain sizes with ECDs in general half the size of pyroxene neoblasts. Average aspect ratios are with 1.8 for opx, 1.9 for olivine, 1.8 for cpx, 1.8 for amphibole and 1.9 in general lower than in matrix domains (S2). In contrast to the grain size, aspect ratios remain constant in all mylonitic samples. In the tectonite, the average aspect ratios are highertend to be higher (S2). Phase boundaries clearly dominate (77 ±4 %) over grain boundaries (Fig. 4Fig. 3H). Apart from one outlier, these high phase boundary percentages are present over the entire shear zone (Fig. 4Fig. 3H). Although opx is mostly the predominant phase, olivine forms, on average, most of the phase boundaries (S2). Olivine neoblast CPOs are the weakest for all microstructural domains (av. max mrd 9, av. M indexM=-0.14). Dominant is the AG-type CPO with girdle distributions of [100] and [001] in the foliation plane (n=11; Fig. 4S3). Transitions to A- or B-type CPOs are formed by point maxima in these girdles (Fig. 7Fig. 8A-ii). Two clear A- and B-type CPOs are present for olivine neoblasts in opx tails (Fig. 4S3). Orthopyroxene neoblasts have the strongest opx CPOs of all microstructural domains (av. max mrd 12, av.

M indexM=–0.079). For almost all orthopyroxene porphyroclast-neoblast assemblages, opx neoblast CPOs are strongly dependent on the parent clast orientation (e.g., Fig. 7Fig. 8A/B-iii). This porphyroclast dependence is present in both strong and weak CPOs of orthopyroxene neoblasts. The common orthopyroxene CPO is [001] parallel to the lineation. The [100] and [010] maxima do not show such a clear trend. Clino- and orthopyroxene CPOs are always for [001] and predominantly for [100] and [001] parallel to each other (e.g., Fig. 7Fig. 8B-iii/iv). With an average maximum mrd of 19 and an average M-index of 0.192 cpx neoblasts in opx porphyroclast tails form the strongest clinopyroxene CPOs of all microstructural domains. For all orthopyroxene tails, amphibole CPOs are related to the orthopyroxene neoblast CPOs and thereby also parallel to the parent clast orientation (e.g., Fig. 7Fig. 8A/B-v).

470

475

4.1.2.2 Clinopyroxene porphyroclasts
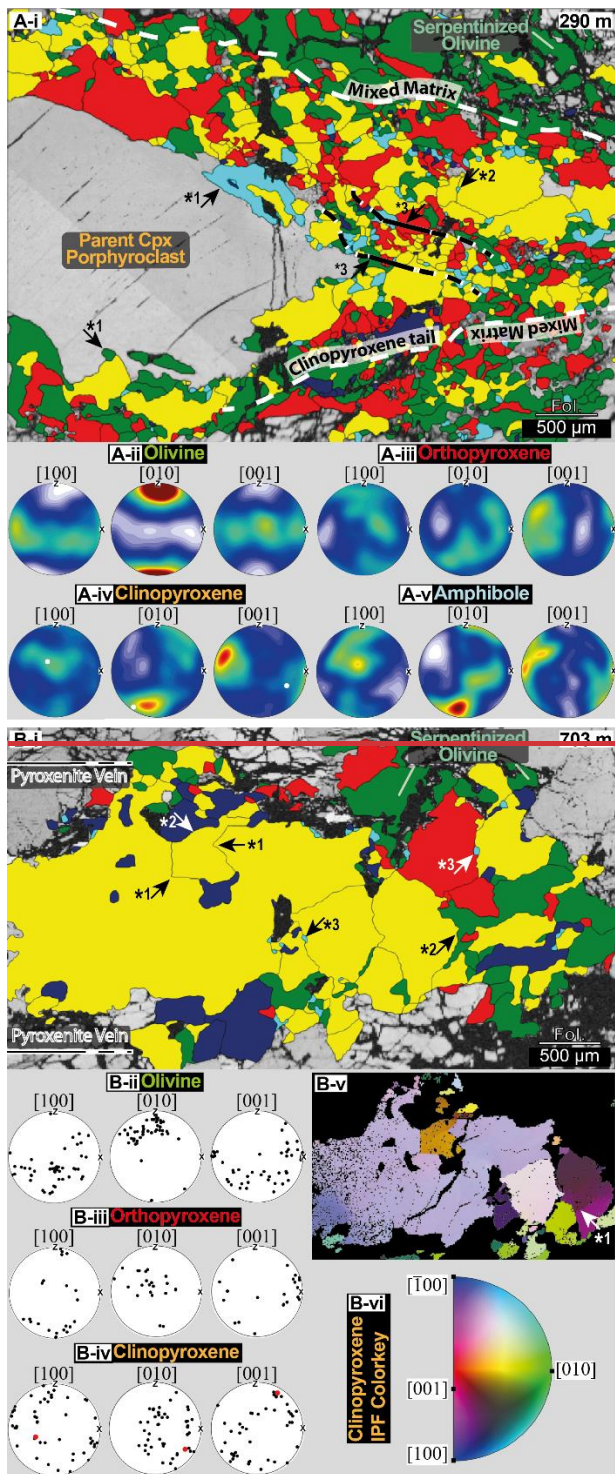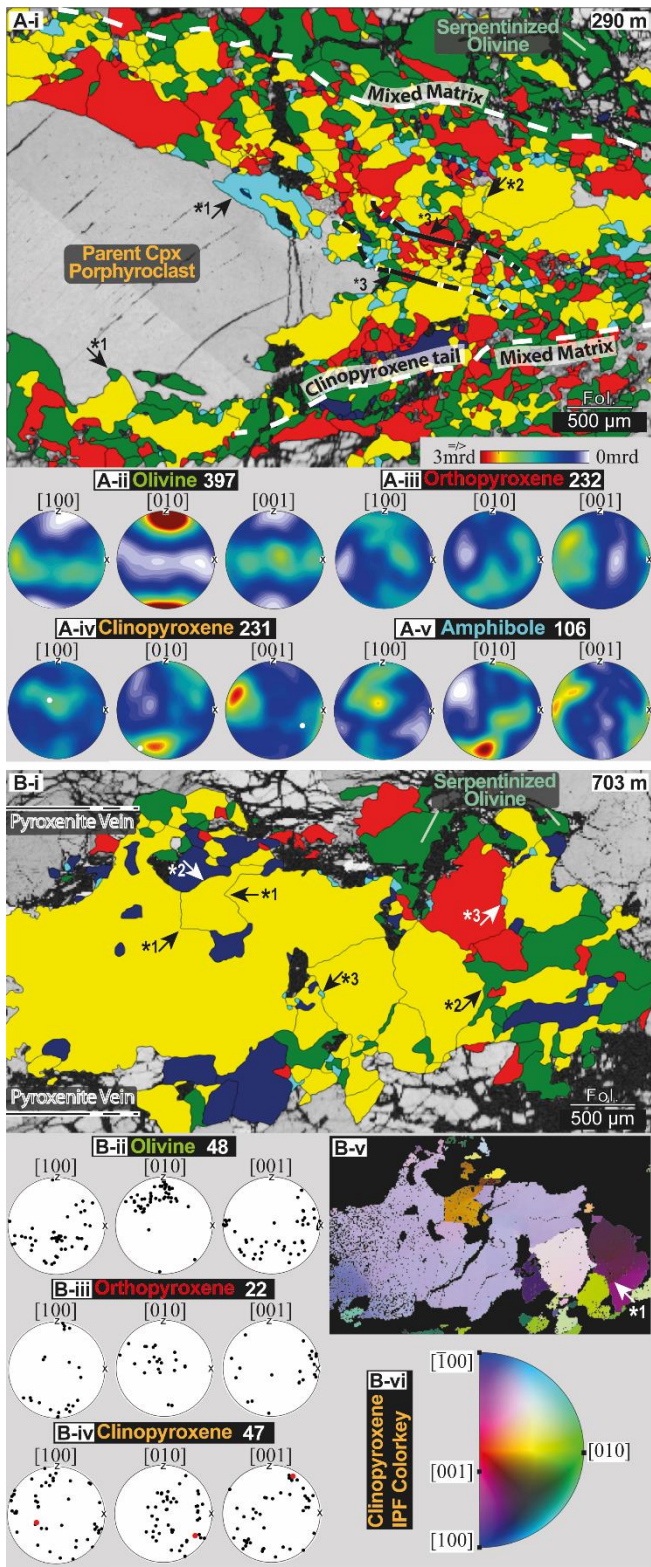
Fig. 8Fig. 9. Example microstructures of clinopyroxene porphyroclast with neoblast tail in 290 m (A-i) and cpx-dominated pyroxenite layer at 703 m (B-i) distance to the SZBNW-B. A: Clinopyroxene porphyroclast neoblast tail embedded in the mixed matrix with amphibole/ol indentations (*1) and interstitial amph (*2). Within the tail a band of fine grained neoblasts (*3) is present. CPOs of all phases are given in A ii-v. B: Pyroxenite layer with straight grain (*1) and lobate/irregular phase boundaries (*2) and interstitial amph and spl (*3). Pole figures of ol (B-ii), opx (B-iii) and cpx (B-iv) orientations are given. The cpx orientation map (B-v; colour key in B-vi) shows grain-internal deformation and subgrain boundaries (*1).

In the tectonite, isolated clasts of clinopyroxene are less frequent than those of orthopyroxene (Fig. 3Fig. 2F). Here, beside the small, interstitial cpx grains mentioned in the mixed matrix section, coarser clinopyroxene grains are predominantly present in pyroxenite layers consisting of intergrown pyroxenes, spinel and olivine (Fig. 8Fig. 9B-i). Phase boundaries in these are irregular, whereas grain boundaries tend to be straight and angular (Fig. 8Fig. 9B-I *1). A differentiation between parent clast and neoblasts is not possible. In mylonitic samples, clinopyroxene porphyroclasts, either present isolated (Fig. 3Fig. 2B-ii) or in deformed assemblages of the above-described layers (Fig. 3Fig. 2D-ii), form tails of neoblasts, which are sweeping into the foliation. Compared to opx neoblast tails, those of clinopyroxene porphyroclasts are more pronounced both in frequency and in tail length (Fig. 3Fig. 2). Additionally, contrary to opx neoblast tails, which formation/frequency seems to depend on the proximity to the SZBNW-B, neoblast tails of cpx porphyroclast are also present in distal mylonitic samples (Fig. 3Fig. 2E-ii). Neoblast tails of cpx porphyroclasts consist of 48 % clinopyroxene (range 22-88), 27 % olivine (range 7-56), 19 % orthopyroxene (range 4-40), 3 % amphibole (range 0-9) and 2 % spinel (range 1-10). For the major components (cpx, opx, ol) no change in phase abundances is present over the transect (Fig. 4Fig. 3F). For the minor phases of amphibole and spinel it seems that in distal parts of the mylonites and in tectonites spinel is the prevailing secondary phase, whereas closer to the SZBNW-B amphibole is more abundant (Fig. 4Fig. 3F). In most microstructures, spinel and amphibole occur separated from each other. Average grain sizes are 88 µm for cpx (range 53-177), 57 83 µm for reconstructed olivine (range 2957-115137), 70 µm for opx (range 40-116), 38 µm for amphibole (range 20-63) and 44 µm for spinel (range 23-112). The distribution of grain sizes is divided into coarse areas of primary phases (pyroxenes and olivine) and fine-grained areas of thoroughly mixed secondary (amphibole or spinel) and primary phases (Fig. 8Fig. 9A-I *3). Primary phase grain sizes are relatively constant over the first 300 m distance to the SZBNW-B (Fig. 4Fig. 3C). In the distal mylonitic part and in the tectonic regime, their grain size increases. Amphibole and spinel average grain sizes are about half of the size of primary phases (Fig. 4Fig. 3C). Their grain sizes tend to be constant over the entire transect. For both, primary and secondary phases, a slight excursion towards bigger grain sizes around ~280 m distance to the SZBNW-B is present. Average aspect ratios are with 1.8 for cpx, 2 1.09 for olivine, 1.9 for opx, 1.9 for amphibole and 1.9 in general lower than in matrix domains (S2). In contrast to the grain size, aspect ratios are more constant over the entire transect (S2). Phase boundaries form on average 72 % (±10 %) of the total boundary length (Fig. 3Fig. 2I). This distribution is in general constant over the entire transect, independent of mylonitic or tectonic unit. Amphibole is mostly affiliated to clinopyroxene (S2).

Olivine neoblasts CPOs in tails of clinopyroxene porphyroclasts are variable. Beside the most present A- and B-type (each n=4) transitions to the AG- type with point maxima in [100] and [010] girdles, pure AG-types and one clear E-type are present (Fig. 4S3). Their strength is moderate to strong (av. max mrd 12, av. M index M=0.15). Clinopyroxene neoblast

CPOs are weak (av. max mrd 15, av. ~~M index~~M=-0.0~~7~~9). In most cases, the parent clinopyroxene porphyroclasts have an imprint on the neoblast orientation (e.g., ~~Fig. 8~~Fig. 9A-iv). However, compared to orthopyroxene, clinopyroxene maxima are often less pronounced and blurred and therefore more variable from their parent clast orientation. The [001] axes are largely parallel to the lineation. Occasionally (n=2), [100] maxima are oriented parallel to the lineation. If present, orthopyroxene neoblasts are parallel to clinopyroxenes with their [001] and show occasionally 90° rotations for [100] and [010]. Amphibole neoblasts are mostly oriented parallel to the pyroxenes (e.g., ~~Fig. 8~~Fig. 9A-v).

4.1.3 Clinopyroxene-amphibole veins
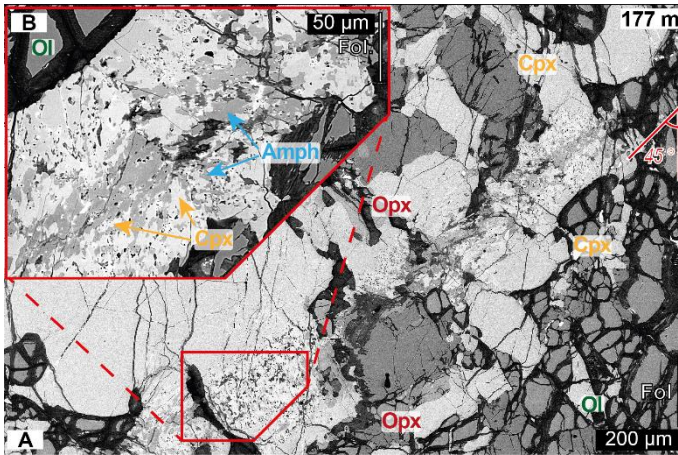
~~Fig. 9~~Fig. 10. A: Clinopyroxene amphibole vein crosscutting the mixed matrix and a clinopyroxene porphyroclast. Note the ~45° angle between foliation and vein orientation. B: Close-up view of vein showing zoning in cpx-rich rim and amph-rich ~~center~~centre.

In three samples, veins consisting of fine grained (ECD < 10 µm) cpx and amphibole were analyzed. These veins crosscut porphyroclasts, tails and the mixed matrix with an orientation of ~45° to the foliation (~~Fig. 9~~Fig. 10). In olivine-rich domains no such veins were found. The veins are best visible when crosscutting cpx porphyroclasts or pyroxenite layers (~~Fig. 9~~Fig. 10). Crosscutting previous structures oblique to the foliation, these veins are attributed to the late evolution of the Ronda peridotite. Because of the focus of this research on the mylonite formation a detailed microstructural investigation was omitted. However, a short revision is given in the geochemistry and discussion chapters.

4.2 Mineral chemistry

The major-element composition of both pyroxenes (opx and cpx), olivine, amphibole and spinel were determined from three samples with different distances to the ~~SZB~~NW-B (96 m, 177 m, 290 m). Apart from the olivine-rich matrix, all microstructural domains (cpx/opx neoblast tails, mixed matrix) were analyzed for each sample, if present. Neoblast tail measurements include the analysis of the parent pyroxene porphyroclast. There is a general trend for all analyzed phases of decreasing Mg# with increasing distance to the ~~SZB~~NW-B (Figs. 1~~0~~1,1~~1~~2). Coupled to the decrease in Mg# are in most cases an increase in TiO_2 and a decrease in Cr_2O_3 (Figs. 11~~0~~,12~~1~~). In the following, deviations from this trend and phase

specific geochemical variations are presented. Detection limits (S1), the complete microprobe data (S34) and additional

540   graphs (S45) are attached as supplementary data.

4.2.1 Orthopyroxene

All analyzed orthopyroxenes have with Mg#s (molar Mg/(Mg+Fe)) exceeding 0.89 enstatitic compositions (Fig. 10Fig. 11). In general, neoblasts of tails and in the mixed matrix have lower Cr₂O₃, Al₂O₃ and TiO₂ abundances than opx porphyroclasts of the same sample (Fig. 10Fig. 11). The decrease in Mg# with increasing distance to the SZBNW-B is most prominent in opx porphyroclasts but also present for all neoblasts. The complete range of this trend is from Mg# 0.89 at 290 m distance to Mg# 0.91 at 90 m distance to the SZBNW-B. The Mg# decrease (increase in FeO) is coupled with an increase of TiO₂ and a slight decrease of Cr₂O₃ (Fig. 10Fig. 11C/E).

4.2.2 Clinopyroxene

All analyzed clinopyroxenes have a diopsitic composition. For each analyzed sample, clinopyroxene porphyroclasts have in general lower Mg#s and higher Al₂O₃ abundances than associated neoblasts. For Na₂O, CaO, Cr₂O₃ and TiO₂, systematic differences between neoblasts and porphyroclasts of a given sample are not present (Figs. 4, 110, S4). However, the neoblasts have a bigger scatter in their composition of these oxides. For clinopyroxene, the decrease in Mg# is with a range from Mg# 0.89 (290 m) to Mg# 0.93 (90 m distance to the SZBNW-B) more pronounced than for orthopyroxene (Fig. 10Fig. 11). Like orthopyroxene, the decrease in Mg# is coupled to a decrease in Cr₂O₃ and an increase in TiO₂ (Fig. 10Fig. 11D/F). Additionally, Na₂O increases and CaO decreases with decreasing Mg# and increasing distance to the SZBNW-B. Clinopyroxene neoblasts from a crosscutting amphibole-pyroxenitic vein deviate significantly from all other analysis by markedly lower Al₂O₃ and Na₂O abundances and increased CaO (Figs. 110, -S35).

4.2.3 Olivine

All analyzed olivines have a forsteritic composition. Olivine neoblasts follow the trend of decreasing Mg# with increasing distance to the SZBNW-B independent from the microstructural domain (Fig. 11Fig. 12A). However, at 290 m distance to the SZBNW-B one group of olivine mixed matrix neoblasts tends to higher Mg#s (Fig. 11Fig. 12A). Yet, with lower Mg#s only present in distal samples, the decrease of the Mg# seems to strictly depend on the distance to the SZBNW-B. CaO and NiO abundances do not vary (Fig. 11Fig. 12D). Most of the Cr₂O₃ and all TiO₂ measurements lie beneath the detection limit and are therefore excluded from further analysis (S45).

4.2.4 Amphibole

All amphiboles are Ti/Cr-rich pargasites with in general variable abundances of K₂O (range 0-0.78 wt.%), Cr₂O₃ (range 0.19-1.7 wt.%) and TiO₂ (range 0.66-3.76 wt.%) (Figs. 121, S35). Apart from one measurement carried out on a sample

situated at 90 m distance to the ~~SZB~~NW-B, all amphiboles follow the trend of decreasing Mg# with increasing distance to the ~~SZB~~NW-B (~~Fig. 11~~Fig. 12B). Like both pyroxenes, Cr_2O_3 abundances decrease and TiO_2 abundances increase with increasing Mg# (~~Fig. 11~~Fig. 12E/G). For TiO_2, four measurements show deviations from this trend by lower abundances. There are no systematic differences between amphiboles associated to ortho-, clinopyroxene tails or the mixed matrix. Na_2O and CaO abundances are except for four/three measurements constant for all samples and all microstructural domains (S~~5~~).

4.2.5 Spinel

Most spinels follow the trend of decreasing Mg# and increasing TiO_2 with increasing distance to the ~~SZB~~NW-B (~~Fig. 11~~Fig. 12C). However, coarse grained spinels (ECD ~1 mm) associated with pyroxenes in kelyphitic intergrow at 290 m distance to the ~~SZB~~NW-B show Mg#s shifted to higher values (~~Fig. 11~~Fig. 12C). Additionally, spinels associated to cpx neoblast tails have in each sample the highest Mg# (~~Fig. 11~~Fig. 12C). High Mg#s in these spinels are related to low TiO_2 and Cr_2O_3 values (~~Fig. 11~~Fig. 12F/H). In contrast to amphibole and both pyroxenes, Cr_2O_3 abundances increase with increasing distance to the ~~SZB~~NW-B (~~Fig. 11~~Fig. 12H).
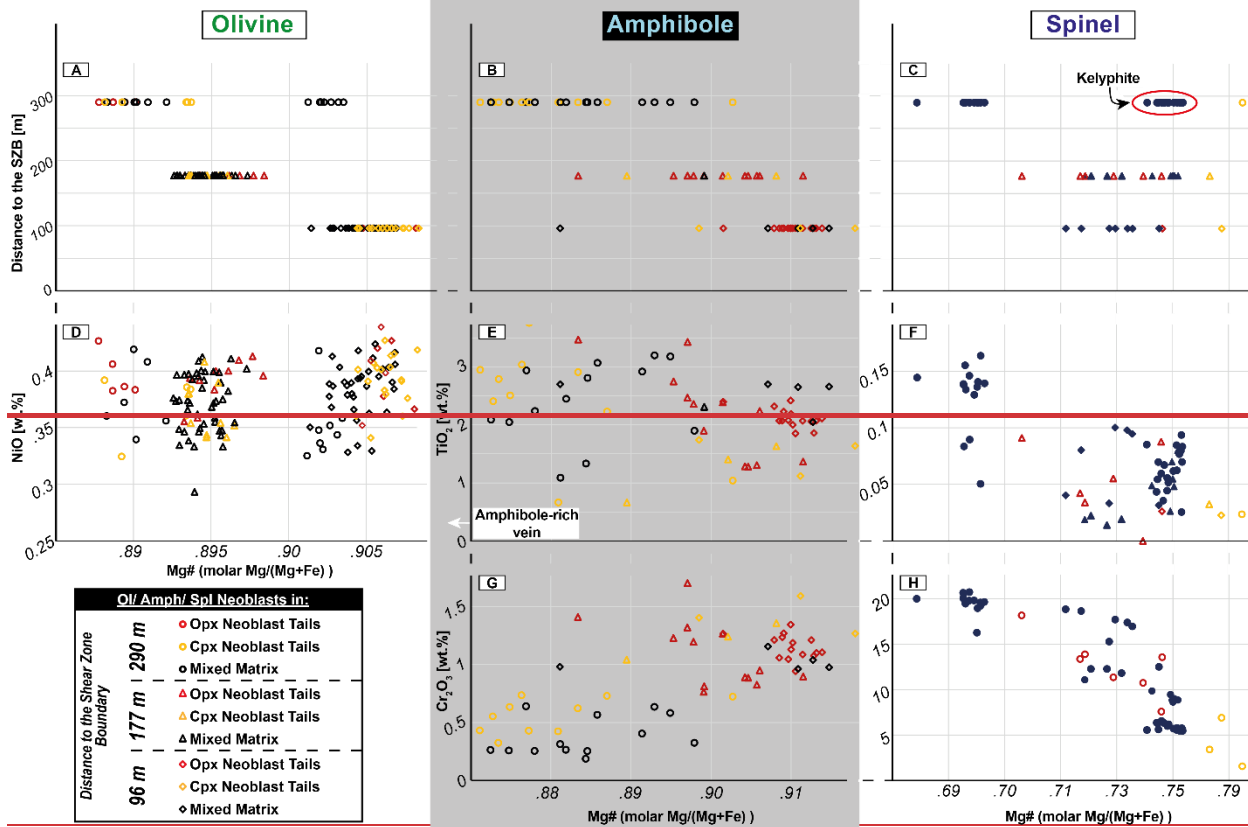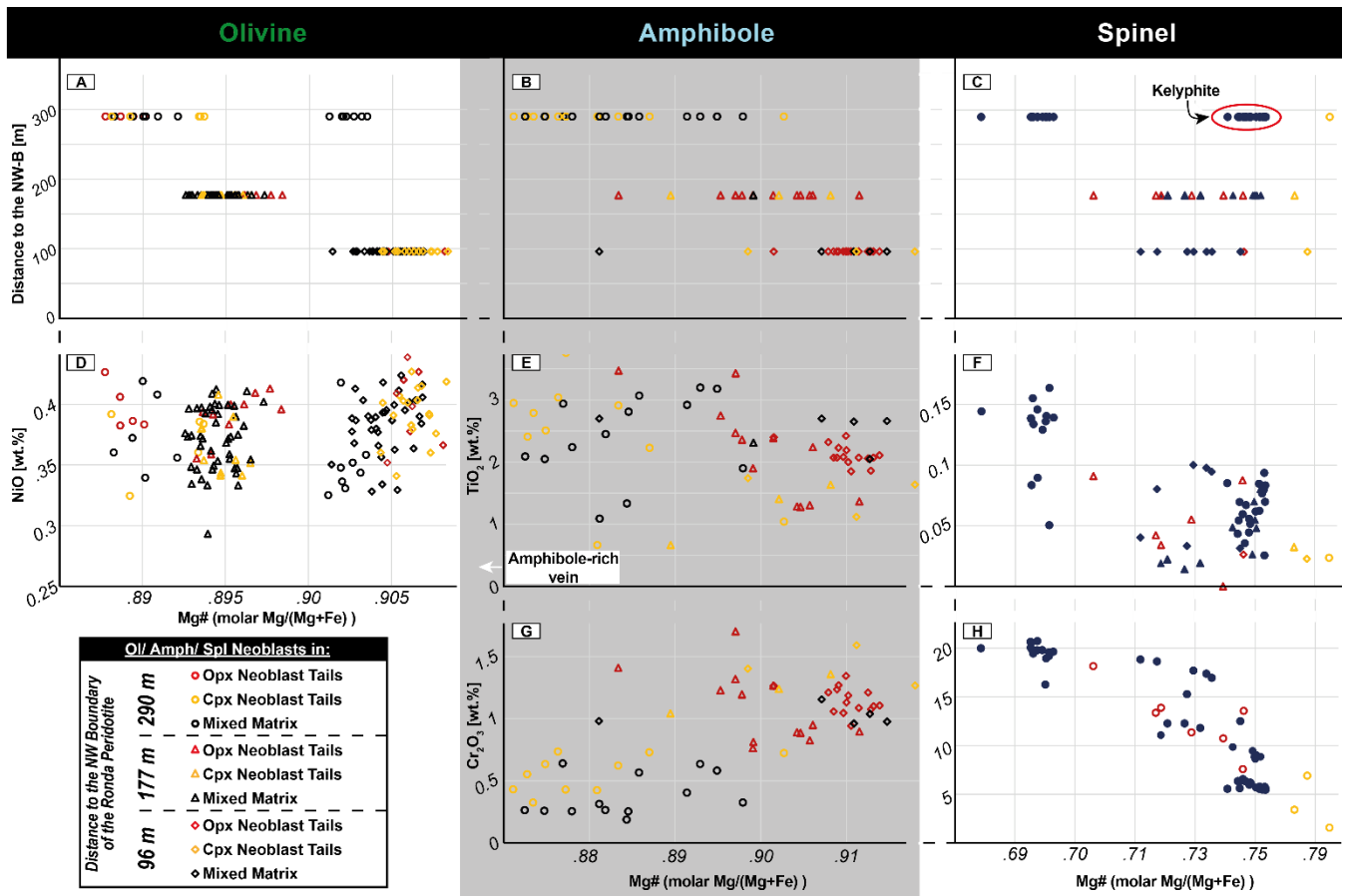
Fig. 11Fig. 12. EPMA data plots of olivine, amphibole and spinel neoblasts of cpx/opx porphyroclast tails and the mixed matrix at 96 m, 177 m and 290 m distance to the ~~SZB~~NW-B. A/B/C: Mg# in dependence of the distance to the ~~SZB~~NW-B. D: Mg# against NiO wt.% for olivine neoblasts. E/F: Mg# against TiO_2 for amph and spl neoblasts. G/H: Mg# against Cr_2O_3 for amph and spl neoblasts.

5 Discussion

5.1 ~~Microstructural implications for the shear zone evolution~~ Microstructural implications – Formation

5.1.1 Mixed Matrix

As the dominant microstructure of all analyzed samples, from 29 to 700 m distance to the NW-B, the mixed matrix is of particular importance for understanding the formation and evolution of the shear zone. Its constant microstructural parameters are primarily a persistent phase assemblage of interstitial secondary grains (opx, spl ± cpx) distributed in between coarse pyroxenes and olivine. The dispersed distribution of secondary phases results in consistent high mixing intensities (av. 71 % phase boundary: Fig. 3G). Additionally, phase boundaries are persistently lobate, and grain shapes, especially of coarse pyroxenes, are highly irregular. Highly lobate phase boundaries, irregular grain shapes, intense, homogeneous phase

mixing and dispersed interstitial secondary grains indicate a formation of these microstructural features by reactions (e.g. (Dijkstra et al., 2002; Hidas et al., 2016; Newman et al., 1999; Tholen et al., 2022). Potential driving forces of reactions in the upper mantle are metamorphism and/or metasomatism by melt- or fluid-rock interactions.

Metamorphic reactions in upper mantle shear zones were coupled to the garnet peridotite–spinel peridotite, and at shallower depth, spinel peridotite–plagioclase peridotite transitions and triggered continuous net transfer reactions (Furusho & Kanagawa, 1999; Newman et al., 1999; Tholen et al., 2022). As phase mixing in the Ronda shear zone is not bound to a specific phase association (grt/spl-bearing), and no plagioclase is present, metamorphic reactions are unlikely to act as dominant driving force for the neoblast formation in the matrix and in pyroxene tails.

As formerly elaborated by Hidas et al. (2016) in their study on ultramylonitic shear zones in Ronda's SSE plagioclase peridotites (location in Fig. 1), syn-kinematic net-transfer, dissolution-precipitation reactions and neoblast crystallization can also be catalyzed by fluids. In this regard, syn-kinematic amphibole precipitation and fluid channelling were also postulated forming mixed phase assemblages and ultramylonites in the center of deformation of the Lanzo shear zone (Vieira Duarte et al., 2020). For a peridotitic composition at shallower upper mantle PT-conditions, Hidas et al. (2016) assume the formation of 1.0–1.4 wt% amphibole when fluid saturation is attained. However, despite all reported microstructural similarities (high mixing intensity, irregular phase boundaries, interstitial or film-like shapes of orthopyroxenes), there are distinct differences between the NW Ronda shear zone and those mentioned above. Firstly, in contrast to the well dispersed amphibole in the matrix reported by Hidas et al. (2016) (~1.6%) and Vieira Duarte et al. (2020) (≤ 30 vol%), in NW Ronda amphibole is mostly limited to pyroxene neoblast tails (av. 3%). In the mixed matrix, amphibole only contributes to on average 1%, which is again mostly associated with coarser pyroxenes, especially cpx. The second difference is the lack of amphibole-bearing ultramylonites and no localization of deformation coinciding with amphibole-rich assemblages (see section 5.3).

Microstructural features as interstitial grains with low dihedral angles, neoblast indentations in coarse orthopyroxene and highly irregular phase were furthermore considered as evidence for melt-rock reactions and secondary crystallization from percolating melts (Dijkstra et al., 2002; Stuart et al., 2018; Suhr, 1993). In this regard, the commonly found irregular, highly lobate boundaries between olivine and orthopyroxene suggest a reaction already evoked by Dijkstra et al. (2002) for melt assisted shearing in the Othris peridotite:

Orthopyroxene + low-Si melt ↔ Olivine + high-Si melt (← high stress, → low stress)

(Reaction I, Dijkstra et al. (2002))

Even though these features suggest a genesis by percolating melt, its composition remains open. Melt percolation were reported to form lherzolite, plagioclase-bearing peridotite and grt-peridotite replacing harzburgite and dunite in a process called "refertilization" (Beyer et al., 2006; Hu et al., 2020; Müntener & Piccardo, 2003; Le Roux et al., 2007). This process was also ascribed to form cpx-enriched tectonites in the refertilization front a few hundred meters ahead of the melting front between Ronda's coarse grained peridotites and the tectonite unit (Lenoir et al., 2001). The melts origin is ascribed to partial melting (2.5-6.5 % extraction) of the coarse grained peridotites at conditions close to the anhydrous peridotite solidus (T ≥

635 1200°C) at 1.5 GPa (Lenoir et al., 2001). In their model, melting was triggered by a rapid, transient heating event (Lenoir et al., 2001). Going further, Soustelle et al. (2009) postulated, that Si-rich melts fertilized the spl-tectonites of the NW Ronda shear zone up to 1.5 km ahead of the melting front. According to these authors, early melt pulses lead to pyroxene and spinel crystallization as irregularly shaped grains, whereas late stage, second-order percolation of evolved melt caused the crystallization of interstitial, undeformed pyroxenes and spinel with a strongly enriched LREE chemistry. In contrast to the

640 data of Soustelle et al. (2009) which leaves the mylonitic shear zone melt-unaffected, our data traces microstructural evidence of melt percolation up to the NW boundary of the Ronda massif. However, a change in the modal composition of refertilized lherzolites by neocrystallized pyroxenes, as commonly described (e.g., Le Roux et al., 2007), is not present, either in their nor in our data. Additionally, syn-kinematic conditions of 800–900 °C and 1.95–2.00 GPa postulated by Garrido et al. (2011) for the mylonite unit refuted the presence of a heating event prior to shearing and inflict with the syn-

645 kinematic presence of refertilizing, basaltic melt.

On the southern limb of the Gibraltar arc in the Moroccan counterpart of the Ronda massif, the Beni Bousera peridotite (Fig. 1), Frets et al. (2014) reported beside an analogous structure of the massif itself, very similar microstructural evidence (irregular grain shape, lobate boundaries, high mixing intensity) for syn-kinematic reactive melt percolation and melt-rock reactions in the corresponding unit of the investigated grt/spl-mylonites. Syn-kinematic conditions of 850-950° C and ~2.0

650 GPa, matching those obtained in Ronda, led to the assumption of a metasomatism by small fractions of fluids or evolved melts which did not reset the equilibrium temperatures (Frets et al., 2012, 2014). Amphibole presence in pyroxene neoblast tails (see section 5.1.2), ubiquitous evidence of reaction-derived microstructures and pyroxene crystallization and syn-kinematic PT-conditions of 800–900 °C and 1.95–2.00 GPa indicate a similar OH-bearing metasomatism by highly evolved melts in Ronda's tectonite and mylonite unit.

655 Geochemically, all microstructural domains are mainly characterized by an increase in FeO (= decrease in Mg#) and TiO_2 for olivine, pyroxenes, spinel and amphibole towards the melting front, with increasing distance to the NW-B respectively (Fig. 13). The continuous geochemical trends and the presence of interstitial spinel and pyroxene neoblast between olivine crystals in the mixed matrix of both, mylonitic and tectonic samples, suggest that the metasomatic reactions leading to pyroxene crystallization were present in the entire transect. In Fig. 13, data from Soustelle et al. (2009) was put in correlation

660 to the distance to the NW-B and added to the data presented here. Both data follow the geochemical trend of increasing Mg# with decreasing distance to the NW-B (arrows Fig. 13). However, an offset is present between both data sets with the data of Soustelle et al. (2009) staring to decrease from higher Mg# (~0.92) than the samples described here (~0.89) (Fig. 13). To resolve the course of the trends in detail requires additional detailed geochemical analysis of the transition zone of spl/grt-mylonites and spl-tectonites which was not in the focus of this research but might give further insights into the timing of the

665 metasomatic event(s).
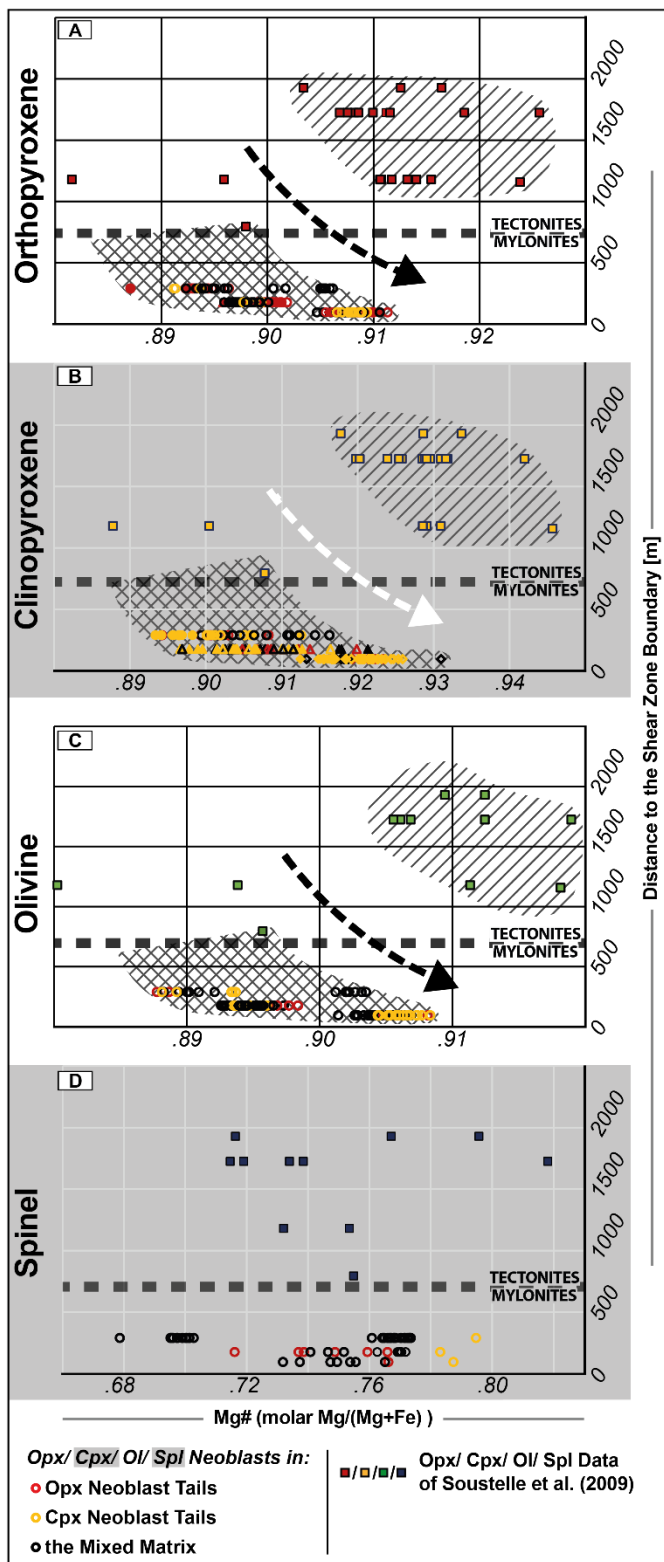
Fig. 13. Mg# data of spinel tectonites (Soustelle et al., 2009) and of spl/grt mylonites (this study) vs. distance to the NW-B. Hatched area: geochemical signature of melt in tectonites; Crosshatched area: geochemical signature of melt in mylonites. Mg# of opx (A), cpx (B), olivine (C) and spl (D) plotted against the distance to the NW-B. Location of the studied area by Soustelle et al. (2009) is indicated in Fig. 1. Arrows indicate geochemical trend of increasing Mg# towards the NW-B.

5.1.2 Pyroxenites and pyroxene porphyroclast neoblast tails

Due to their microstructural and geochemical similarities, both pyroxene porphyroclast (opx/ cpx) microstructural domains will be discussed together. In their neoblast tails, the phase assemblage (cpx, opx, ol, spl, amph) with high phase boundary percentages (opx av. 77%, cpx av. 72%) and highly irregular boundaries of porphyroclast and neoblasts remain constant throughout the entire transect (Figs. 3, 8, 9). Especially in the tectonite, clinopyroxene porphyroclasts are often associated with pyroxenitic layers, which show a coarse-grained intergrowth of both pyroxenes, olivine and spinel. Beside their formation by partial crystallization from percolating melts, Garrido and Bodinier (1999) interpreted these websteritic layers as formed at the expense of garnet-bearing pyroxenites by melt-rock reactions. The kelyphitic structures in pyroxenite layers of mylonites, also described by Van Der Wal and Vissers (1996), corroborate that these assemblages represent at least partially garnet breakdown products. However, the replacement of garnet-bearing by websteritic assemblages, which is documented in our samples up to the tectonite-mylonite transition, was so far associated with the melting/recrystallization front (Garrido and Bodinier, 1999). In the tectonite regime, straight grain boundaries with 90° angles within the pyroxenites suggest that these websteritic assemblages were partly annealed after having replaced garnet-bearing assemblages.

Already in the distal part of the mylonite zone, the pyroxenite layers are affected by pinch-and-swell structures, which result from boudinage (Précigout et al., 2013). In the same samples, the formation of neoblast tails of cpx porphyroclasts and fine-grained patches of neoblasts bordering irregular, lobate boundaries of opx porphyroclasts with indentations of all neoblast phases indicate metasomatic reactions. Amphibole indentations into the porphyroclasts underline that it is part of the primary neoblast assemblage. Pargasitic amphibole has been shown to be stable up to ~3.8 GPa at 1000 °C with its stability strongly depending on the amount of bulk H_2O (Mandler and Grove, 2016). Accordingly, pargasite-bearing peridotites have been shown to be stable in peridotite shear zones at similar, syn-kinematic PT-conditions to those present in Ronda (Garrido et al., 2011; Johanesen et al., 2014: 1.95-2/ 1.5 GPa, 800-900 °C; (Hidas et al., 2016; Tholen et al., 2022). The common association of pyroxenes, olivine and amphibole, indentations of amphibole into pyroxene porphyroclasts also reported by Van der Wal (1993) and the observation that spinel is less abundant in areas with amphibole and vice versa suggests a reaction of pyroxenes, spinel and amphibole. The replacement of clinopyroxene and spinel by amphibole in peridotites is commonly referred to metasomatic reactions (e.g., Blatter and Carmichael, 1998; Bonadiman et al., 2014; Ishimaru et al., 2007). Hydrous melts were observed forming amphibole at the expense of primary orthopyroxene, olivine and clinopyroxene (Rapp et al., 1999; Sen and Dunn, 1995). In their study of xenoliths from Antarctica Coltorti et al. (2004) suggested a melt-assisted reaction with formation of amphibole at the expense of clinopyroxene and spinel shortly (few thousand years) before their uplift. Their model implies a two-stage melt-rock evolution with an initial crystallization of pyroxenes, olivine and spinel succeeded by the secondary crystallization of amphibole. However, the composition of associated glass suggests that the

metasomizing agent was a Na-alkali silicate melt. For Ronda, constant Na_2O abundances for clinopyroxene clasts and neoblasts and Ti/Fe enrichment for pyroxenes suggest a Fe-Ti-enriched, OH-bearing melt. As no chemical difference is present between neoblast tail and matrix microstructures, pyroxene tail assemblages are thought to be affected/formed by this metasomatism like the mixed matrix (Figs. 11, 12). Therefore, the formation of the neoblast tails is attributed to the same deformation stage as the mixed matrix. According to the experimental results of Wang et al. (2021), the composition of the crystallizing amphibole varies greatly depending on the tectonic setting, metasomatic melt and peridotite composition. In this regard, relatively low Mg# and high Na_2O and TiO_2 abundances of the analyzed amphibole indicate a supra-subduction zone metasomatism (Coltorti et al., 2007). Higher OH abundances in pyroxene neoblast tails are corroborated by olivine B-type CPOs, which indicate increased concentrations of H/Si (Jung et al., 2006; Jung and Karato, 2001; Mizukami et al., 2004).

Towards the NW-B the proportion of intact pyroxene porphyroclasts to reacting porphyroclasts decreases. Concomitant with that, the dominant olivine CPO changes from an A-type CPO, indicative for low water and intermediate stress conditions, to an AG-type or occasionally a B-type CPO, indicative for increased water content and high stress (e.g., Jung, 2017). The increased presence of olivine B-type CPOs towards the NW-B was formerly interpreted to result from grain boundary sliding (GBS) rather from a change in the dominant slip system (Précigout and Hirth, 2014). However, over the entire mylonitic area, independent on the distance to the NW-B, olivine CPOs from pyroxene neoblast tails are predominantly B- or-AG type (Fig. 4). Pyroxene tail microstructures, which include, due to the scanning arrangement, areas of or transitions to the surrounding matrix, tend to have AG- or A-type olivine CPOs. On the opposite, a stronger B-type is commonly bound to a well-defined neoblast tail without large amounts of the surrounding matrix highlighting the relation between CPO-type and microstructural location. Accordingly, the girdle distributions of olivine's [100] and [001] within the foliation plane present in the AG-type could result from a mix of A- and B-type CPOs. The increased occurrence of amphibole in neoblast tails, especially in association with cpx, indicates higher OH abundances. This in turn corroborates the association of B-type CPO to increased concentrations of H/Si (Jung et al., 2006; Jung and Karato, 2001; Mizukami et al., 2004). The correlation of a stronger B-type with increased clinopyroxene abundances observed by Précigout and Hirth (2014), which was at odds with the B-type solely dependent on the increase of GBS towards the NW-B therefore fits with both presented observations: Pronounced presence of amphibole and olivine B-type CPOs in pyroxene neoblast tails and the preferred association of amphibole with clinopyroxene. Accordingly, the decrease of porphyroclasts and the increase in pyroxene neoblast tails towards the NW-B leads to an increase of olivine neoblasts with B-type orientation. However, the formation of olivine B-type CPOs by GBS in the mixed matrix close to the NW-B (< 100 m), suggested by Précigout and Hirth (2014), cannot be ruled out. Although multiphase mixtures crystallized in the metasomatic neoblast tails of pyroxenes, no strain localization as reported for pyroxene reaction tails in other peridotite shear zones occurred in these microstructural domains (Hidas et al., 2013b; Tholen et al., 2022). The main reason for the lack of strain localization might be that all microstructural domains have similar amounts of phase boundaries and similar grain sizes. Therefore, no strain partitioning between the mixed matrix and the tails associated with a switch to a grain size sensitive deformation mechanism was achieved (e.g., Rutter and Brodie, 1988). The strong relation between neoblast and parent porphyroclast orientation implies an inherited orientation of the

parent phase neoblasts. The shared orientation of at least one preferred orientation for amphibole and second pyroxene neoblasts with parent phase clast and neoblasts suggests topo- or epitactic growth (Putnis et al., 2006). Beside the formation of neoblasts, elongated, mostly "retort shaped" (Johanesen and Platt, 2015) and/or stable opx porphyroclasts present up to the NW-B suggest that deformation of opx was accommodated more strongly by intragranular deformation than for cpx porphyroclasts.

5.~~21.1~~ ~~Mixed matrix~~ Microstructural implications – Deformation

Main differences between the mylonitic and the tectonic mixed matrix are the grain shape and, subordinate, the grain size. The tectonitic mixed matrix is characterized by small, equiaxial, interstitial grains of both pyroxenes and spinel between coarse pyroxenes and olivine. Neoblast formation in both the tectonic mixed matrix and around orthopyroxene porphyroclasts at the tectonite-mylonite transition, show weak dependence on the foliation. Additionally, tectonic mixed matrix orthopyroxene neoblasts have a CPO with [001] subperpendicular to the foliation, which is atypical for a deformation-imposed CPO (e.g., Jung, 2017) and in most cases strongly connected to the parent clast CPO. Distributed neoblast precipitation, equiaxial neoblast grain shapes and irregular CPO indicate weaker deformation in tectonites and distal (large distance to NW-B) mylonites. Olivine, on the other hand, with the strongest CPOs of all microstructural domains (A-type CPO, M= 0.2) and lobate grain boundaries was affected by dislocation creep.

In the mylonite unit, neoblasts and pyroxene porphyroclasts show similar irregular grain boundaries but a different shape and size of neoblasts compared to the tectonites. There is a clear preferred orientation of film-like pyroxenes along grain boundaries subparallel to the foliation, which was also observed in peridotite mylonites from the Othris shear zone (Dijkstra et al., 2002) and in ultramylonites from the plagioclase-tectonite unit in Ronda (Hidas et al., 2016). For Othris it was assumed that the direction of the above reaction I depends on local stress variations (Dijkstra et al., 2002). Orthopyroxenes with highly irregular ol-opx phase boundaries sub-perpendicular to the foliation, and ol indentations, which are present in the mixed matrix and dominant in stress shadows of pyroxene tails represent the "low stress", ol forming variant of reaction I. On the other hand, and as pervasively present in Ronda's mylonitic mixed matrix, the wedge-shaped pyroxene neoblasts along ol-ol boundaries subparallel to the foliation were interpreted as "high stress" pyroxene precipitates of reaction I. For fluid assisted dissolution-precipitation reactions in ultramylonites, Hidas et al. (2016) inferred that the fluid composition can be locally controlled by the surrounding minerals, allowing alternating dissolution and precipitation of olivine and orthopyroxene. Regardless of the type of metasomatic agent, the microstructures, in particular the highly lobate phase boundaries and the wedge/film-like shapes of pyroxenes along the foliation, strongly point to the activity of dissolution-precipitation processes in the mylonitic mixed matrix. For the Beni Bousera, (Frets et al., 2014) argued consistently for the syn- to late kinematic formation of similar structures in the ~~coresponding~~corresponding ~~g~~Grt/~~s~~Spl- mylonites under near-solidus conditions. The metasomatism in the mylonites is therefore thought to be pre- to early syn-kinematic. In this regard,

the tendency of mixed matrix pyroxene neoblasts to lower TiO_2 and Cr_2O_3 abundances could indicate a stronger effect of diffusion on the smaller grains (Cherniak & Liang, 2012). This process could additionally be enhanced by ongoing deformation as elongated grain shape and size of the mylonitic mixed matrix suggest. Strain localization in the shear zone during this metasomatic process might have been supported by- (1) melt/fluid-enhanced dissolution-precipitation creep along grain boundaries (Hirth & Kohlstedt, 1995) and the (2) delimiting effect of secondary crystallized pyroxenes on the grain growth by pinning (Linckens et al., 2011).

However, even with grain-size-sensitive dissolution-precipitation creep being active, the strong CPO of olivine and of both pyroxenes, the increased dislocation density in neoblasts of the mixed matrix and the elongation of all present grains suggest dislocation creep as the main deformation mechanism in the entire transect. The localization of dynamic crystallization processes in olivine neoblasts is corroborated by the highest average M-indices (0.14-0.20) of each microstructural domain, except for cpx in neoblast tails of opx porphyroclasts (M= 0.19), and highest neoblast dislocation densities by GND concentration. Its dominant A-type indicates slip on (010) in [100] (e.g., Karato et al. 2008). In orthopyroxene, slip on (100) or on (010) is dominant with both directed towards [001] (Ohuchi et al., 2011; Ross and Nielsen, 1978). The activity of a dislocation creep-accommodated, grain-size-sensitive deformation mechanism was formerly suggested by Johanesen and Platt (2015) and Précigout et al. (2007). In contrast to dislocation creep accommodated GBS (DisGBS, Hirth and Kohlstedt, 2003) suggested by Précigout et al. (2007) and Précigout and Hirth (2014), Johanesen and Platt (2015) ~~favored~~favoured dislocation creep with a grain size sensitivity given by grain boundary migration as dominant recovery mechanism (DRX creep, Platt and Behr, 2011). Because microstructural evidence for both mechanisms ~~are~~ is present (GBS: grain and phase boundary alignments; DRX creep: lobate grain boundaries) and DRX creep and DisGBS are dominant under approximately the same conditions of grain size and shear stress (Johanesen and Platt, 2015), neither mechanism can be excluded by this study.

The change in the overall microstructure in the shear zone, interpreted as a continuous decrease in grain size towards the NW-B by several authors (e.g., Obata, 1980; Précigout et al., 2007; Van Der Wal and Vissers, 1996) could be related to the change in grain shape and grain size of the mixed matrix between tectonites and mylonites. ~~On base of~~Based on optically traced grain boundaries Johanesen and Platt (2015) reported a rather constant grain size of recrystallized olivine (~130 µm) with regional variations in mylonites and tectonites. In our study, neoblast grain sizes of all phases and from all microstructural domains stay constant over the entire mylonitic shear zone. For the mylonites, the trend of decreasing total grain size with decreasing distance to the NW-B reported by previous studies could be explained in this regard by the increasing amount of neoblasts rather than by a systematica~~lly~~ change in their grain size. The average reconstructed olivine grain size of 103 µm for the mixed and 107 µm for the ol-rich matrix lies in the range of average recrystallized olivine grain size reported by Johanesen and Platt (2015) and ~~(~~Frets et al. ~~,~~ (2014) for the ~~g~~Grt/~~s~~Spl-mylonite unit of both, Ronda and Beni Bousera. The increase in grain size in the tectonite unit and its coarser, less deformed microstructures corroborate different deformation histories for mylonites and tectonites as described above (section 5.1.1). Differences in the shape of primarily the neoblasts of the mixed matrix are therefore thought to be dependent on the strain of the specific unit. To that effect, the

elongation of neoblasts in the mylonitic mixed matrix, the elongation of opx porphyroclasts and the elongation of pyroxene tails stretched ~~in~~ along the foliation are interpreted as increased strain towards the NW-B. Additionally, the increase in pyroxene porphyroclast neoblast tails with concurrent decrease of porphyroclasts towards the NW-B might indicate a strain

805 dependence. De Ronde and Stünitz (2007) reported a positive feedback between deformation and reactions in their experiments for the transition from plagioclase to spinel in olivine+plagioclase aggregates. An enhanced nucleation reaction rate was here explained by increasing deformation-induced defects in the reactant and the deformation-induced transportation of neoblasts away from the reaction interface, which thereby maintains a high chemical potential. For Ronda, this similar mechanism could clear the porphyroclast reaction interface of neoblasts and thereby form in the foliation

810 elongated neoblast tails. With constant stresses and constant dominant deformation mechanism(s) operating in the melt-affected area neoblast grain sizes are kept nearly constant. The increase in finite strain could be either due to an increase of the strain-rate (Johanesen and Platt, 2015) or a longer-lasting deformation in mylonites.

~~As the dominant microstructure of all analyzed samples, from 29 to 700 m distance to the SZB, the mixed matrix is of particular importance for understanding the formation and evolution of the shear zone. Beside grain shape and grain size,~~

815 ~~most microstructural parameters of the mixed matrix are constant over the entire transect (next paragraph, Fig. 4). Differences and constants suggest a uniform genesis but different deformation histories of mylonites and tectonites:~~ ~~Following the consistencies, several lines of microstructural evidence indicate a common formation process for the mixed matrix of tectonite and mylonites. The distribution between interstitial, secondary grains (pyroxenes, spinel) and coarser pyroxenes with highly lobate grain boundaries is alike in all mixed matrix domains. Accordingly, the presence of interstitial~~

820 ~~neoblasts with low dihedral angles and neoblasts along boundaries of coarse olivine is already present in the matrix of tectonites, which is in turn their dominant microstructure. Interstitial grains with low dihedral angles, embayments in coarse orthopyroxene and highly irregular grain boundaries of coarse pyroxenes and olivines are microstructural indications for secondary crystallization of melts and melt rock reactions (Dijkstra et al., 2002; Stuart et al., 2018; Suhr, 1993). Following Soustelle et al. (2009), interstitial pyroxenes are therefore thought to have crystallized from a Si-rich grain boundary melt.~~

825 ~~Constant phase assemblage and constant phase abundances in the mixed matrix of mylonites and tectonites suggests that both units were affected similarly by the melt. The commonly found irregular, highly lobate boundaries between olivine and orthopyroxene suggest a reaction already evoked by Dijkstra et al. (2002) for melt assisted shearing in the Othris peridotite:~~

~~Orthopyroxene + low-Si melt ↔ Olivine + high-Si melt~~

830 ~~(Reaction I, Dijkstra et al. (2002))~~

~~The direction of this reaction was shown to be dependent on local stress variations: Orthopyroxene decay was dominantly observed in stress shadows and thereby on boundaries at a high angle to the foliation. On the other hand, pyroxene precipitation mainly occurred along boundaries oriented subparallel to the foliation (Dijkstra et al., 2002).~~

835 Main differences between mylonitic and tectonic mixed matrix are the grain shapes and, subordinate, also the grain sizes. The tectonitic mixed matrix is characterized by small, equiaxial, interstitial grains of both pyroxenes and spinel between coarse pyroxenes and olivines. Neoblast formation in both the tectonic mixed matrix and around orthopyroxene porphyroclasts at the tectonite-mylonite transition, show weak dependence on the foliation. Additionally, tectonic mixed matrix orthopyroxene neoblasts have a CPO with [001] subperpendicular to the foliation, which is atypical for a

840 deformation imposed CPO. Distributed neoblast precipitation, equiaxial neoblast grain shapes and irregular CPO indicate weaker deformation in tectonites and distal mylonites. Olivine, on the other hand, with its strong A type CPO and lobate grain boundaries was affected by dislocation creep in form of dynamic recrystallization.

For the mylonitic unit, neoblast and pyroxene porphyroclasts show similar irregular grain boundaries but a different shape and size of neoblasts. There is a clear preferred orientation of film like pyroxenes along grain boundaries subparallel to the

845 foliation, which was also observed in peridotite mylonites from the Othris shear zone (Dijkstra et al., 2002). Following Dijkstra et al. (2002), these pyroxenes are interpreted as "high stress" precipitates of reaction I. Highly irregular phase boundaries between pyroxene and olivine sub perpendicular to the foliation in places present in the mixed matrix and dominant in tails of pyroxenes indicate pyroxene melt rock reactions as "low stress" variant of reaction I (Dijkstra et al., 2002). The strong CPO of olivine and of both pyroxenes suggest dislocation creep as the main deformation mechanism

850 (Johanesen and Platt, 2015; Précigout and Hirth, 2014). In olivine, the dominant A type indicates slip on (010) in [100] (e.g., Karato et al. 2008). In orthopyroxene, slip on (100) or on (010) is dominant with both directed towards [001] (Ohuchi et al., 2011; Ross and Nielsen, 1978). Towards the SZB the dominant olivine CPO changes from an A type CPO, indicative for low water and intermediate stress conditions, to an AG type or occasionally a B type CPO, indicative for increased water content and high stress (e.g., Jung, 2017). The increased presence of olivine B type CPOs towards the SZB was formerly

855 interpreted to result from grain boundary sliding (GBS) rather from a change in the dominant slip system (Précigout and Hirth, 2014). However, the CPO of pyroxene neoblast tails discussed in the next chapter does not support this assumption.

Deformation in the shear zone was probably enhanced by both the presence of melt during the early stages of shearing (e.g., Hirth and Kohlstedt, 1995) and the delimiting effect of secondary crystallized pyroxenes on the grain growth by pinning (e.g., Linckens et al., 2011). The resulting grain size reduction favours the activation of a grain size sensitive deformation

860 mechanism in the shear zone, which is documented by the piezometric data of Johanesen and Platt (2015) and Précigout et al. (2007). In contrast to GBS accommodated by dislocation creep (DisGBS, Hirth and Kohlstedt, 2003) suggested by Précigout et al. (2007) and Précigout and Hirth (2014), Johanesen and Platt (2015) favoured dislocation creep with a grain size sensitivity given by grain boundary migration as dominant recovery mechanism (DRX creep, Platt and Behr, 2011). Because microstructural evidence for both mechanisms are present (GBS: grain and phase boundary alignments; DRX creep:

865 lobate grain boundaries) and DRX creep and DisGBS are dominant under approximately the same conditions of grain size and shear stress (Johanesen and Platt, 2015), neither mechanism can be excluded by this study. However, the elongation of all present grains and the strong CPO for all phases demonstrates that the deformation was accommodated by dislocation creep in the entire mylonitic matrix. Even though the activity of GBS is supported by straight grain boundaries and smaller

grain sizes in the mylonites, phase mixing in the mixed matrix is a consequence of crystallization of interstitial pyroxenes rather than by extensive GBS as proposed by Précigout et al. (2007).

5.1.2 Pyroxenites and pyroxene porphyroclast neoblast tails

Due to their microstructural and geochemical similarities both pyroxenes (opx and cpx) will be discussed together. In the tectonite, clinopyroxene porphyroclasts are often associated with pyroxenitic layers, which show a coarse grained intergrowth of both pyroxenes, olivine and spinel. Garrido and Bodinier (1999) interpreted these websteritic layers as formed at the expense of garnet bearing pyroxenites by melt rock reactions. The kelyphitic structures in pyroxenite layers of mylonites, also described by Van Der Wal and Vissers (1996), corroborate that these assemblages represent at least partially breakdown products. However, the replacement of garnet bearing by websteritic assemblages, which is in our samples present up to the tectonite mylonite transition, was so far associated with the melting/recrystallization front (Garrido and Bodinier, 1999). In the tectonite regime, straight grain boundaries with 90° angles within the pyroxenites suggest that these websteritic assemblages were partly annealed after having replaced garnet bearing assemblages.

Already in the distal part of the mylonite zone, these pyroxenite layers are affected by pinch and swell structures, which result from boudinage. In the same samples, the formation of neoblast tails of cpx porphyroclasts and fine grained patches of neoblasts bordering irregular, lobate boundaries of opx porphyroclasts with indentations of all neoblast phases indicate reactions. Towards the SZB the proportion of intact pyroxene porphyroclasts to reacting porphyroclasts decreases. However, elongated, mostly "retort shaped" (Johanesen and Platt, 2015) and/or stable opx porphyroclasts suggest that deformation of opx was accommodated rather by intragranular deformation than by neoblast formation like for most cpx porphyroclasts. Nevertheless, the phase assemblage of neoblasts tails (cpx, opx, ol, spl, amph) remains constant for tails of both pyroxenes in all mylonitic samples pointing to a common reaction as neoblast formation process for both pyroxenes. Indentations of amphibole into pyroxene porphyroclasts underline that amphibole is part of the primary neoblast assemblage. Pargasitic amphibole has been shown to be stable up to ~3.8 GPa at 1000 °C with its stability strongly depending on the amount of bulk H_2O (Mandler and Grove, 2016). Accordingly, pargasite bearing peridotites have been shown to be stable in peridotite shear zones at similar, syn kinematic PT conditions to those present in Ronda (Garrido et al., 2011; Johanesen et al., 2014: 1.95 2/1.5 GPa, 800 900 °C; (Hidas et al., 2016; Tholen et al., 2022). The common association of pyroxenes, olivine and amphibole, indentations of amphibole into pyroxene porphyroclasts also reported by Van der Wal (1993) and the observation that spinel is less abundant in areas with amphibole and vice versa suggests a reaction of pyroxenes, spinel and amphibole. The replacement of clinopyroxene and spinel by amphibole in peridotites is commonly referred to metasomatic reactions (e.g., Blatter and Carmichael, 1998; Bonadiman et al., 2014; Ishimaru et al., 2007). Hydrous melts were observed forming amphibole at the expense of primary orthopyroxene, olivine and clinopyroxene (Rapp et al., 1999; Sen and Dunn, 1995). In their study of xenoliths from antarctica Coltorti et al. (2004) suggested a melt assisted reaction that crystallized amphibole at the expense of clinopyroxene and spinel shortly (few thousand years) before their uplift. Their model implies a two stage melt rock evolution with an initial crystallization of pyroxenes, olivine and spinel succeeded by the secondary crystallization of amphibole. However, the composition of associated glass suggests that the metasomatizing agent was a Na alkali silicate

melt. For Ronda, constant Na$_2$O abundances for clinopyroxene clasts and neoblasts and Ti/Fe enrichment for pyroxenes suggest a Fe Ti rich silicate melt. According to the experimental results of Wang et al. (2021), the composition of the crystallizing amphibole varies greatly depending on the tectonic setting, metasomatic melt and peridotite composition. According to Coltorti et al. (2007), relatively low Mg# and high Na$_2$O and TiO$_2$ abundances of the analyzed amphibole indicate in this regard a supra subduction zone metasomatism.

Over the entire mylonitic area, independent on the distance to the SZB, olivine CPOs from pyroxene neoblast tails are predominantly B or AG type. Pyroxene tail microstructures, which include, due to the scanning arrangement, areas of or transitions to the surrounding matrix, tend to have AG or A type olivine CPOs. On the opposite, a stronger B type is commonly bound to a well defined neoblast tail without large amounts of the surrounding matrix highlighting the relation between CPO type and microstructural location. Accordingly, the girdle distributions of olivine's [100] and [001] within the foliation plane present in the AG type could result from a mix of A and B type CPOs. Amphibole, which is concentrated in pyroxene neoblast tails and often associated with clinopyroxene, indicates higher OH abundances in these tails. This in turn corroborates the association of B type CPO to increased concentrations of H/Si (Jung et al., 2006; Jung and Karato, 2001; Mizukami et al., 2004). The correlation of a stronger B type with increased clinopyroxene abundances observed by Précigout and Hirth (2014), which was at odds with the B type solely dependent on the increase of GBS towards the SZB therefore fits with both presented observations: Pronounced presence of amphibole and olivine B type CPOs in pyroxene neoblast tails and the preferred association of amphibole with clinopyroxene. Accordingly, the decrease of porphyroclasts and the increase in pyroxene neoblast tails towards the SZB leads to an increase of olivine neoblasts with B type orientation. However, the formation of olivine B type CPOs by GBS in the mixed matrix close to the SZB (< 100 m) suggested by Précigout and Hirth (2014) cannot be ruled out. Although multiphase mixtures crystallized in the metasomatic neoblast tails of pyroxenes, no strain localization as reported for pyroxene reaction tails in other peridotite shear zones occurred in these microstructural domains (Hidas et al., 2013b; Tholen et al., 2022). The main reason for the lack of strain localization might be that all microstructural domains have similar amounts of phase boundaries and similar grain sizes. Therefore, no strain partitioning between the mixed matrix and the tails associated with a switch to a grain size sensitive deformation mechanism was achieved (e.g., Rutter and Brodie, 1988).

5.1.3 Grain size evolution

The change in the overall microstructure in the shear zone, interpreted as a continuous decrease in grain size towards the SZB by several authors (e.g., Obata, 1980; Précigout et al., 2007; Van Der Wal and Vissers, 1996) should be strongly related to the change in grain shape and grain size of the mixed matrix between tectonites and mylonites described above. In agreement with Johanesen and Platt (2015), who reported a rather constant grain size of recrystallized olivine (~130 μm) with regional variations in mylonites and tectonites, neoblast grain sizes of all phases and from all microstructural domains stay constant over the entire mylonitic shear zone. Accordingly, and following Johanesen and Platt (2015), the trend of decreasing total grain size with decreasing distance to the SZB reported by previous studies is explained by the increasing amount of neoblasts rather than by a systematically change in their grain size. Only the outermost, tectonic sample shows

larger grain sizes in the mixed matrix domain, whereas grain sizes in pyroxene neoblast tails remain constant but have a bigger spread. Furthermore, an excursion towards bigger grain sizes (deviation ~50 µm) comparable to the variations found by Johanesen and Platt (2015) is present in the mixed matrix and in orthopyroxene neoblast tails at ~290 m distance to the SZB. Due to a smaller number of analyzed microstructures in these samples, the excursion is only rudimentary present for neoblasts of cpx tails. As these local variations are present for most phases in multiple microstructural domains, they indicate variations in differential stress independent of the distance to the SZB. Corroborating the results of Johanesen and Platt (2015), no gradual increase of stress towards the SZB is indicated in our data, which would result in a gradual decrease in grain size. In contrast to the average recrystallized olivine grain size of ~130 µm from Johanesen and Platt (2015) our average grain sizes are smaller for all phases and all microstructural domains (< 100 µm). Reporting only the grain size of recrystallized olivine, which was excluded for matrix microstructures in this study due to uncertainties caused by serpentinization, our grain sizes are not consistent to those of Johanesen and Platt (2015), which could explain this discrepancy. However, the increase in grain size in the tectonite unit and its coarser, less deformed microstructures corroborate different deformation histories for mylonites and tectonites as described above (section 5.1.1). Differences in the shape of primarily the neoblasts of the mixed matrix are therefore thought to be dependent on the strain of the specific unit. To that effect, the elongation of neoblasts in the mylonitic mixed matrix, the elongation of opx porphyroclasts and the elongation of pyroxene tails stretched in the foliation are interpreted as increased strain towards the SZB at almost constant stress (= constant grain sizes). The increase in strain could be either due to an increase of the strain rate (Johanesen and Platt, 2015) or a longer lasting deformation in mylonites, which will be addressed below.

5.2 Melts in the shear zone

Increasing evidence for metasomatic processes and melt rock interactions were reported closer and closer to the NW boundary of the Ronda peridotite during the last decades. The so called "recrystallization front", which separates the spinel tectonites from the coarse grained peridotites, was revealed as melting front . Soustelle et al. (2009) confirmed that Si rich melts fertilized the spinel tectonites of the NW Ronda shear zone up to 1.5 km ahead of this melting front. According to these authors, early melt pulses lead to pyroxene and spinel crystallization as irregularly shaped grains, whereas late stage, second order percolation of evolved melt caused the crystallization of interstitial, undeformed pyroxenes and spinel with a strongly enriched LREE chemistry. The melt is postulated to be derived by partial melting (2.5-6.5 % extraction) of the coarse grained peridotites (Lenoir et al., 2001). Beside melt assisted crystallization, partial melting of garnet pyroxenite layers in the tectonites and their increasing conversion into spinel pyroxenites towards the melting front can also be placed in the context of melt percolation and the steep thermal gradient from the melting front to the SZB (Garrido and Bodinier, 1999). However, even though the deformation in the entire shear zone (tectonites + mylonites) shows continuous orientations of foliation and lineation and the timing of the melt percolation is postulated to be syn- to late kinematic (Soustelle et al., 2009), the westernmost mylonite unit was so far considered either to be completely melt free (Précigout et al., 2007; Soustelle et al., 2009) or melt absent during the deformation (Johanesen & Platt, 2015). Based on our combined

970 microstructural and geochemical investigations we can extend the sphere of melt influence into the mylonites and up to the NW edge of the Ronda peridotite.
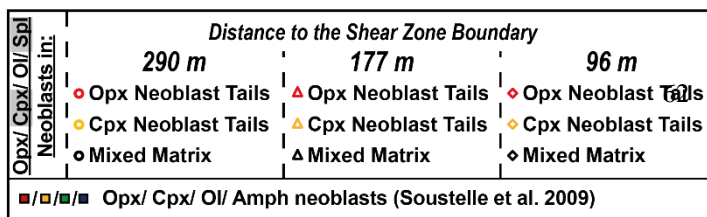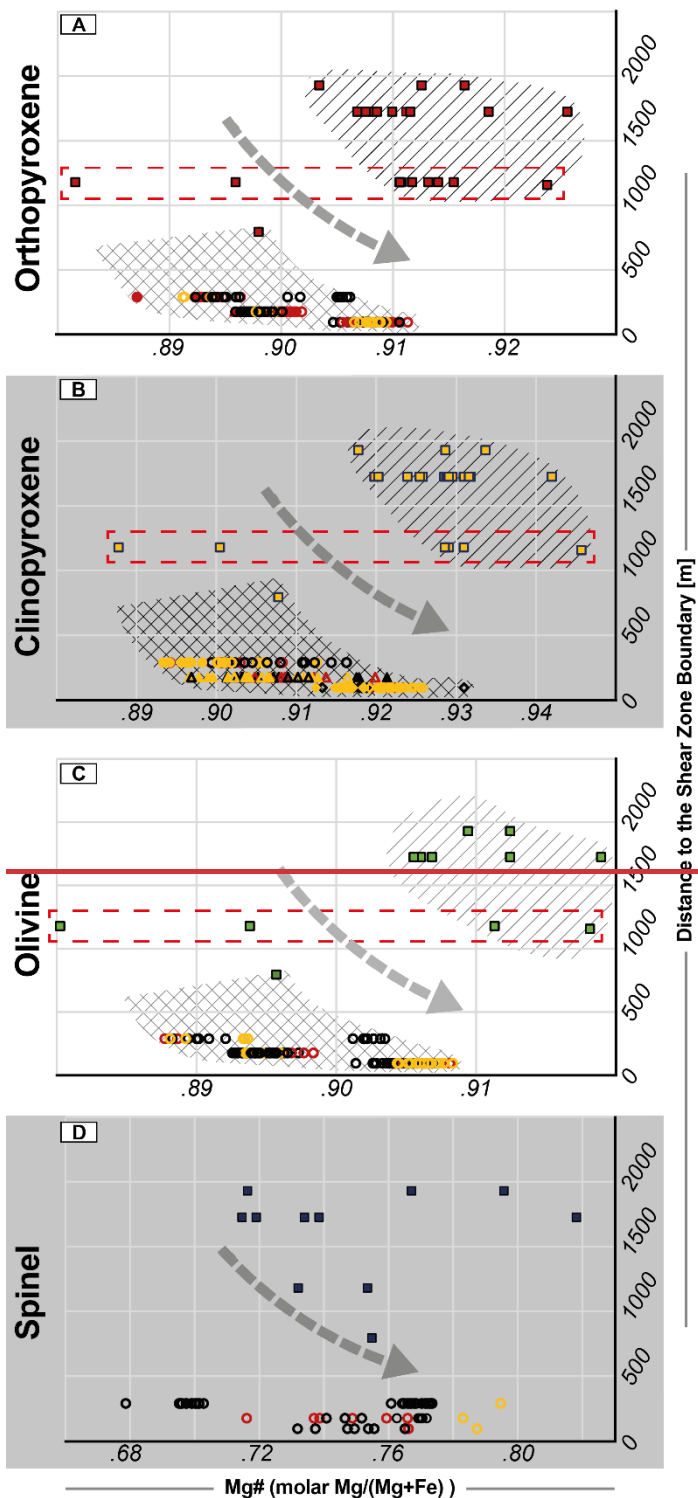
Fig. 12. Mg# data of spinel tectonites (Soustelle et al., 2009) and of spl/grt mylonites (this study) vs. distance to the SZB. Arrows indicate trend of re-fertilization. Hatched area: geochemical signature of melt in tectonites; Crosshatched area: geochemical signature of melt in mylonites. Mg# of opx (A), cpx (B), olivine (C) and spl (D) plotted against the distance to the SZB. Location of the studied area by Soustelle et al. (2009) is indicated in Fig. 1.

Following Soustelle et al. (2009), we interpret the interstitial pyroxenes and spinel of the mixed matrix in tectonites and mylonites as precipitates from percolating, re-fertilizing melt. The associated melt-rock reactions are geochemically mainly characterized by an increase in FeO (= decrease in Mg#) and TiO_2 for olivine, pyroxenes, spinel and amphibole towards the melting front, with increasing distance to the SZB respectively. The continuous geochemical trends and the presence of interstitial spinel and pyroxene neoblast between olivine crystals in the mixed matrix of both, mylonitic and tectonic samples, suggest that the re-fertilizing melts leading to pyroxene crystallization were present in the entire transect. In contrast to Soustelle et al. (2009) who reported a fertilization only 1.5 km ahead the melting front and therefore leaving the mylonitic shear zone unaffected, our data traces the re-fertilizing melts up to the SZB. In Fig. 12, data from Soustelle et al. (2009) was put in correlation to the distance to the SZB and added to the data presented here. Indicated by the grey arrows is the geochemical trend of increasing Mg# with decreasing distance to the SZB. It is obvious that the data of Soustelle et al. (2009) and our data follow this trend (Fig. 12). Anyhow, an offset is present between both data sets with data of Soustelle et al. (2009) staring to decrease from higher Mg# (~0.92) than the analyzed data herein (~0.89) (Fig. 12). This offset in Mg# between the, in regard to the SZB, distal tectonites (Soustelle et al., 2009) on the one hand, and the mylonites and tectonites closer to the SZB on the other hand (analyzed herein) is potentially the geochemical im- and overprint of multiple re-fertilization events (Fig. 12). The re-fertilization documented in our samples and characterized by lower Mg#s is in this regard assigned to an early melt impulse affecting the entire area between melting front and SZB, present day tectonites and mylonites respectively. As samples remote from the SZB (>1150-1200 m) do not follow the geochemical trend present in those analyzed herein but rather follow a new, second order trend beginning with increased Mg# for all analyzed phases (Fig. 12) a late stage melt infiltration overprinting this area close to the melting front is most plausible. Interestingly, samples with a distance of ~1150-1200 m to the SZB from Soustelle et al. (2009) record with their wide range of Mg#s apparently both re-fertilization events. Further, both re-fertilizations follow the same geochemical trend and trajectory, indicating the area beneath the structurally deeper melting front as the melt source (Fig. 12). A comprehensive sketch of the interplay of microstructural evolution and melt percolation is shown in Fig. 13. The possibility of varying source rocks being responsible for the various trends is unlikely because different lithologies (lherzolites and harzburgites) and diverse microstructures (neoblast/porphyroclasts of different domains) analyzed by Soustelle et al. (2009) and herein follow the same trend. The tendency of mixed matrix pyroxene neoblasts to lower TiO_2 and Cr_2O_3 abundances could indicate a stronger effect of diffusion on the smaller grains (Cherniak & Liang, 2012). This process could additionally be enhanced by ongoing deformation as elongated grain shape and size of the mylonitic mixed matrix suggest. The melt infiltration in the mylonites is therefore thought to be pre- to early syn-kinematic.

As no geochemical difference is present between the various microstructures, pyroxene tail assemblages are thought to be affected by the re fertilization event like the mixed matrix. The synkinematic formation of the neoblast tails is therefore attributed to the same deformation stage, which was initiated by the re fertilization of the entire shear zone. Melt infiltration has been shown to significantly reduce the mechanical strength of the upper mantle (e.g., Tommasi et al., 2017). The strength contrast between melt affected (tectonites+mylonites) and melt free areas is a plausible reason for the localization of deformation at the boundary between both areas. The flattening of the re fertilization imprint (Mg#, TiO_2) towards the present day SZB might indicate, that this boundary coincides approximately with today's SZB. With progressive deformation, the area accommodating the deformation expands further into the melt affected region, towards the melting front respectively, forming the mylonitic unit. As the strain localization starts at the boundary of the melt affected area, here the deformation is active for the longest time resulting in maximum degree of finite strain. Hence, porphyroclast elongation increases towards the boundary (present day SZB). Additionally, the increase in pyroxene porphyroclast neoblast tails with concurrent decrease of porphyroclasts towards the SZB might indicate a strain dependence. De Ronde and Stünitz (2007) reported a positive feedback between deformation and reactions in their experiments for the transition from plagioclase to spinel in olivine+plagioclase aggregates. An enhanced nucleation reaction rate was here explained by increasing deformation induced defects in the reactant and the deformation induced transportation of neoblasts away from the reaction interface, which thereby maintains a high chemical potential. For Ronda, a similar mechanism could clear the melt porphyroclast interface of neoblasts and thereby form the, in the foliation elongated, neoblast tails. With constant stresses and constant dominant deformation mechanism(s) operating in the melt affected area neoblast grain sizes are kept nearly constant.
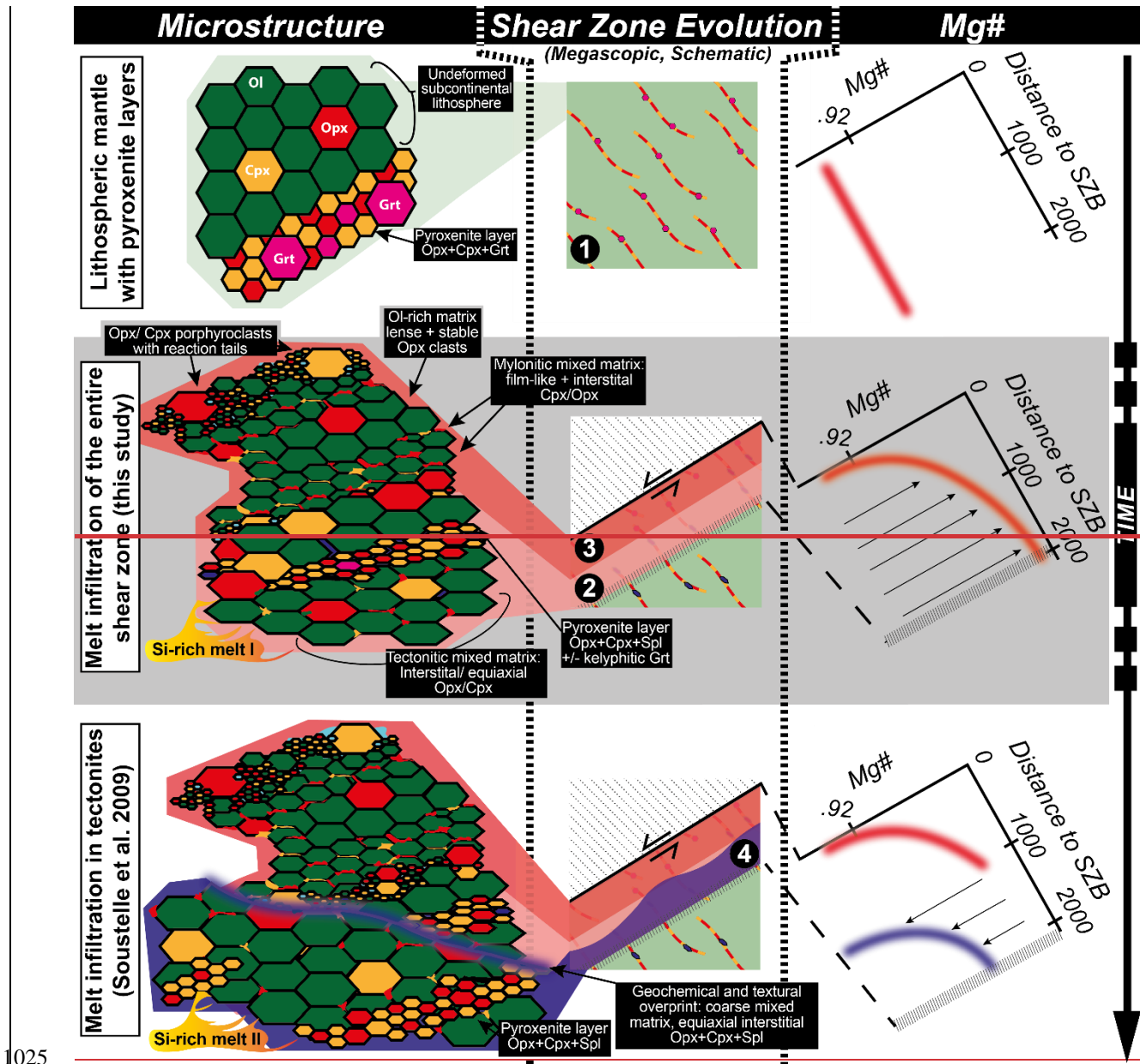
Fig. 13. Sketch of microstructural, shear zone and Mg# evolution of the NW Ronda shear zone. (1): Layered lithospheric mantle: Equilibrated assemblage of coarse olivines and pyroxenes cut by grt-bearing pyroxenite layers; homogenous Mg#. (2) and (3): Melt infiltration of the entire shear zone. Formation of mixed matrix by crystallization of interstitial pyroxenes in the entire shear zone (2). Areas little effected by melt form Ol-rich matrix. Apart from distal pyroxenites, grt is replaced by kelyphitic opx+cpx+spl. "Melting front" as origin of the re-fertilizing melts is shown as hatched area in the shear zone evolution. Fe- and Ti-rich melt shifts Mg# of pyroxenes and olivine towards lower values. Increased deformation leads to elongation of olivine and wedge-like pyroxenes in the mylonites (3). Pyroxene porphyroclasts form amph-bearing neoblast tails. Ol-rich matrix form lenses in the mixed matrix. (4) Melt

1035

5.~~3~~ 4 Late-stage fluid infiltration

For the sake of completeness, the fluid-infiltration, documented in several samples, will be addressed in the following section (see also ~~Fig. 9~~Fig. 10). The crosscutting of amphibole-filled cracks of entire cpx porphyroclasts, the replacing of cpx exsolution lamellae in opx porphyroclasts by amphibole described by Obata (1980) and the formation of amphibole and

1040 clinopyroxene rich veins oblique to the ~~formation~~ foliation indicate a late-stage fluid infiltration without relation to the melt infiltration and deformation processes discussed above. Since these observations were primarily made in mylonites close to the ~~SZB~~NW-B, a fluid infiltration originating from the adjacent metasedimentary Jubrique unit seems plausible. Lower Ti abundances for amphibole, clino- and orthopyroxene neoblasts and amphibole Mg#s not comparable (<0.86) to those of other microstructural domains corroborate an independent formation process. Interestingly, the formation of serpentine

1045 seems to follow these structures when present.

5.~~4~~ 5 Reactions and deformation

Like for most studied upper mantle shear zones, the results presented for the Ronda shear zone point to a key-role of reactions in the evolution of upper mantle shear zones (e.g., Dijkstra et al., 2004). A comparison between these studies suggests that the impact of reactions on the evolution of shear zones depends rather on the timing than on the type of

1050 reaction:

Tommasi et al. (2017) have shown that hydrous Si-rich melts significantly affect the ~~rheological~~ mechanical strength of the upper mantle and favour a strain localization in the melt-effected region. Additionally, melt-rock reactions in low strain microstructures of the Lanzo shear zone indicate melt-presence during initial shearing (Kaczmarek and Müntener, 2008). Beside phase mixing by crystallization of pyroxene neoblasts interstitially and at the reacting boundaries of coarser olivine in

1055 combination with the activity of a grain size sensitive creep mechanism (Hirth and Kohlstedt, 2003; Platt and Behr, 2011), an additional effect is the reduction of the ~~viscosity~~ strength by "wetting" of the grain boundaries (e.g., Hirth and Kohlstedt, 1995). As these effects are solely dependent on the presence of melt, they also are most likely decisive for early localization of strain in the upper mantle.

For syn-tectonic, high stress conditions during the later stages of the shear zone evolution, metasomatic and metamorphic

1060 reactions were shown to be decisive for the formation of ultramylonitic neoblast assemblages either in pyroxene porphyroclasts tails or in ultramylonitic bands: In the shear zones of Othris and Erro Tobbio, melt-rock reactions formed ultramylonitic, mixed tails dominated by pyroxene and olivine (Dijkstra et al., 2002; Linckens and Tholen, 2021). Metamorphic reactions in relation to the phase transitions of garnet, spinel and plagioclase triggered reactions at pyroxene porphyroclasts and the formation of ultramylonitic assemblages in shear zones of the Uenzaru peridotite complex, the Turon

1065 de Técouère peridotite body and the Lanzo peridotite massif (Furusho and Kanagawa, 1999; Newman et al., 1999; Tholen et

al., 2022). Fluid presence enhancing dissolution-precipitation creep and leading to the formation of ultramylonites was reported for shear zones at the transition from plagioclase to granular peridotite in central Ronda (Hidas et al., 2016) and in the Anita Peridotite (Czertowicz et al., 2016). Phase mixing with amphibole and/or chlorite in ultramylonitic assemblages was reported for Erro-Tobbio (Hoogerduijn Strating et al., 1993; Linckens and Tholen, 2021) and the Shaka and Prince Edward transform fault (Kohli and Warren, 2020; Prigent et al., 2020). Diffusion creep and GBS as dominant deformation process in these ultramylonitic assemblages weaken the rheology significantly leading to further strain localization in the shear zones if the ultramylonitic areas are interconnected (e.g., de Ronde et al., 2005).

To summarize: ~~R~~Metasomatic and metamorphic reactions weaken the upper mantle and lead to strain localization. The degree of strain localization seems to ~~dependen~~dependent~~t~~ on the timing of the reaction in the course of the shear zone evolution, but not on the nature of the reaction itself. In the case of Ronda, ~~extensive melt infiltration~~pre- to early syn-kinematic metasomatic reactions formed the mixed matrix and the neoblast tails ~~localized the deformation~~ over a km-scale area in tectonites and mylonites and thereby shaped the shear zone. High mixing intensities and resulting homogenous grain sizes in the mylonitic mixed matrix ensured that no further strain localization did occur in ~~porphyroclast'~~ porphyroclasts reaction tails. In the shear zones of Othris (Dijkstra et al., 2002), Erro-Tobbio (Linckens and Tholen, 2021), Uenzaru (Furusho and Kanagawa, 1999), Turon de Técouère (Newman et al., 1999) and central Ronda (Hidas et al., 2016) syn-kinematic melt/fluid-assisted and/or metamorphic reactions under high stress conditions led to the formation of mixed ultramylonitic bands. In these bands strain is further localized in the dm- to cm-scale by a switch to diffusion creep as dominant deformation mechanism.

6 Conclusions

Nearly homogenous microstructures and geochemical composition indicate a pervasive metasomatism of the entire NW Ronda shear zone, forming a dominant mixed matrix with embedded pyroxene porphyroclasts with neoblast tails. The mixed matrix is characterized by interstitial secondary grains (opx, spl $\pm$ cpx) in between pristine, coarse pyroxenes and olivine. Tails of ortho- and clinopyroxene porphyroclasts consist of a constant phase assemblage (cpx, opx, ol, spl, amph) and AG- or B-type olivine CPOs. Highly lobate phase boundaries, irregular grain shapes, intense, homogeneous phase mixing and dispersed interstitial secondary grains suggest the formation of both, matrix and pyroxene tails by metasomatic reactions. Published syn-deformational temperature estimates (800-900° C at 1.95-2.00 GPa), amphibole abundances, olivine B-type CPOs and the consistency in microstructures of grt/spl-mylonites of the Beni Bousera massif (Morocco, Gibraltar arc) point to a OH-bearing metasomatism by small fractions of evolved melts, which did not reset the equilibrium temperatures. Beside this common genesis, there is a difference in the deformation history of both shear zone units (tectonites/ mylonites). Distributed neoblast precipitation, equiaxial neoblast grain shapes and weak pyroxene CPOs indicate weaker deformation of the tectonite unit. In the mixed matrix of the mylonite unit film/wedge-shaped pyroxenes are oriented along olivine grain boundaries subparallel to the foliation pointing to dissolution-precipitation during deformation. However, strong CPOs of all

phases, high dislocation density in neoblasts of the mixed matrix and the elongation of all grains suggest dislocation creep as the main deformation mechanism in the entire transect. The overlap of deformation and reaction fabrics in the mylonites suggest a pre- to early syn-kinematic metasomatism. ~~Microstructural and geochemical analysis of the major microstructural domains of the NW Ronda shear zone document a multistage melt-derived re-fertilization with a fundamental impact on strain localization and the formation of the km-scale shear zone. The interaction of melt and deformation in the course of the shear zone evolution can be illustrated by the following bullet points (see also Fig. 13):~~

~~1) The initial, largely undeformed rock belongs to a coarse grained lithospheric mantle (ol+opx+cpx) with a relatively homogenous composition and layers of grt-bearing pyroxenites.~~

~~2) Melt infiltration re-fertilizes the complete present-day shear zone. Strain localization is initiated by melt-enhanced deformation and grain size reduction by the crystallization of interstitial pyroxenes and the subsequent activation of a grain-size sensitive deformation mechanism. Potential dominant deformation mechanisms are DRX creep and/or DisGBS. The change in composition (Mg#↓, Fe↑, Cr↓) of pyroxenes and olivine and its fading towards the shear zone boundary suggest that the area affected by strain localization is strongly dependent on the presence of melt. At the shear zone boundary, areas little effected by melt preserve garnets (Garrido et al., 2011).~~

~~3) Increased deformation localized in the melt-affected areas led to the formation of mylonites. With constant stress over the entire melt-affected area but an earlier onset of deformation at the shear zone boundary a strain gradient is formed. Its microstructural evidence are the increasing elongation of orthopyroxene porphyroclasts, neoblasts and the boudinage of pyroxenitic layers towards the shear zone boundary. Furthermore, deformation induced reactions led to an increase of neoblast formation in reaction tails and the decrease of pyroxene porphyroclasts in mylonites situated close to the shear zone boundary.~~

~~4) Secondary melts infiltrate the tectonites up to ~1.5 km ahead of the melting front (Soustelle et al., 2009). Microstructures are affected by recrystallization and increase in Mg#. The geochemical signature formed in step 2 is overprinted. Equiaxial pyroxenes with low internal deformation corroborate a late-kinematic timing (Soustelle et al., 2009).~~

Supplementary data (attached as .zip file)

S1 - EPMA measurement settings and detection limits.

S2 – Microstructural data of all analysed (EBSD) microstructures.

~~S3 – CPO overview of all analysed (EBSD) microstructures.~~

S3~~4~~ – Complete EPMA data.

S4~~5~~ – EPMA additional graphs. Additional graphs for clinopyroxene, olivine and amphibole.

Author contribution

Sören Tholen: Conceptualization, Methodology, Software, Validation, Formal analysis, Investigation, Data Curation, Writing, Visualization, Project administration. **Jolien Linckens:** Conceptualization, Validation, Methodology, Resources, Project administration, Supervision, Funding acquisition, Writing (Review). **Gernold Zulauf:** Resources, Writing (Review), Funding acquisition.

Competing Interests

The authors declare that they have no conflict of interest.

Acknowledgments

For fruitful discussions and comments along the way, we want to thank Alan Woodland, Catharina Heckel, Reiner Kleinschrodt and Marina Kemperle. Additionally, the authors want to thank Andréa Tommasi and Jacques Précigout for their revision and their constructive feedback which improved the manuscript significantly. Illuminating field information were provided by Jacques Précigout and Carlos J. Garrido. Without the help of Thomas González and his team at the Sabinillas Bookstore, most of our samples would have fallen victim to dodgy transport companies and COV-19 restrictions, thank you very much! For superb sample preparation Maria Bladt and Nils Prawitz are to be thanked. We are grateful for the collaboration with the Institute of Geology and Mineralogy Cologne and want to thank again Reiner Kleinschrodt, Patrick Grunert and Hannah Cieszynski. This project was made possible by funds of the Deutsche Forschungsgemeinschaft (DFG) [LI 2888/2-1].

References

Bachmann, F., Hielscher, R., & Schaeben, H. (2010). Texture analysis with MTEX- Free and open source software toolbox. *Solid State Phenomena*, *160*, 63–68. https://doi.org/10.4028/www.scientific.net/SSP.160.63

Balanyá, J. C., García-Dueñas, V., Azañón, J. M., & Sánchez-Gómez, M. (1997). Alternating contractional and extensional events in the Alpujarride nappes of the Alboran Domain (Betics, Gibraltar Arc). *Tectonics*, *16*(2), 226–238. https://doi.org/10.1029/96TC03871

Barich, A., Acosta-Vigil, A., Garrido, C. J., Cesare, B., Tajčmanová, L., & Bartoli, O. (2014). Microstructures and petrology of melt inclusions in the anatectic sequence of Jubrique (Betic Cordillera, S Spain): Implications for crustal anatexis. *Lithos*, *206–207*(1), 303–320. https://doi.org/10.1016/j.lithos.2014.08.003

Bergmann, R., Chan, R. H., Hielscher, R., Persch, J., & Steidl, G. (2016). Restoration of manifold-valued images by half-quadratic minimization. *Inverse Problems and Imaging*, *10*(2), 281–304. https://doi.org/10.3934/ipi.2016001

Bercovici, D., & Ricard, Y. (2014). Plate tectonics, damage and inheritance. *Nature*, *508*(7497), 513–516. https://doi.org/10.1038/nature13072

Beyer, E. E., Griffin, W. L., & O'Reilly, S. Y. (2006). Transformation of archaean lithospheric mantle by refertilization: Evidence from exposed peridotites in the Western Gneiss Region, Norway. *Journal of Petrology*, *47*(8), 1611–1636. https://doi.org/10.1093/petrology/egl022

Blatter, D. L., & Carmichael, I. S. E. (1998). Plagioclase-free andesites from Zitácuaro (Michoacán), Mexico: Petrology and experimental constraints. *Contributions to Mineralogy and Petrology*, *132*(2), 121–138. https://doi.org/10.1007/s004100050411

Bonadiman, C., Nazzareni, S., Coltorti, M., Comodi, P., Giuli, G., & Faccini, B. (2014). Crystal chemistry of amphiboles: Implications for oxygen fugacity and water activity in lithospheric mantle beneath Victoria Land, Antarctica. *Contributions to Mineralogy and Petrology*, *167*(3), 1–17. https://doi.org/10.1007/s00410-014-0984-8

Booth-Rea, G., Ranero, C. R., Grevemeyer, I., & Martínez-Martínez, J. M. (2007). Crustal types and tertiary tectonic evolution of the Alborán sea, western Mediterranean. *Geochemistry, Geophysics, Geosystems*, *8*(10), 1–25. https://doi.org/10.1029/2007GC001639

Borghini, G. (2008). The spinel- to plagioclase-facies transition in mantle peridotites: Natural and experimental constraints. *Plinius*, *34*(January 2008), 43–45.

Boullier, A. M., & Gueguen, Y. (1975). SP-Mylonites: Origin of some mylonites by superplastic flow. *Contributions to Mineralogy and Petrology*, *50*(2), 93–104. https://doi.org/10.1007/BF00373329

Bunge, H.-J. (1982). Orientation Distributions. In *Texture Analysis in Materials Science*. London: Butterworths. https://doi.org/10.1016/B978-0-408-10642-9.50008-8

Cherniak, D. J., & Liang, Y. (2012). Ti diffusion in natural pyroxene. *Geochimica et Cosmochimica Acta*, *98*, 31–47. https://doi.org/10.1016/j.gca.2012.09.021

Coltorti, M., Beccaluva, L., Bonadiman, C., Faccini, B., Ntaflos, T., & Siena, F. (2004). Amphibole genesis via metasomatic reaction with clinopyroxene in mantle xenoliths from Victoria Land, Antarctica. *Lithos*, *75*(1–2), 115–139. https://doi.org/10.1016/j.lithos.2003.12.021

Coltorti, M., Bonadiman, C., Faccini, B., Grégoire, M., O'Reilly, S. Y., & Powell, W. (2007). Amphiboles from suprasubduction and intraplate lithospheric mantle. *Lithos*, *99*(1–2), 68–84. https://doi.org/10.1016/j.lithos.2007.05.009

Cross, A. J., & Skemer, P. (2017). Ultramylonite generation via phase mixing in high-strain experiments. *Journal of Geophysical Research: Solid Earth*, *122*(3), 1744–1759. https://doi.org/10.1002/2016JB013801

Czertowicz, T. A., Toy, V. G., & Scott, J. M. (2016). Recrystallisation , phase mixing and strain localisation in peridotite during rapid extrusion of sub-arc mantle lithosphere. *Journal of Structural Geology*, *88*, 1–19. https://doi.org/10.1016/j.jsg.2016.04.011

Davies, G. R., Nixon, P. H., Pearson, D. G., & Obata, M. (1993). Tectonic implications of graphitized diamonds from the Ronda peridotite massif, southern Spain. *Geology*, *21*(5), 471–474. https://doi.org/10.1130/0091-7613(1993)021<0471:TIOGDF>2.3.CO;2

Dijkstra, A. H., Drury, M. R., Vissers, R. L. M., & Newman, J. (2002). On the role of melt-rock reaction in mantle shear zone formation in the Othris Peridotite Massif (Greece). *Journal of Structural Geology*, *24*(9), 1431–1450. https://doi.org/10.1016/S0191-8141(01)00142-0

Dijkstra, A. H., Drury, M. R., Vissers, R. L. M., Newman, J., & Van Roermund, H. L. M. (2004). Shear zones in the upper mantle: Evidence from alpine- and ophiolite-type peridotite massifs. *Geological Society Special Publication*, *224*, 11–24. https://doi.org/10.1144/GSL.SP.2004.224.01.02

Drury, M. R., & Urai, J. L. (1989). Deformation-related recrystallization processes. *Tectonophysics*, *172*, 235–253. https://doi.org/https://doi.org/10.1016/0040-1951(90)90033-5

Drury, M. R., Vissers, R. L. M., Van der Wal, D., & Hoogerduijn Strating, E. H. (1991). Shear localisation in upper mantle peridotites. *Pure and Applied Geophysics PAGEOPH*, *137*(4), 439–460. https://doi.org/10.1007/BF00879044

Esteban, J. J., Cuevas, J., Tubía, J. M., Sergeev, S., & Larionov, A. (2011). A revised Aquitanian age for the emplacement of the Ronda peridotites (Betic Cordilleras, southern Spain). *Geological Magazine*, *148*(1), 183–187. https://doi.org/10.1017/S0016756810000737

Esteban, José Julián, Sánchez-Rodríguez, L., Seward, D., Cuevas, J., & Tubía, J. M. (2004). The late thermal history of the Ronda area, southern Spain. *Tectonophysics*, *389*(1–2), 81–92. https://doi.org/10.1016/j.tecto.2004.07.050

Esteban, José Julián, Cuevas, J., Vegas, N., & Tubía, J. M. (2008). Deformation and kinematics in a melt-bearing shear zone from the Western Betic Cordilleras (Southern Spain). *Journal of Structural Geology*, *30*(3), 380–393. https://doi.org/10.1016/j.jsg.2007.11.010

Frets, E., Tommasi, A., Garrido, C. J., Padrón-Navarta, J. A., Amri, I., & Targuisti, K. (2012). Deformation processes and rheology of pyroxenites under lithospheric mantle conditions. *Journal of Structural Geology*, *39*(June), 138–157. https://doi.org/10.1016/j.jsg.2012.02.019

Frets, E., Tommasi, A., Garrido, C., Vauchez, A., Mainprice, D., Kamaltarguisti, & Amri, I. (2014). The beni bousera peridotite (rif belt, morocco): An oblique-slip low-angle shear zone thinning the subcontinental mantle lithosphere. *Journal of Petrology*, *55*(2), 283–313. https://doi.org/10.1093/petrology/egt067

Furusho, M., & Kanagawa, K. (1999). Transformation-induced strain localization in a lherzolite mylonite from the Hidaka metamorphic belt of central Hokkaido, Japan. *Tectonophysics*, *313*(4), 411–432. https://doi.org/10.1016/S0040-1951(99)00215-2

Garrido, C. J., & Bodinier, J. L. (1999). Diversity of mafic rocks in the Ronda peridotite: Evidence for pervasive melt-rock reaction during heating of subcontinental lithosphere by upwelling asthenosphere. *Journal of Petrology*, *40*(5), 729–754. https://doi.org/10.1093/petroj/40.5.729

Garrido, C. J., Gueydan, F., Booth-Rea, G., Précigout, J., Hidas, K., Padrón-Navarta, J. A., & Marchesi, C. (2011). Garnet lherzolite and garnet-spinel mylonite in the Ronda peridotite: Vestiges of Oligocene backarc mantle lithospheric extension in the western Mediterranean. *Geology*, *39*(10), 927–930. https://doi.org/10.1130/G31760.1

Hidas, K., Booth-Rea, G., Garrido, C. J., Martínez-Martínez, J. M., Padrón-Navarta, J. A., Konc, Z., et al. (2013). Backarc basin inversion and subcontinental mantle emplacement in the crust: Kilometre-scale folding and shearing at the base of the proto-alborán lithospheric mantle (Betic Cordillera, southern Spain). *Journal of the Geological Society*, *170*(1), 47–55. https://doi.org/10.1144/jgs2011-151

Hidas, K., Garrido, C. J., Tommasi, A., Padrón-Navarta, J. A., Thielmann, M., Konc, Z., et al. (2013). Strain localization in pyroxenite by reaction-enhanced softening in the shallow subcontinental lithospheric mantle. *Journal of Petrology*, *54*(10), 1997–2031. https://doi.org/10.1093/petrology/egt039

Hidas, K., Tommasi, A., Garrido, C. J., Padrón-Navarta, J. A., Mainprice, D., Vauchez, A., et al. (2016). Fluid-assisted strain localization in the shallow subcontinental lithospheric mantle. *Lithos*, *262*(October), 636–650. https://doi.org/10.1016/j.lithos.2016.07.038

Hiraga, T., Miyazaki, T., Yoshida, H., & Zimmerman, M. E. (2013). sliding Comparison of microstructures in superplastically deformed synthetic materials and natural mylonites : Mineral aggregation via grain boundary sliding. https://doi.org/10.1130/G34407.1

Hirth, G., & Kohlstedt, D. (2003). Rheology of the upper mantle and the mantle wedge: A view from the experimentalists. *Geophysical Monograph Series*, *138*, 83–105. https://doi.org/10.1029/138GM06

Hirth, G., & Kohlstedt, D. L. (1995). Experimental constraints on the dynamics of the partially molten upper mantle: deformation in the diffusion creep regime. *Journal of Geophysical Research*, *100*(B2), 1981–2001. https://doi.org/10.1029/94JB02128

Hoogerduijn Strating, E. H., Rampone, E., Piccardo, G. B., Drury, M. R., & Vissers, R. L. M. (1993). Subsolidus emplacement of mantle peridotites during incipient oceanic rifting and opening of the mesozoic tethys (voltri massif, NW Italy). *Journal of Petrology*, *34*(5), 901–927. https://doi.org/10.1093/petrology/34.5.901

Hu, W. J., Zhong, H., Chu, Z. Y., Zhu, W. G., Bai, Z. J., & Zhang, C. (2020). Ancient Refertilization Process Preserved in the Plagioclase Peridotites: An Example From the Shuanggou Ophiolite, Southwest China. *Journal of Geophysical Research: Solid Earth*, *125*(1), 1–21. https://doi.org/10.1029/2019JB017552

Ishimaru, S., Arai, S., Ishida, Y., Shirasaka, M., & Okrugin, V. M. (2007). Melting and multi-stage metasomatism in the mantle wedge beneath a frontal arc inferred from highly depleted peridotite xenoliths from the avacha volcano, Southern Kamchatka. *Journal of Petrology*, *48*(2), 395–433. https://doi.org/10.1093/petrology/egl065

Johanesen, K., Platt, J. P., Kaplan, M. S., & Ianno, A. J. (2014). A revised thermal history of the Ronda peridotite, S. Spain: New evidence for excision during exhumation. *Earth and Planetary Science Letters*, *393*, 187–199. https://doi.org/10.1016/j.epsl.2014.01.024

Johanesen, K. E., & Platt, J. P. (2015). Rheology, microstructure, and fabric in a large scale mantle shear zone, Ronda Peridotite, southern Spain. *Journal of Structural Geology*, *73*, 1–17. https://doi.org/10.1016/j.jsg.2015.01.007

Jung, H., & Karato, S. I. (2001). Water-induced fabric transitions in olivine. *Science*, *293*(5534), 1460–1463. https://doi.org/10.1126/science.1062235

Jung, Haemyeong. (2017). Crystal preferred orientations of olivine, orthopyroxene, serpentine, chlorite, and amphibole, and implications for seismic anisotropy in subduction zones: a review. *Geosciences Journal*, *21*(6), 985–1011. https://doi.org/10.1007/s12303-017-0045-1

Jung, Haemyeong, Katayama, I., Jiang, Z., Hiraga, T., & Karato, S. (2006). Effect of water and stress on the lattice-preferred orientation of olivine. *Tectonophysics*, *421*(1–2), 1–22. https://doi.org/10.1016/j.tecto.2006.02.011

Kaczmarek, M. A., & Müntener, O. (2008). Juxtaposition of melt impregnation and high-temperature shear zones in the upper mantle; field and petrological constraints from the lanzo peridotite (Northern Italy). *Journal of Petrology*, *49*(12), 2187–2220. https://doi.org/10.1093/petrology/egn065

Karato, S., Jung, H., Katayama, I., & Skemer, P. (2008). Geodynamic Significance of Seismic Anisotropy of the Upper Mantle: New Insights from Laboratory Studies. *Annual Review of Earth and Planetary Sciences*, *36*(1), 59–95. https://doi.org/10.1146/annurev.earth.36.031207.124120

Kelemen, P. B., & Hirth, G. (2007). A periodic shear-heating mechanism for intermediate-depth earthquakes in the mantle. *Nature*, *446*(7137), 787–790. https://doi.org/10.1038/nature05717

Kilian, R., Bestmann, M., & Heilbronner, R. (2016). Absolute orientations from EBSD measurements - as easy as it seems ? *Geophysical Research Abstracts*, *18*, 8221.

Kohli, A. H., & Warren, J. M. (2020). Evidence for a Deep Hydrologic Cycle on Oceanic Transform Faults. *Journal of Geophysical Research: Solid Earth*, *125*(2), 1–23. https://doi.org/10.1029/2019JB017751

Lenoir, X., Garrido, C. J., Bodinier, J. L., Dautria, J. M., & Gervilla, F. (2001). The recrystallization front of the Ronda

periodite: Evidence for melting and thermal erosion of subcontinental lithospheric mantle beneath the Alboran basin. *Journal of Petrology*, *42*(1), 141–158. https://doi.org/10.1093/petrology/42.1.141

Linckens, J., & Tholen, S. (2021). Formation of ultramylonites in an upper mantle shear zone, erro-tobbio, italy. *Minerals*, *11*(10). https://doi.org/10.3390/min11101036

Linckens, J., Herwegh, M., Mntener, O., & Mercolli, I. (2011). Evolution of a polymineralic mantle shear zone and the role of second phases in the localization of deformation. *Journal of Geophysical Research: Solid Earth*, *116*(6), 1–21. https://doi.org/10.1029/2010JB008119

Linckens, J., Herwegh, M., & Müntener, O. (2015). Small quantity but large effect - How minor phases control strain localization in upper mantle shear zones. *Tectonophysics*, *643*, 26–43. https://doi.org/10.1016/j.tecto.2014.12.008

Lonergan, L. (1993). Timing and kinematics of deformation in the Malaguide Complex, internal zone of the Betic Cordillera, southeast Spain. *Tectonics*, *12*(2), 460–476. https://doi.org/10.1029/92TC02507

Mameri, L., Tommasi, A., Signorelli, J., & Hansen, L. N. (2019). Predicting viscoplastic anisotropy in the upper mantle: a comparison between experiments and polycrystal plasticity models. *Physics of the Earth and Planetary Interiors*, *286*(October 2018), 69–80. https://doi.org/10.1016/j.pepi.2018.11.002

Mandler, B. E., & Grove, T. L. (2016). Controls on the stability and composition of amphibole in the Earth's mantle. *Contributions to Mineralogy and Petrology*, *171*(8–9), 1–20. https://doi.org/10.1007/s00410-016-1281-5

Mizukami, T., Wallis, S. R., & Yamamoto, J. (2004). Natural examples of olivine lattice preferred orientation patterns with a flow-normal a-axis maximum. *Nature*, *427*(6973), 432–436. https://doi.org/10.1038/nature02179

Müntener, O., & Piccardo, G. B. (2003). Melt migration in ophiolitic peridotites: The message from Alpine-Apennine peridotites and implications for embryonic ocean basins. *Geological Society Special Publication*, *218*(Anonymous 1972), 69–89. https://doi.org/10.1144/GSL.SP.2003.218.01.05

Newman, J., Lamb, W. M., Drury, M. R., & Vissers, R. L. M. (1999). Deformation processes in a peridotite shear zone: Reaction-softening by an H2O-deficient, continuous net transfer reaction. *Tectonophysics*, *303*(1–4), 193–222. https://doi.org/10.1016/S0040-1951(98)00259-5

Obata, M. (1980). The ronda peridotite: Garnet-, spinel-, and plagioclase-lherzolite facies and the P-T trajectories of a high-temprature mantle intrusion. *Journal of Petrology*, *21*(3), 533–572. https://doi.org/10.1093/petrology/21.3.533

Ohuchi, T., Karato, S., & Fujino, K. (2011). Strength of single-crystal orthopyroxene under lithospheric conditions. *Contributions to Mineralogy and Petrology*, *161*(6), 961–975. https://doi.org/10.1007/s00410-010-0574-3

Pantleon, W. (2008). Resolving the geometrically necessary dislocation content by conventional electron backscattering diffraction. *Scripta Materialia*, *58*(11), 994–997. https://doi.org/10.1016/j.scriptamat.2008.01.050

Passchier, C. W., & Trouw, R. A. J. (1996). *Microtectonics*. Springer, Berlin, Heidelberg: Springer-Verlag Berlin Heidelberg. https://doi.org/10.1007/3-540-29359-0

Platt, J. P., & Behr, W. M. (2011). Grainsize evolution in ductile shear zones: Implications for strain localization and the strength of the lithosphere. *Journal of Structural Geology*, *33*(4), 537–550. https://doi.org/10.1016/j.jsg.2011.01.018

Platt, J. P., Argles, T. W., Carter, A., Kelley, S. P., Whitehouse, M. J., & Lonergan, L. (2003). Exhumation of the Ronda peridotite and its crustal envelope: Constraints from thermal modelling of a P-T-time array. *Journal of the Geological Society*, *160*(5), 655–676. https://doi.org/10.1144/0016-764902-108

Platt, J. P., Kelley, S. P., Carter, A., & Orozco, M. (2005). Timing of tectonic events in the Alpujárride Complex, Betic

Cordillera, southern Spain. *Journal of the Geological Society*, *162*(3), 451–462. https://doi.org/10.1144/0016-764903-039

Platt, J. P., Anczkiewicz, R., Soto, J. I., Kelley, S. P., & Thirlwall, M. (2006). Early Miocene continental subduction and rapid exhumation in the western Mediterranean. *Geology*, *34*(11), 981–984. https://doi.org/10.1130/G22801A.1

Précigout, J., & Hirth, G. (2014). B-type olivine fabric induced by grain boundary sliding. *Earth and Planetary Science Letters*, *395*, 231–240. https://doi.org/10.1016/j.epsl.2014.03.052

Précigout, J., & Stünitz, H. (2016). Evidence of phase nucleation during olivine diffusion creep : A new perspective for mantle strain localisation, *455*, 94–105. https://doi.org/10.1016/j.epsl.2016.09.029

Précigout, J., Gueydan, F., Gapais, D., Garrido, C. J., & Essaifi, A. (2007). Strain localisation in the subcontinental mantle - a ductile alternative to the brittle mantle. *Tectonophysics*, *445*(3–4), 318–336. https://doi.org/10.1016/j.tecto.2007.09.002

Précigout, J., Gueydan, F., Garrido, C. J., Cogné, N., & Booth-Rea, G. (2013). Deformation and exhumation of the Ronda peridotite (Spain). *Tectonics*, *32*(4), 1011–1025. https://doi.org/10.1002/tect.20062

Prigent, C., Warren, J. M., Kohli, A. H., & Teyssier, C. (2020). Fracture-mediated deep seawater flow and mantle hydration on oceanic transform faults. *Earth and Planetary Science Letters*, *532*, 115988. https://doi.org/10.1016/j.epsl.2019.115988

Puga, E., Nieto, J. M., Díaz De Federico, A., Bodinier, J. L., & Morten, L. (1999). Petrology and metamorphic evolution of ultramafic rocks and dolerite dykes of the Betic Ophiolitic Association (Mulhacen Complex, SE Spain): Evidence of eo-Alpine subduction following an ocean-floor metasomatic process. *Lithos*, *49*(1–4), 23–56. https://doi.org/10.1016/S0024-4937(99)00035-3

Putnis, A., Niedermeier, D. R. D., & Putnis, C. V. (2006). From epitaxy to topotaxy: The migration of reaction interfaces through crystals. *Geochimica et Cosmochimica Acta*, *70*(18), A509. https://doi.org/10.1016/j.gca.2006.06.1479

Rapp, R. P., Shimizu, N., Norman, M. D., & Applegate, G. S. (1999). Reaction between slab-derived melts and peridotite in the mantle wedge: Experimental constraints at 3.8 GPa. *Chemical Geology*, *160*(4), 335–356. https://doi.org/10.1016/S0009-2541(99)00106-0

de Ronde, A. A., & Stünitz, H. (2007). Deformation-enhanced reaction in experimentally deformed plagioclase-olivine aggregates. *Contributions to Mineralogy and Petrology*, *153*(6), 699–717. https://doi.org/10.1007/s00410-006-0171-7

de Ronde, A. A., Stünitz, H., Tullis, J., & Heilbronner, R. (2005). Reaction-induced weakening of plagioclase-olivine composites. *Tectonophysics*, *409*(1–4), 85–106. https://doi.org/10.1016/j.tecto.2005.08.008

Ross, J. V., & Nielsen, K. C. (1978). FLOW OF WET POLYCRYSTALLINE Orthopyroxene is a common mineral in ultramafic rocks and together with olivine is believed to be a major component of mantle material . Me- chanical data and flow laws are known for olivine under both " wet " and " dry " condi. *Tectonophysics*, *44*, 233–261.

Rossetti, F., Faccenna, C., & Crespo-Blanc, A. (2005). Structural and kinematic constraints to the exhumation of the Alpujarride Complex (Central Betic Cordillera, Spain). *Journal of Structural Geology*, *27*(2), 199–216. https://doi.org/10.1016/j.jsg.2004.10.008

Le Roux, V., Bodinier, J. L., Tommasi, A., Alard, O., Dautria, J. M., Vauchez, A., & Riches, A. J. V. (2007). The Lherz spinel lherzolite: Refertilized rather than pristine mantle. *Earth and Planetary Science Letters*, *259*(3–4), 599–612. https://doi.org/10.1016/j.epsl.2007.05.026

Rutter, E. H., & Brodie, K. H. (1988). The role of tectonic grain size reduction in the rheological stratification of the

lithosphere. *Geologische Rundschau*, 77(1), 295–307. https://doi.org/10.1007/BF01848691

Sen, C., & Dunn, T. (1995). Experimental modal metasomatism of a spinel lherzolite and the production of amphibole-bearing peridotite. *Contributions to Mineralogy and Petrology*, 119(4), 422–432. https://doi.org/10.1007/BF00286939

Skemer, P., Katayama, I., Jiang, Z., & Karato, S. (2005). The misorientation index: Development of a new method for calculating the strength of lattice-preferred orientation. *Tectonophysics*, 411(1–4), 157–167. https://doi.org/10.1016/j.tecto.2005.08.023

Soustelle, V., Tommasi, A., Bodinier, J. L., Garrido, C. J., & Vauchez, A. (2009). Deformation and reactive melt transport in the mantle lithosphere above a large-scale partial melting domain: The Ronda peridotite Massif, Southern Spain. *Journal of Petrology*, 50(7), 1235–1266. https://doi.org/10.1093/petrology/egp032

Stuart, C. A., Piazolo, S., & Daczko, N. R. (2018). The recognition of former melt flux through high-strain zones, (May 2017). https://doi.org/10.1111/jmg.12427

Suades, E., & Crespo-blanc, A. (2011). Onshore study of syn-orogenic olistostromic deposits in the Gibraltar Arc : a tool to reveal mountain front uplift. *EGU*.

Suhr, G. (1993). Evaluation of upper mantle microstructures in the Table Mountain massif (Bay of Islands ophiolite). *Journal of Structural Geology*, 15(11), 1273–1292. https://doi.org/10.1016/0191-8141(93)90102-G

Tholen, S., Linckens, J., Heckel, C., & Kemperle, M. (2022). Reaction-induced phase mixing and the formation of ultramylonitic bands. *Tectonophysics*, 827(December 2021). https://doi.org/10.1016/j.tecto.2022.229230

Tommasi, A., & Vauchez, A. (2015). Heterogeneity and anisotropy in the lithospheric mantle. *Tectonophysics*, 661, 11–37. https://doi.org/10.1016/j.tecto.2015.07.026

Tommasi, A., Langone, A., Padrón-Navarta, J. A., Zanetti, A., & Vauchez, A. (2017). Hydrous melts weaken the mantle, crystallization of pargasite and phlogopite does not: Insights from a petrostructural study of the Finero peridotites, southern Alps. *Earth and Planetary Science Letters*, 477, 59–72. https://doi.org/10.1016/j.epsl.2017.08.015

Vauchez, A., & Garrido, C. J. (2001). Seismic properties of an asthenospherized lithospheric mantle: Constraints from lattice preferred orientations in peridotite from the Ronda massif. *Earth and Planetary Science Letters*, 192(2), 235–249. https://doi.org/10.1016/S0012-821X(01)00448-4

Van der Wal, D. (1993). *Deformation process in mantle peridotites with emphasis on the Ronda peridotite of SW Spain*. *Geologica Ultraiectina* (Vol. 102).

Van Der Wal, D., & Bodinier, J.-L. (1996). Origin of the recrystallisation front in the Ronda peridotite by km-scale pervasive porous melt flow. *Contributions to Mineralogy and Petrology*, 122(4), 387–405. https://doi.org/10.1007/s004100050135

Van Der Wal, D., & Jean-Louis, B. (1996). Origin of the recrystallisation front in the Ronda peridotite by km-scale pervasive porous melt flow. *Contributions to Mineralogy and Petrology*, 122(4), 387–405. https://doi.org/10.1007/s004100050135

Van Der Wal, D., & Vissers, R. L. M. (1993). Uplift and emplacement of upper mantle rocks in the western Mediterranean. *Geology*. https://doi.org/10.1130/0091-7613(1993)021<1119:UAEOUM>2.3.CO;2

Van Der Wal, D., & Vissers, R. L. M. (1996). Structural petrology of the Ronda peridotite, SW Spain: Deformation history. *Journal of Petrology*, 37(1), 23–43. https://doi.org/10.1093/petrology/37.1.23

Wang, C., Liang, Y., & Xu, W. (2021). Formation of Amphibole-Bearing Peridotite and Amphibole-Bearing Pyroxenite Through Hydrous Melt-Peridotite Reaction and In Situ Crystallization: An Experimental Study. *Journal of*

Geophysical Research: Solid Earth, 126(3). https://doi.org/10.1029/2020JB019382

White, S. H., Burrows, S. E., Carreras, J., Shaw, N. D., & Humphreys, F. J. (1980). On mylonites in ductile shear zones. *Journal of Structural Geology, 2*(1–2), 175–187. https://doi.org/10.1016/0191-8141(80)90048-6

1395

Bergmann, R., Chan, R. H., Hielscher, R., Persch, J., & Steidl, G. (2016). Restoration of manifold-valued images by half-quadratic minimization. *Inverse Problems and Imaging, 10*(2), 281–304. https://doi.org/10.3934/ipi.2016001

Beyer, E. E., Griffin, W. L., & O'Reilly, S. Y. (2006). Transformation of archaean lithospheric mantle by refertilization: Evidence from exposed peridotites in the Western Gneiss Region, Norway. *Journal of Petrology, 47*(8), 1611–1636.

1400 https://doi.org/10.1093/petrology/egl022

Cherniak, D. J., & Liang, Y. (2012). Ti diffusion in natural pyroxene. *Geochimica et Cosmochimica Acta, 98*, 31–47. https://doi.org/10.1016/j.gca.2012.09.021

Coltorti, M., Bonadiman, C., Faccini, B., Grégoire, M., O'Reilly, S. Y., & Powell, W. (2007). Amphiboles from suprasubduction and intraplate lithospheric mantle. *Lithos, 99*(1–2), 68–84. https://doi.org/10.1016/j.lithos.2007.05.009

1405 Dijkstra, A. H., Drury, M. R., Vissers, R. L. M., & Newman, J. (2002). On the role of melt-rock reaction in mantle shear zone formation in the Othris Peridotite Massif (Greece). *Journal of Structural Geology, 24*(9), 1431–1450. https://doi.org/10.1016/S0191-8141(01)00142-0

Frets, E., Tommasi, A., Garrido, C. J., Padrón-Navarta, J. A., Amri, I., & Targuisti, K. (2012). Deformation processes and rheology of pyroxenites under lithospheric mantle conditions. *Journal of Structural Geology, 39*(June), 138–157.

1410 https://doi.org/10.1016/j.jsg.2012.02.019

Frets, E., Tommasi, A., Garrido, C., Vauchez, A., Mainprice, D., Kamaltarguisti, & Amri, I. (2014). The beni-bousera peridotite (rif belt, morocco): An oblique-slip low-angle shear zonethinning the subcontinental mantle lithosphere. *Journal of Petrology, 55*(2), 283–313. https://doi.org/10.1093/petrology/egt067

Furusho, M., & Kanagawa, K. (1999). Transformation-induced strain localization in a lherzolite mylonite from the Hidaka

1415 metamorphic belt of central Hokkaido, Japan. *Tectonophysics, 313*(4), 411–432. https://doi.org/10.1016/S0040-1951(99)00215-2

Garrido, C. J., Gueydan, F., Booth-Rea, G., Précigout, J., Hidas, K., Padrón-Navarta, J. A., & Marchesi, C. (2011). Garnet lherzolite and garnet-spinel mylonite in the Ronda peridotite: Vestiges of Oligocene backarc mantle lithospheric extension in the western Mediterranean. *Geology, 39*(10), 927–930. https://doi.org/10.1130/G31760.1

1420 Hidas, K., Garrido, C. J., Tommasi, A., Padrón-Navarta, J. A., Thielmann, M., Konc, Z., et al. (2013). Strain localization in pyroxenite by reaction-enhanced softening in the shallow subcontinental lithospheric mantle. *Journal of Petrology, 54*(10), 1997–2031. https://doi.org/10.1093/petrology/egt039

Hidas, K., Tommasi, A., Garrido, C. J., Padrón-Navarta, J. A., Mainprice, D., Vauchez, A., et al. (2016). Fluid-assisted strain localization in the shallow subcontinental lithospheric mantle. *Lithos, 262*, 636–650.

1425 https://doi.org/10.1016/j.lithos.2016.07.038

Hirth, G., & Kohlstedt, D. L. (1995). Experimental constraints on the dynamics of the partially molten upper mantle 2. Deformation in the dislocation creep regime. *J. Geophys. Res.*, *100*(B8), 15441–15449.

Hu, W. J., Zhong, H., Chu, Z. Y., Zhu, W. G., Bai, Z. J., & Zhang, C. (2020). Ancient Refertilization Process Preserved in the Plagioclase Peridotites: An Example From the Shuanggou Ophiolite, Southwest China. *Journal of Geophysical Research: Solid Earth*, *125*(1), 1–21. https://doi.org/10.1029/2019JB017552

Jung, H. (2017). Crystal preferred orientations of olivine, orthopyroxene, serpentine, chlorite, and amphibole, and implications for seismic anisotropy in subduction zones: a review. *Geosciences Journal*, *21*(6), 985–1011. https://doi.org/10.1007/s12303-017-0045-1

Lenoir, X., Garrido, C. J., Bodinier, J. L., Dautria, J. M., & Gervilla, F. (2001). The recrystallization front of the Ronda peridotite: Evidence for melting and thermal erosion of subcontinental lithospheric mantle beneath the Alboran basin. *Journal of Petrology*, *42*(1), 141–158. https://doi.org/10.1093/petrology/42.1.141

Linckens, J., Herwegh, M., Mntener, O., & Mercolli, I. (2011). Evolution of a polymineralic mantle shear zone and the role of second phases in the localization of deformation. *Journal of Geophysical Research: Solid Earth*, *116*(6), 1–21. https://doi.org/10.1029/2010JB008119

Mameri, L., Tommasi, A., Signorelli, J., & Hansen, L. N. (2019). Predicting viscoplastic anisotropy in the upper mantle: a comparison between experiments and polycrystal plasticity models. *Physics of the Earth and Planetary Interiors*, *286*(October 2018), 69–80. https://doi.org/10.1016/j.pepi.2018.11.002

Müntener, O., & Piccardo, G. B. (2003). Melt migration in ophiolitic peridotites: The message from Alpine Apennine peridotites and implications for embryonic ocean basins. *Geological Society Special Publication*, *218*(Anonymous 1972), 69–89. https://doi.org/10.1144/GSL.SP.2003.218.01.05

Newman, J., Lamb, W. M., Drury, M. R., & Vissers, R. L. M. (1999). Deformation processes in a peridotite shear zone: Reaction softening by an H2O deficient, continuous net transfer reaction. *Tectonophysics*, *303*(1–4), 193–222. https://doi.org/10.1016/S0040-1951(98)00259-5

Pantleon, W. (2008). Resolving the geometrically necessary dislocation content by conventional electron backscattering diffraction. *Scripta Materialia*, *58*(11), 994–997. https://doi.org/10.1016/j.scriptamat.2008.01.050

Précigout, J., & Hirth, G. (2014). B type olivine fabric induced by grain boundary sliding. *Earth and Planetary Science Letters*, *395*, 231–240. https://doi.org/10.1016/j.epsl.2014.03.052

Précigout, J., Gueydan, F., Garrido, C. J., Cogné, N., & Booth Rea, G. (2013). Deformation and exhumation of the Ronda peridotite (Spain). *Tectonics*, *32*(4), 1011–1025. https://doi.org/10.1002/tect.20062

Putnis, A., Niedermeier, D. R. D., & Putnis, C. V. (2006). From epitaxy to topotaxy: The migration of reaction interfaces through crystals. *Geochimica et Cosmochimica Acta*, *70*(18), A509. https://doi.org/10.1016/j.gca.2006.06.1479

de Ronde, A. A., & Stünitz, H. (2007). Deformation enhanced reaction in experimentally deformed plagioclase olivine aggregates. *Contributions to Mineralogy and Petrology*, *153*(6), 699–717. https://doi.org/10.1007/s00410-006-0171-7

Le Roux, V., Bodinier, J. L., Tommasi, A., Alard, O., Dautria, J. M., Vauchez, A., & Riches, A. J. V. (2007). The Lherz spinel lherzolite: Refertilized rather than pristine mantle. *Earth and Planetary Science Letters*, *259*(3–4), 599–612. https://doi.org/10.1016/j.epsl.2007.05.026

Soustelle, V., Tommasi, A., Bodinier, J. L., Garrido, C. J., & Vauchez, A. (2009). Deformation and reactive melt transport in the mantle lithosphere above a large-scale partial melting domain: The Ronda peridotite Massif, Southern Spain. *Journal of Petrology*, *50*(7), 1235–1266. https://doi.org/10.1093/petrology/egp032

Suades, E., & Crespo-blanc, A. (2011). Onshore study of syn-orogenic olistostromic deposits in the Gibraltar Arc : a tool to reveal mountain front uplift. *EGU*.

Tholen, S., Linckens, J., Heckel, C., & Kemperle, M. (2022). Reaction-induced phase mixing and the formation of ultramylonitic bands. *Tectonophysics*, *827*(December 2021). https://doi.org/10.1016/j.tecto.2022.229230

Vieira Duarte, J. F., Kaczmarek, M. A., Vonlanthen, P., Putlitz, B., & Müntener, O. (2020). Hydration of a Mantle Shear Zone Beyond Serpentine Stability: A Possible Link to Microseismicity Along Ultraslow Spreading Ridges? *Journal of Geophysical Research: Solid Earth*, *125*(10), 1–24. https://doi.org/https://doi.org/10.1029/2020JB019509

Van der Wal, D. (1993). *Deformation process in mantle peridotites with emphasis on the Ronda peridotite of SW Spain. Geologica Ultraiectina* (Vol. 102).

Van Der Wal, D., & Vissers, R. L. M. (1996). Structural petrology of the Ronda peridotite, SW Spain: Deformation history. *Journal of Petrology*, *37*(1), 23–43. https://doi.org/10.1093/petrology/37.1.23

White, S. H., Burrows, S. E., Carreras, J., Shaw, N. D., & Humphreys, F. J. (1980). On mylonites in ductile shear zones. *Journal of Structural Geology*, *2*(1–2), 175–187. https://doi.org/10.1016/0191-8141(80)90048-6